

KRZYSZTOF CHUDYBA, PIOTR MATYSEK\*

## METHODS FOR DETERMINING MASONRY WALLS FIRE RESISTANCE

### METODY OKREŚLANIA ODPORNOŚCI OGNIOWEJ ŚCIAN MUROWYCH

#### Abstract

In the paper, the general procedures for masonry wall design in fire situations are presented together with methods for determining the fire resistance according to EN 1996-1-2 [1] and its Polish version, PN-EN 1996-1-2 [2]. Special attention is paid to the practical application of presented methods (tabulated data and simplified methods based on reduced cross-section) and to pointing out possible problems and shortcomings. There is also brief comments on the process of introducing Euro code 6 (EN 1996-1-1 [3], EN 1996-1-2 [1]) for the design of masonry structures in Polish practice (codes: PN-EN 1996-1-1 [4], PN-EN 1996-1-2 [2]).

*Keywords: masonry structures, fire resistance, verification methods*

#### Streszczenie

W artykule przedstawiono metody weryfikacji odporności ogniowej ścian murowych według normy EN 1996-1-2 [1] i jej polskiej wersji PN-EN 1996-1-2 [2]. Szczególną uwagę zwrócono na praktyczne aspekty stosowania opisanych metod (danych tabelarycznych, uproszczonych metod bazujących na przekroju zredukowanym), wskazując ich potencjalne niedostatki. Skomentowano także proces wprowadzania normy Eurokod 6 (EN 1996-1-1 [3], EN 1996-1-2 [1]) do projektowania konstrukcji murowych do polskiej praktyki projektowej (normy: PN-EN 1996-1-1 [4], PN-EN 1996-1-2 [2]).

*Słowa kluczowe: konstrukcje murowe, odporność ogniowa, metody weryfikacji*

\* PhD. Eng. Krzysztof Chudyba, PhD. Eng. Piotr Matysek, Institute for Building Material and Structures, Faculty of Civil Engineering, Cracow University of Technology.

## 1. Introduction

The basic requirements formulated for masonry structures in the case of fire include: load-bearing capacity ( $R$  function), integrity ( $E$  function) and thermal insulation ( $I$  function). In practice, these functions connected with fire resistance of specified structural elements are being transformed onto fire resistance classes expressed in minutes (30, 60, 90, ... , 240) for standard fire exposure. In the case of fire, the analysis of structure may be conducted on the level of isolated elements, for the part of the structure or for the whole structural system (global analysis). Fire models/scenarios used for the analysis may also exhibit different levels of complexity and accuracy – from nominal (standard) ones to real parametric fires. Within particular combinations of fire model and structural analysis level, different methods for verification of fire resistance may be applied: descriptive methods (using tabulated data), simplified or advanced engineering (calculation) methods, fire tests or a combination of tests and calculations.

For masonry structures, just as with structures constructed from other materials, for the specified time of fire duration it is necessary to satisfy the following general condition:

$$E_{fi} \leq R_{fi,t,d} \quad (1)$$

where:

- $E_{fi}$  – design value of actions effect for fire conditions according to EN 1991-1-2 [5], accounting for thermal strains effects,
- $R_{fi,t,d}$  – appropriate design resistance for fire situations determined whilst taking into account the unfavourable effects of high temperature on the mechanical properties of masonry walls.

General principles as to the determination of fire resistance based on fire tests or tests combined with calculations are included in EN 1990 [6].

Due to practical reasons, tests in the fire chamber are usually carried out for isolated masonry walls, thus it is not possible to model the existence of other adjacent or restraining elements. Therefore, results can rather seldom be directly generalized onto elements with different geometry, load patterns or boundary conditions. However, the major advantages of fire tests over tabulated data or simplified calculation methods is the fact that they provide information about the real temperature distribution in walls and its deformations during heating as well as providing information about weak or sensitive points (e.g. connections) that are very difficult to detect by any other method. Results obtained from fire tests depend on the detailed procedures assumed, tests conditions, and the accuracy of applied measuring devices – hence the need for harmonisation of fire tests to have the possibility to compare results from different research centres in an univocal manner. In the case of masonry load-bearing walls, such procedures for fire testing are formulated and given in EN 1365-1 [7] and for non load-bearing walls – in EN 1364-1 [8].

## 2. Procedures for determining fire load capacity of masonry walls according to Eurocode 6 [1]

Behaviour of masonry walls in high temperature is conditioned by various factors:

- masonry unit material – ceramic, silicates, normal weight or lightweight concrete, cellular concrete, natural or artificial stone.
- type of masonry unit – solid, hollowed (type and magnitude of openings, their percentage participation in masonry unit volume), thickness of internal and external walls.
- type of mortar (normal, thin layer, lightweight),
- ratio of design load to design resistance of wall.
- wall thickness.
- load eccentricity.
- masonry unit density.
- type of wall structure (single-leaf, cavity wall, load bearing or non-load bearing wall)
- type and method of finishing the walls' surface.

Due to this fact, while applying any calculation method for masonry walls fire resistance, it is necessary to operate with temperature dependent properties that should be determined separately not only for each masonry material, but also for each type of masonry unit made from the same material, whilst taking into account the other major factors mentioned above.

### 2.1. Tabulated data for determining the fire resistance of masonry walls

Evaluation of fire resistance for masonry walls may be carried out in the simplest manner by using the tabulated data included in Appendix B of EN 1996-1-2 [1]. The tables provided give minimum thickness of walls necessary to achieve the required fire resistance for specified types of wall and for determined way of loading. Tables may be applied for walls that satisfy requirements of EN 1996-1-1[3], EN 1996-1-2 [1] and EN 1996-3 [9] for appropriate types and functions of walls. Values of minimum thicknesses are defined for the structural layer of walls, without taking into account the finishing layers.

In Table 1 there are presented requirements as to the minimum wall thicknesses for satisfying appropriate *REI* function for load-bearing walls (with normal mortar, constructed from elements from group 1) according to EN 1996-1-2 [1]. In cases where two lines of numerical values are given in the table, the first set determines fire resistance for the wall without a finishing layer, while the second – for walls with appropriate finishing layers but with a thickness of at least 10 mm from both sides for single-leaf wall or from the side of the fire action for the cavity wall. If there are two values given in one line (for ex. 70/90) it means that the recommended wall thickness is within the defined range (for ex. from 70 to 90 mm).

According to PN-EN 1996-1-1 [4] the minimum thickness for structural walls constructed from masonry units with  $f_k \geq 5$  MPa should not be smaller than 100 mm, and for walls with  $f_k < 5$  MPa – 150 mm ( $f_k$  – characteristic value of compressive strength for wall). The minimum thickness for shear walls is 180 mm. In practice, in Poland there are applied as structural elements walls with thickness at least equal to 180 mm, which means that they satisfy the criterion *REI* 90 and for some materials (even for minimum thicknesses equal to 180 mm) also *REI* 120.

**Minimum thickness for load-bearing brick wall (REI criteria) to satisfy fire resistance requirements according to EN 1996-1-2 [1] – walls with normal mortar made from elements of group 1**

Type of masonry elements in wall		Minimum wall thickness [mm] to obtain fire classification REI for time [minutes] $t_{f,d}$					
		REI 30	REI 60	REI 90	REI 120	REI 180	REI 240
ceramic <sup>(1)</sup>	$A \leq 1,0$	90/100 (70/90)	90/100 (70/90)	100/170 (70/90)	100/140 (100/140)	170/190 (110/170)	190/210 (170/190)
	$A \leq 0,6$	90/100 (70/90)	90/100 (70/90)	100/140 (70/90)	140/170 (100/140)	140/170 (110/170)	190/200 (170/190)
silicate <sup>(2)</sup>	$A \leq 1,0$	90/100 (90/100)	90/100 (90/100)	100 (90/100)	140/200 (140)	190/240 (170/190)	190/240 (140)
	$A \leq 0,6$	90/100 (90/100)	90/100 (90/100)	100 (100)	120/140 (100)	170/200 (140)	190/200 (140)
normal weight concrete <sup>(3)</sup>	$A \leq 1,0$	90/170 (90/140)	90/170 (90/140)	90/170 (90/140)	100/190 (90/170)	140/240 (100/190)	150/300 (100/240)
	$A \leq 0,6$	70/140 (60/100)	70/140 (70/100)	90/170 (70/100)	90/170 (70/140)	100/190 (90/170)	140/240 (100/190)
lightweight concrete <sup>(4)</sup>	$A \leq 1,0$	90/170 (90/140)	90/170 (90/140)	100/170 (90/140)	100/190 (90/170)	140/240 (100/190)	150/300 (100/240)
	$A \leq 0,6$	70/140 (60/100)	70/140 (60/100)	90/170 (70/100)	90/170 (70/140)	100/190 (90/170)	100/240 (90/190)
cellular concrete $350 \leq \rho \leq 500$	$A \leq 1,0$	90/115 (90/115)	90/140 (90/115)	90/200 (90/200)	90/225 (90/225)	140/300 (140/240)	150/300 (150/300)
	$A \leq 0,6$	90/115 (90/115)	90/115 (90/115)	100/150 (90/115)	90/175 (90/150)	140/200 (140/200)	150/200 (150/200)
cellular concrete $500 \leq \rho \leq 1000$	$A \leq 1,0$	90/100 (90/100)	90/150 (90/100)	90/170 (90/150)	90/200 (90/170)	125/240 (100/200)	150/300 (100/240)
	$A \leq 0,6$	90/100 (90/100)	90/100 (90/100)	90/150 (90/100)	90/170 (90/125)	125/240 (125/140)	150/240 (150/200)

(<sup>1</sup>)  $5 \text{ MPa} \leq f_b \leq 75 \text{ MPa}$ ;  $1000 \leq \rho \leq 2400 \text{ kg/m}^3$ ; (<sup>2</sup>)  $12 \text{ MPa} \leq f_b \leq 15 \text{ MPa}$ ;  $1400 \leq \rho \leq 2400 \text{ kg/m}^3$   
(<sup>3</sup>)  $6 \text{ MPa} \leq f_b \leq 35 \text{ MPa}$ ;  $1200 \leq \rho \leq 2400 \text{ kg/m}^3$ ; (<sup>4</sup>)  $2 \text{ MPa} \leq f_b \leq 15 \text{ MPa}$ ;  $400 \leq \rho \leq 1600 \text{ kg/m}^3$   
 $f_b$  – normalized compressive strength for masonry elements [MPa]  
 $\rho$  – volume density [kg/m<sup>3</sup>]

## 2.2. Calculation methods for masonry walls fire resistance verification

Fire resistance of masonry walls may be also determined by calculation methods assuming appropriate failure mechanisms in case of fire action, appropriate temperature dependent material properties, wall thickness as well as effects of thermal strains and deformations. In EN 1996-1-2 [1] there are included two calculation methods for fire resistance determination: simplified (in Annex C) and advanced (in Annex D).

In introduction to calculation methods it is underlined that their accuracy is to be determined by comparison of calculated values with fire tests results.

According to the **simplified method** for fire design, the resistance is calculated using boundary conditions for reduced cross-section of the wall, for established time of fire duration and for loads as for normal temperature design. This method may be only applied for standard fire conditions. In the calculation procedure, it is necessary to determine temperature profiles within the cross-section, then to evaluate the reduced cross-section and calculate the capacity for ultimate limit state for reduced cross-section and finally – to verify if this capacity (calculated according to general assumption as for normal temperature conditions given in EN 1996-1-1 [3]) is not less than is required for appropriate combination of actions. In Fig. 1 (showing the horizontal cross-section for the wall) there is presented the general scheme for determination of appropriate zones for reduced cross-section of the wall in the case of fire acting from one side.

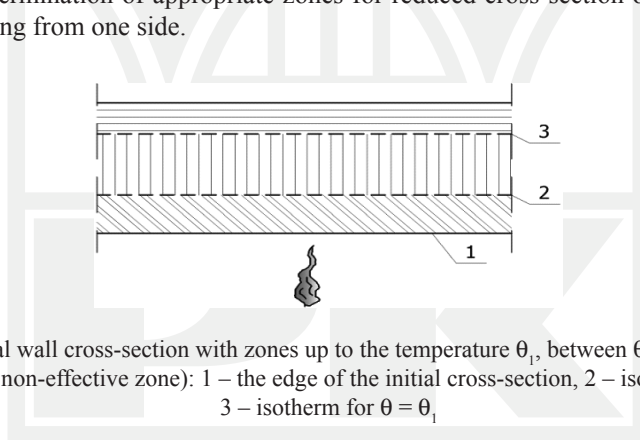


Fig. 1. Horizontal wall cross-section with zones up to the temperature  $\theta_1$ , between  $\theta_1$  and  $\theta_2$  and above  $\theta_2$  (structurally non-effective zone): 1 – the edge of the initial cross-section, 2 – isotherm for  $\theta = \theta_2$ , 3 – isotherm for  $\theta = \theta_1$

For fire situation at the ultimate limit state it is necessary to satisfy the following condition:

$$N_{Ed} \leq N_{Rd,fi(\theta)_i} \quad (2)$$

Design value of walls capacity under vertical load is expressed as:

$$N_{Rd,fi(\theta)_i} = \Phi(f_{d\theta_1}A_{\theta_1} + f_{d\theta_2}A_{\theta_2}) \quad (3)$$

where:

- $A_{\theta_1}$  – area of masonry wall zone with temperature not exceeding  $\theta_1$ ;
- $A_{\theta_2}$  – area of masonry wall with temperature between  $\theta_1$  and  $\theta_2$ ;

- $\theta_1$  – maximum temperature at which the strength of masonry walls may be assumed as for normal temperature conditions (see: Table 2);
- $\theta_2$  – temperature above which masonry wall strength is reduced (see: Table 2);
- $N_{Ed}$  – design value of vertical load;
- $f_{d\theta 1}$  – design value of compressive strength for masonry walls in temperatures not exceeding  $\theta_1$ ;
- $f_{d\theta 2}$  – design value of compressive strength in the temperature range between  $\theta_1$  and  $\theta_2$ , assumed as  $cf_{d,fi}$ ;
- $c$  – constant determined from stress-strain relationship obtained from fire test for appropriate considered material (see: Table 2);
- $X$  – reduction coefficient for capacity in the middle of wall determined on the basis of EN 1996-1-1 [3] (where it is denoted as  $\theta_m$ ) whilst taking into account additional eccentricity  $e_{\Delta\theta}$ ;
- $e_{\Delta\theta}$  – eccentricity caused by fire load.

Eccentricity  $e_{\Delta\theta}$  caused by fire action may be determined from fire tests or from the relationship:

$$e_{\Delta\theta} = \frac{1}{8} h_{ef}^2 \frac{\alpha_t(\theta_2 - 20)}{t_{Fr}} \leq h_{ef} / 20 \quad (4)$$

where:

- $e_{\Delta\theta} = 0$  when fire is acting from all sides,
- $h_{ef}$  – effective height of wall,
- $\alpha_t$  – thermal elongation coefficient for masonry walls according to EN 1996-1-1 [3], p. 3.7.4,
- 20°C – temperature assumed on the non-heated surface of the wall,
- $t_{Fr}$  – thickness of cross-section for which temperature does not exceed  $\theta_2$ .

In Table 2, there are listed values of parameters needed for masonry wall calculation under vertical loading according to equation (3). It is worth underlying that despite introducing and defining the constant  $c$ , there are not included the specified numerical values for that symbol. It is recommended to determine  $c$  values from fire tests separately for each different masonry wall material.

In Fig. 2 there is schematically presented the temperature distribution along the wall's thickness together with way of determination of reduced cross-section for calculation of fire resistance on the base of the simplified method.

Temperature distributions in wall cross-sections and the temperature at which a masonry wall is no longer structurally effective material in fire condition should generally be determined on the base of fire tests or using information from the fire test results base. As a design aid, temperature distributions included in Annex C of EN 1996-1-2 [1] may be used. In Fig. 3, there are presented exemplary temperature distributions within the cross-section for standard fire durations from 30 to 120/180 minutes for walls constructed from ceramic masonry units (Fig. 3a) and from silicate masonry units (Fig. 3b).

The basis for **advanced methods** of calculation constitute the general physical laws allowing for evaluation of behaviour of structural elements subjected to fire actions. Advanced methods of calculations make it possible to determine:

- thermal response – development and distribution of temperature within structural elements, based on the principles and assumptions of heat flow theory whilst taking into account appropriate thermal actions as well as thermal and physical properties of materials as temperature functions.
- mechanical response – evaluation of structural behaviour accounting for unfavourable effects of high temperature on mechanical properties of materials and for effects of thermal stress and strains.

Table 2

**Basic parameters for masonry wall materials necessary for analysis of fire resistance according to simplified method of EN 1996-1-2 [1]**

Masonry wall elements and mortar (unprotected surface)	Value $c$	Temperature °C	
		$\theta_2$	$\theta_1$
Ceramic elements with general purpose mortar	$c_{cl}$	600	100
Silicate elements with mortar for thin joints	$c_{cs}$	500	100
Lightweight concrete elements with general purpose mortar	$c_{la}$	400	100
Normal weight concrete elements with general purpose mortar	$c_{da}$	500	100
Cellular concrete elements with mortar for thin joint	$c_{aac}$	700	200

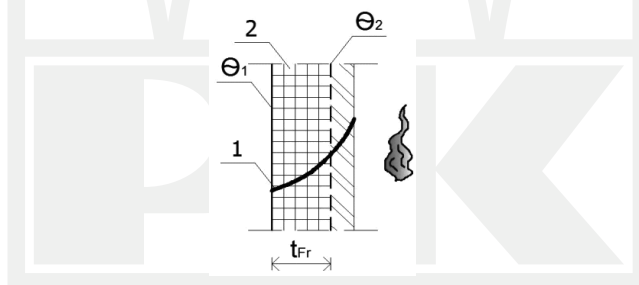


Fig. 2. Temperature distribution and definition of reduced vertical cross-section for calculating the fire resistance for wall by simplified method: 1 – temperature distribution, 2 – reduced cross-section maintaining the material strength ( $A_{01} + A_{02}$ )

Some information as to the values of parameters needed for thermal and mechanical analysis in fire situations are included in Annex C of EN 1996-1-2 [1]. In Fig. 4 and Fig. 5, there are shown selected relationships for ceramic and silicate masonry units in the form of design values of temperature dependant material physical and thermal properties (Fig. 4) and stress-strain graphs as a function of temperature (Fig. 5).

For relationships given in Fig. 5 it is worth noting that silicate masonry units (Fig. 5b) indicate within the certain range of temperatures the increase in strength in comparison with normal temperature condition (equal to 20°C), which is not observed for other materials, e.g. ceramic masonry units (Fig. 5a).

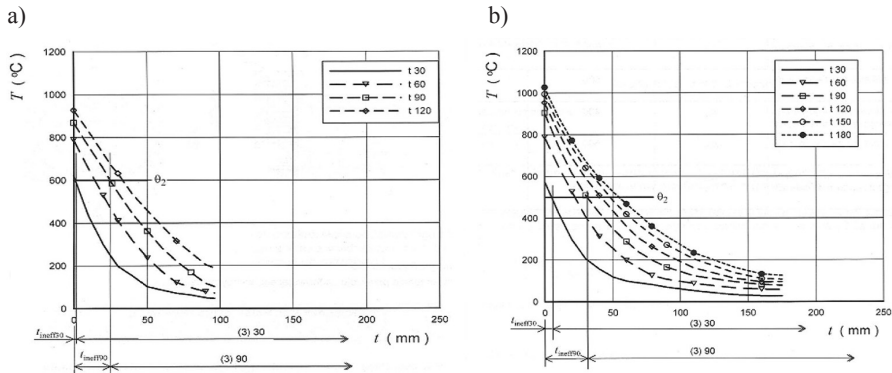


Fig. 3. Temperature distribution within the cross-section for standard fire duration from 30 to 120/180 minutes: a) ceramic masonry units (density 1000–2000 kg/m<sup>3</sup>), b) silicate masonry units (density 1500–2000 kg/m<sup>3</sup>)

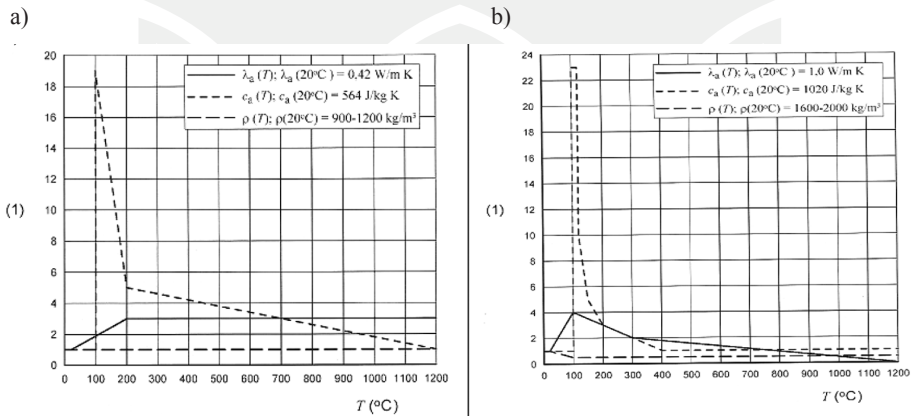


Fig. 4. Design values of temperature-dependent material properties for: ceramic masonry units (density 900–1200 kg/m<sup>3</sup>), b) silicate masonry units (density 1600–2000 kg/m<sup>3</sup>)

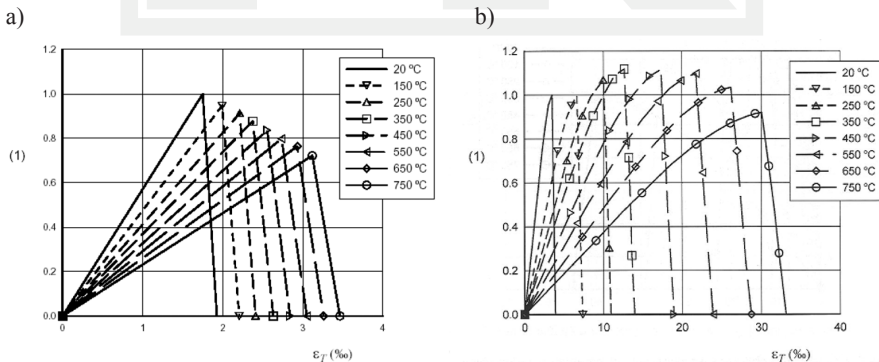


Fig. 5. Design values of temperature-dependent stress-strain relationships: a) for ceramic masonry units (group 1) with the strength 12 N/mm<sup>2</sup>–20 N/mm<sup>2</sup> and density 900 kg/m<sup>3</sup>–1 200 kg/m<sup>3</sup>, b) for silicate masonry units (group 1) with the strength 12 N/mm<sup>2</sup>–20 N/mm<sup>2</sup> and density 1600 kg/m<sup>3</sup>–2000 kg/m<sup>3</sup>

Note: vertical axis expresses the ratio of strength in fire temperature  $T$  to strength in temperature 20°C

### 2.3. Fire tests for masonry walls

For all types of masonry walls, the fire resistance may be estimated by fire tests that should be conducted according to appropriate codes [7–8]. In analyzing tests results, it may be necessary to take into account the amendments resulting from possible different systems of loading the walls in comparison with those given in codes.

Fire tests for masonry walls are necessary to determine directly the fire resistance for masonry elements and walls. But they also constitute the source for the evaluation and calibration of appropriate material parameters of different types (physical, thermal, mechanical) applied for calculation methods or advanced models. It concerns for example the value of  $c$  in simplified method of calculation, which is essential for determining appropriate zones with different values of the compressive strength of masonry units.

From information of the fire test course and results, included in reports collected by authors from different laboratories (Fires, Batizovce – Slovak Republic; MPA TU Braunschweig – Germany; ITB, Warsaw – Poland) from tests on various masonry units (ceramic, silicate, concrete) that were carried out on masonry units producers' orders, it may be concluded that due to significant differentiation in properties of materials of masonry units, the behaviour of walls constructed from various units in fire tests may be significantly diversified – with various phenomena occurring during heating or different failure modes. For example, ceramic masonry units (especially hollow ones) exhibit severe loss of external surfaces (spalling) from the side exposed to fire that may reach even 50–70% of the total area of wall (Fig. 6a) and the failure mode is usually due to formation and propagation of vertical cracks. For silicate elements there are observed, vertical and horizontal cracks in masonry elements and in joints at failure, while for cellular concrete elements during heating there is observed process of moisture condensation along joints and cracks on non-heated side of wall (Fig. 6b).

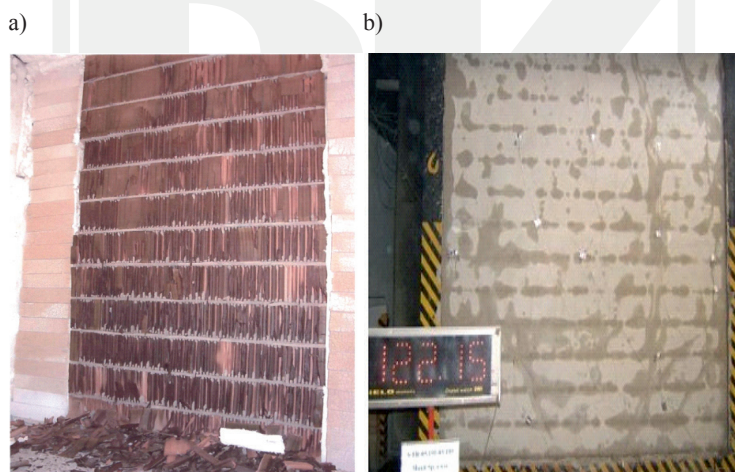


Fig. 6. Examples of typical phenomena occurring while carrying out fire tests: a) spalling from the wall side exposed to fire for ceramic masonry hollow units (Report from fire tests on walls made from THERMOPOR masonry hollowed units – LEIER, Poland), b) condensation zones along the joints and cracks for walls made of concrete blocks on non-heated surface (Report from fire tests on walls made from OPTIROC masonry units – MAXIT, Poland)

### 3. Comments on introducing EN 1996-1-2 [1] into Polish practice

Until the time of introducing the code PN-EN 1996-1-2 [2] into Poland, for determination of minimum masonry wall thickness for required fire resistance ( $REI$ ) there were applied recommendations formulated and included in the ITB Instruction [10]. Minimum wall thicknesses that were given in [10] are within the ranges proposed by PN-EN 1996-1-2 [2] or are greater than the upper limits for these ranges. In PN-EN 1996-1-2 [2], introducing EN 1996-1-2 [1] into Polish practice, there were accepted as a rule – without any changes – recommendations of European code. At the same time, there was worked out the National Annex (with Nationally determined parameters) for the code EN 1996-1-1 [3], assuming different values of coefficients for determining the masonry walls compressive strength. Compressive strengths ( $f_k$ ) evaluated from relationships included in EN 1996-1-1 [3] are significantly greater than those calculated on the basis of PN-EN 1996-1-1 [4]. Differences are also visible while determining masonry walls elasticity modulus ( $E$ ) which results in the fact that the wall's load-bearing capacity determined on the basis of relationships included in codes [3] and [4] may differ even about 30%. It plays an important role in evaluating coefficient  $\alpha$ , defining the level of exertion of wall (ratio of design load to design resistance of wall), for which the minimum wall thickness is given as a function of the required  $REI$  value. Lower values of  $f_k$  calculated on the basis of PN-EN 1996-1-1 [4] determines higher values of  $\alpha$  in comparison with those obtained from EN 1996-1-1 [3], which finally results in the necessity to accept the thicker walls by tabulated data method. Such values of  $f_k$  according to National Annex, are due to the insufficient number of experimental results within this scope considered and from the necessity to operate with the safe/conservative values. According to PN-EN 1996-1-1 [4], values of  $f_k$  may also be determined on the basis of experimental results. From these reasons, it would be desirable in Poland – in fire test preparations and programming – to determine experimentally the basic mechanical parameters for masonry walls. Such a procedure would make it possible to widen the existing test results base and to refer to the obtained results with those from foreign research centres.

### 4. Conclusions

In the paper, methods for determining masonry walls' fire resistance according to EN 1996-1-2 [1] are presented and commented on from the point of view of their practical application and with regard to fire tests. Based on that, the following general conclusions may be drawn:

1. Due to significant differentiation in thermal, physical and mechanical properties of various masonry materials, types of masonry units and mortar, while calculating the fire resistance of masonry walls, it is necessary to operate with values determined separately for each combination of these variables. Moreover, additional important factors have to be taken into account – wall thickness, load eccentricity, ratio of load design to wall's design resistance. This need may be satisfied by working out and taking advantage of the base for fire test results conducted in different research centres on numerous various masonry materials and elements (the authors are trying to collect such results from different countries and laboratories – see: p. 2.3).

2. Application of the simplest method based on tabulated data is easy and straightforward, but has some practical shortcomings and limitations. Usually in tables (see: Table 1) there are included not the specific values, but ranges of minimum wall thicknesses. In many cases – especially for units made of normal weight, lightweight and cellular concrete, but also of silicates and masonry for higher fire resistance – these ranges are quite wide and in extreme examples, the highest thickness may be even twice the lowest from the admissible wall thickness range. That may lead to quite serious problems with practical application of tabulated data by designers.
3. Calculation methods given in EN 1996-1-2 [1] are based on many parameters that should be determined by fire tests. Though some numerical values or functions are included in Annex C (for ex.: values of temperatures  $\theta_1$  and  $\theta_2$  needed for determination of zones indicating different level of design compressive strength for masonry wall, design values of temperature-dependent physical and thermal properties for various materials, design values of temperature-dependent stress-strain relationships for masonry walls materials), there is still a lack of some indispensable data (for example: value of constant  $c$  for different masonry wall elements in simplified method, being reduction coefficient for design compressive strength in the intermediate zone between the temperature  $\theta_1$  and  $\theta_2$ ). This, once again, strongly underlines the importance of fire tests and manifests the need for existence of a fire test results base.
4. As to the process of introducing Eurocode 6 (for masonry structures design in normal temperature conditions and for accidental fire situation) into Polish practice, it is worth pointing out some incoherencies existing in final versions of PN-EN 1996-1-1 [4] and PN-EN 1996-1-2 [2] due to the presence of National Annexes. They were briefly discussed in p.3 of the paper and concern mainly the questions of the determination of basic mechanical parameters ( $f_k$  and  $E$ ) for masonry walls at normal temperatures, but which also results in operating with a different value  $\alpha$  (ratio of design load to design resistance of wall) while using tabulated data – and in consequence with various resulted values of minimum wall thickness for specified required fire resistance.

## References

- [1] EN 1996-1-2: Design of masonry structures. Part 1–2: General rules – Structural fire design.
- [2] PN-EN 1996-1-2: Design of masonry structures. Part 1–2: General rules – Structural fire design (Polish Code).
- [3] EN-1996-1-1: Design of masonry structures. Part 1–1: Common rules for reinforced and unreinforced masonry structures.
- [4] PN-EN-1996-1-1: Design of masonry structures. Part 1–1: Common rules for reinforced and unreinforced masonry structures (Polish Code).
- [5] EN 1991-1-2: Actions on structures. Part 1–2: General actions – Actions on structures exposed to fire.
- [6] EN 1990: Basis of structural design.
- [7] EN 1365-1: Fire resistance tests of load-bearing elements. Part 1: Walls.
- [8] EN 1364-1: Fire resistance tests of non load-bearing elements. Part 1: Walls.
- [9] EN-1996-1-3: Design of masonry structures – Simplified calculation methods and simple rules for masonry structures.

- [10] Kosiorek M., Woźniak G., *Projektowanie elementów żelbetowych i murowych z uwagi na odporność ogniową*, Seria: *Instrukcje, Wytyczne, Poradniki nr 409/2005*, ITB, Warszawa 2005 (in Polish).
- [11] EN-1052-1: Methods of test for masonry – Part 1: Determination of compressive strength.



KRZYSZTOF CHUDYBA, SZYMON SERĘGA\*

## STRUCTURAL FIRE DESIGN METHODS FOR REINFORCED CONCRETE MEMBERS

### METODY PROJEKTOWANIA ELEMENTÓW ŻELBETOWYCH Z UWAGI NA WARUNKI POŻAROWE

#### Abstract

The paper presents methods for determining fire resistance of reinforced concrete members according to Eurocode 2-1-2 (simplified methods based on the effective cross-section and incremental-iterative approach) [3]. Results of conducted calculations are compared with fire test results taken from the literature. The main parameters considered in the conducted analysis are: concrete class, values of normal force eccentricity and cross-section shape. General conclusions are formulated as to the accuracy of simplified methods and practical limitations of their application within the analysed scope of variable material and geometrical parameters.

*Keywords: concrete structures, fire resistance, simplified methods*

#### Streszczenie

W artykule przedstawiono metody określania odporności ogniowej elementów żelbetowych według normy EN 1992-1-2 [3] (metody uproszczone bazujące na przekroju zredukowanym oraz podejście przyrostowo-iteracyjne). Rezultaty obliczeń porównano z wynikami badań ogniowych dostępnych w literaturze. W analizie obliczeniowej rozważono następujące parametry: klasę betonu, mimośród siły podłużnej, kształt przekroju. Sformułowano wnioski odnośnie dokładności metod uproszczonych i praktycznych ograniczeń ich stosowania w zakresie analizowanych zmiennych materiałowych i geometrycznych.

*Słowa kluczowe: konstrukcje betonowe, odporność ogniowa, metody uproszczone*

\* PhD. Eng. Krzysztof Chudyba, PhD. Eng. Szymon Seręga, Institute for Building Material and Structures, Faculty of Civil Engineering, Cracow University of Technology.

## 1. Introduction

In general, reinforced concrete structural members exhibit good performance under fire conditions. This is due to the fact that thermal conductivity of concrete is relatively low at room temperature and decreases with increasing temperature. As long as concrete is not damaged as a result of excessive cracking or spalling, it constitutes effective protection for reinforcing steel against high temperature occurring during fire.

The comprehensive analysis of reinforced concrete structures under the specified fire scenario includes thermal analysis (determination of temperature distribution within each point of structural elements) and mechanical analysis (evaluation of structural response to determined temperature fields). In order to carry out these analyses, it is necessary to possess detailed information as to numerous material properties (physical, thermal, mechanical – both for structural concrete and for reinforcing steel) which are the functions of temperature, for example basing on [1], as well as to operate with appropriate computational tools for coping with advanced thermo-hydro-mechanical material models for the structure.

A properly designed reinforced concrete structure is characterized in normal design conditions by a certain reserve in bearing capacity:

$$R \geq E_d > E_{d,fi}(t=0) \quad (1)$$

where:

- $R$  – the load bearing capacity,
- $E_d$  – a design value of an effect of actions according to [2],
- $E_{d,fi}(t=0)$  – a design effect of actions in fire situations at the beginning of a fire.

This reserve causes that despite the decrease in mechanical properties of reinforcing steel and concrete, additional indirect actions due to restrained deformations as well as intensified second order effects or temperature gradients, the structure does not collapse immediately, what is schematically presented in Fig. 1. It means that the structure has the ability to bear the loads by the certain time  $t_{fi}$  of fire which is called fire resistance.

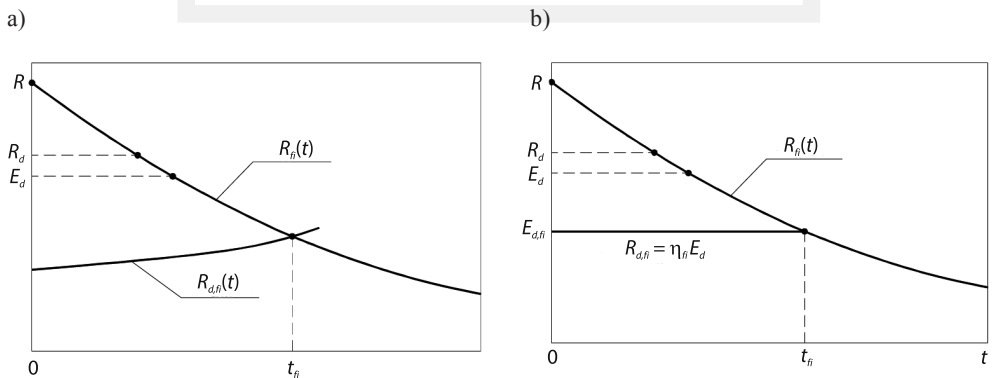


Fig. 1. Methods for determining fire resistance  $t_{fi}$ : a) indirect actions due to restrained deformations are taken into account, b) indirect actions are neglected

Usually, the indirect actions should be considered in the analysis of fire resistance  $t_{fi}$  of concrete structures. However, when high accuracy is not required or if an isolated structural member is analysed, these actions can be neglected and internal forces may be estimated from the following equation [3]:

$$E_{d,fi} = \eta_{fi} E_d \quad \eta_{fi} = \frac{G_k + \psi_{fi} Q_{k,1}}{\delta_1 \gamma_G G_k + \delta_2 \gamma_{Q,1} Q_{k,1}} \quad (2)$$

what is illustrated in Fig. 1b. In eq.  $G_k$  is a characteristic value of permanent load;  $Q_{k,1}$  is a characteristic value of major variable loads;  $\gamma_G, \gamma_{Q,1}$  are partial safety coefficients for loads  $G_k$  and  $Q_{k,1}$ ;  $\psi_{fi}$  denotes a combination coefficient with frequent or quasi-permanent values determined by  $\psi_{1,1}$  or  $\psi_{2,1}$  according to [2];  $\delta_1, \delta_2$  should be taken as 1.0 for the load combination (6.10) according to [2], for the combination (6.10a)  $\delta_1 = 1.0, \delta_2 = \psi_{0,1}$ ; while considering combination (6.10b)  $\delta_1 = \xi, \delta_2 = 1.0, \psi_{0,1}$  is a coefficient for the combination value of variable load;  $\xi$  is a reduction coefficient for unfavourable permanent load. The relationships between the coefficient  $\eta_{fi}$  and ratio of loads  $Q_{k,1}/G_k$  is presented in Fig. 2.

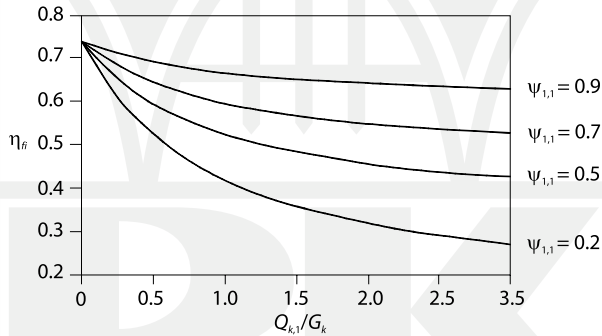


Fig. 2. Variation of reduction factor  $\eta_{fi}$  with the load ratio  $Q_{k,1}/G_k$

The low thermal conductivity of concrete makes the temperature fields in the element non-uniform which is one of the main difficulties in analysing the fire capacity of reinforced concrete structures. Due to this fact, in everyday practice, designing of simple concrete elements (slabs, beams, columns or walls) is usually made with the application of descriptive methods (for example tabulated data) or simplified engineering methods usually being the adaptations of design approaches originally derived for normal temperature conditions [4–7].

Fire is one of the most severe actions that the structure could be subjected to in the whole service life. For reasons of safety, each part of a structure has to fulfil requirements not only concerning the ultimate load states or serviceability load states but also it has to be characterized by adequate fire resistance. This results in a great interest as to the behaviour of reinforced concrete structures under high temperature conditions and contributes to the development of many analytical and numerical methods that allow the estimation of the degree of fire resistance of concrete structures. Generally, these methods may be classified into three categories [8]:

- tabulated data for well-recognized design solutions,
- simplified engineering methods (e.g. 500°C isotherm method or zone method) for specified types of structural elements,
- advanced thermo-mechanical or thermo-hydro-mechanical material models of steel and concrete for numerical modelling of parts of structures or for the whole structure.

The first category usually consists of sets of tables, where minimum distances from the centre of steel bars to the heated edge of cross-section and minimum section's dimensions for required fire resistance are provided. Estimating the fire resistance on the basis of the tabulated data is straightforward but also has significant limitations. Tabular data cover a relatively limited range of design cases – for example, tables in [3, 9] can be applied only for the ISO 834 standard fire time-temperature curve or similar and for normal strength concrete. Moreover, this type of method does not allow the determination of the actual fire load bearing capacity  $R_{fi}(t)$  for specified time  $t$  or fire resistance  $t_{fi}$  for specified  $E_{d,fi}$ .

Simplified engineering methods, i.e. the 500°C isotherm method and the zone method, will be described in detail and discussed further in the paper within the light of their accuracy and validity for determining the fire resistance for compressed reinforced concrete elements and cross-sections.

For advanced calculation methods, many physical models taking into account temperature, moisture and mechanical fields both for concrete and steel have been worked out. Generally, thermal analysis should be carried out with taking into account principles of heat and moisture flow with temperature dependent physical material characteristics. For mechanical analysis of material response for loads – both mechanical and thermal – there should be taken into account total strains including the following components: free thermal strain, immediate mechanical strain, basic (isothermal) creep strain and creep strain in transient conditions.

Advanced thermo-mechanical or thermo-hydro-mechanical models are valuable tools for better understanding of different phenomena occurring in concrete structures in fire and constitute important supplements for experimental research. However, in the case of everyday designing practices which are limited to standard structural solutions, the advanced methods are too complex to apply. Thus there is a strong need for developing simplified methods for determining  $R_{fi}(t)$  function which do not have the disadvantages of the tabular methods. In addition, simplified design methods for typical reinforced concrete elements under accidental fire conditions provide an engineer with a certain level of insight and control over conducted calculation procedures and may also constitute an initial design stage for complex non-typical structures.

## **2. Simplified methods for determining fire load capacity of RC sections according to Eurocode 2-1-2**

Simplified methods may be applied mainly for determining the load bearing capacity of a cross-section in a fire situation for elements where the plane cross-sections hypothesis remains valid. Additionally, the following assumptions are presumed:

- deformations due to fire actions do not influence the thermal field,
- free thermal strains are omitted in the analysis,
- there are omitted or taken into account indirectly transient creep strains in thermal conditions. Additional strains may be considered in stress-strain relationships of concrete

assumed for analysis, determined from experiments in transient thermal conditions (for example physical relationships given in [3]),

- stresses acting in a perpendicular direction to the elements axis resulted from temperature gradients are omitted, assuming the same material mechanical characteristics as for an uniaxial state of stress,
- explosive spalling of concrete is not taken into account,
- concrete tensile strength is omitted,
- there is assumed the full bound between reinforcing steel and surrounding concrete during the whole process of heating of an element.

The simplified methods included in Eurocode 2-1-2 [3] are supplemented with assumptions concerning both the manner of reducing the material strengths during high temperature action and the reduction of dimensions of a cross-section.

In [3] there are proposed three simplified methods for determining fire resistance of concrete elements such as beams or columns. The first two are based on the so-called “effective section”: the 500°C isotherm method and zone method. The third method is the incremental-iterative procedure where for any axial force  $N_u$  ( $N_u \leq N_{u0}$ ,  $N_{u0}$  – the load bearing capacity of axially loaded element) the ultimate bending moment  $M_u$  is determined on the basis of bending moment – curvature diagram. The main disadvantage of the latter is the fact that for every value  $N_u$  the bending moment – curvature diagram has to be constructed, which is more time consuming and laborious in comparison with the aforementioned methods.

Despite the methods included in Eurocode 2-1-2 [3], there are many simplified procedures for determining fire resistance developed especially for columns. In order to estimate fire load capacity of isolated concrete columns, the simple Rankine formula is employed [10–11] or researchers extend the procedures of their national codes for structures design at room temperature for the cases of fire actions [4–7].

## 2.1. Method of 500°C isotherm

The method of 500°C isotherm was developed in the 70-ties of the last century by Swedish researchers [12] and was introduced into Eurocode 2-1-2 [3] and the CEB-FIP Bulletin [9].

The basis of this method constitutes an observation that the reduction in compressive strength of concrete is not significant within the temperature range from 20°C to 500°C. After exceeding the temperature level of 500°C, compressive strength of concrete radically decreases, reaching at temperature 700°C the value of only about 30% of initial strength. Hence, it was assumed that the thickness  $a_z$  by which the cross-sectional dimensions are to be reduced due to fire effects, should be determined by the location of 500°C isotherm. As a result, a new shape of cross-section of the element is created within the 500°C isotherm being the restricting line (Fig. 3). Concrete properties within the new cross-section are the same as for normal temperature. Reduction of yielding stress of reinforcing steel is conducted as the function of temperature level at the centre of each bar despite their location with regard to the 500°C isotherm.

Having determined the reduced cross-section dimensions and the reduced level of yielding stress for steel, the load bearing capacity in fire situation for element  $R_{f,t}$  at time  $t$  is calculated on the basis of the commonly accepted methods for reinforced concrete elements analysis in normal temperature conditions.

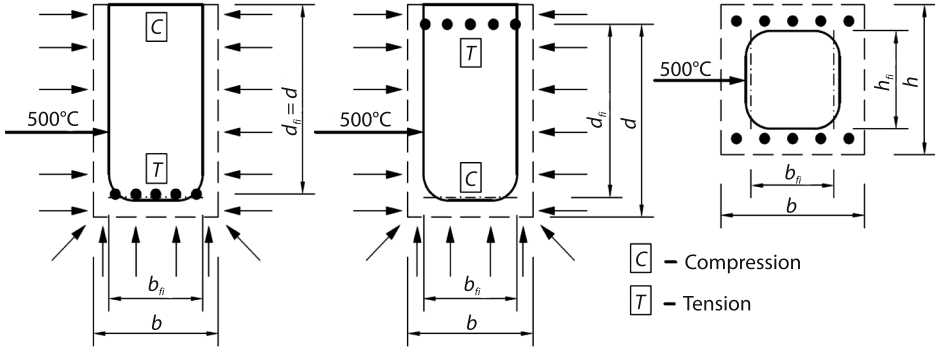


Fig. 3. Reduced cross-section of reinforced concrete beam or column in 500°C isotherm method

The method of 500°C isotherm is relatively simple and may be applied for all cross-section shapes and different heating scenarios (fire from both sides of load-bearing walls, fire from all four sides for columns, etc.) but it also has some limitations. It was worked out and experimentally verified for elements made of normal strength concrete (NSC) that were subjected to failure due to exceeding the capacity of tensile reinforcement and usually not heated from the compressive side (beams, slabs heated from the bottom side). For compressed elements, especially when an eccentricity of a normal force is small, and for elements made of high strength concrete (HSC) 500°C isotherm method may overestimate the load bearing capacity in a fire situation that was earlier indicated in [13–15].

## 2.2. Zone method

The zone method, that constitutes an alternative to the 500°C isotherm method, was worked out in the eighties of the last century by K. Hertz [16]. Eurocode 2-1-2 [3] recommends its application for elements subjected to a bending moment and a compressive normal force.

In Fig. 4 there are presented assumptions and basic notations for which the effective cross-section dimensions are to be determined. Considering the section of wall heated from both sides, it is possible to evaluate the temperature distribution by solving transient but one-dimensional heat flow problems. Having temperature distribution  $\theta(x)$ , one may determine maximum stress that may be carried by each of the concrete fibres  $f_c(\theta(x))$ . It is assumed that the compressive strength of concrete for the middle part of the cross-section  $b_f = 2w - 2a_z$  has a constant value equal to  $f_c(\theta_M)$ , where  $\theta_M$  denotes the temperature in the coldest concrete fibre. For the analysed case, it is the fibre located in the middle of the wall. The thickness of the layer  $a_z$  is determined from the equality of the area below the graph of  $f_c(\theta(x))$  and the area of a rectangle with a width of  $b_f$  and a height equal to  $f_c(\theta_M)$ :

$$a_z = w \left[ 1 - \delta_{f_c} \right] \quad \delta_{f_c} = \frac{\int_{-w}^w f_c(\theta(x)) dx}{2w \cdot f_c(\theta_M)} \cong \frac{\sum_{i=1}^n k_c(\theta_i)}{n \cdot k_c(\theta_M)} \quad (3)$$

In equation (3),  $k_c(\theta)$  is the ratio of concrete compressive strength at temperature  $\theta$  to the value at normal temperature. By dividing the width  $w$  into  $n$  equal parts ( $n \geq 3$ ) and by calculating the temperature in the middle of each layer  $\theta_i$ , the integral in the equation for  $\delta_{fc}$  may be approximately substituted by the sum.

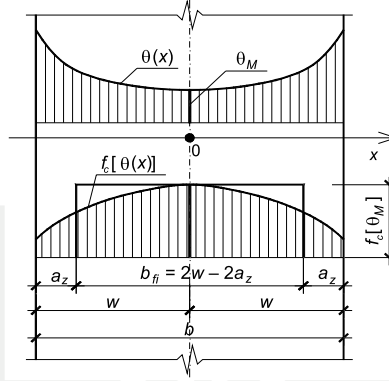


Fig. 4. Assumptions and notations for zone method

In Appendix B for Eurocode 2-1-2 [3], the equation for  $\delta_{fc}$  is given in the transformed version. For thin divisions  $n$ , the modified form of equation (4) takes into account significant variation in temperature within the zone of each division:

$$a_z = w \left[ 1 - \delta_{fc} \right] \quad \delta_{fc} = \frac{1 - \frac{1}{5n} \sum_{i=1}^n k_c(\theta_i)}{n k_c(\theta_M)} \quad (4)$$

Detailed information as to the reduction of cross-sectional dimensions by a value  $a_z$  for different shapes is included in Appendix B of Eurocode 2-1-2 [3].

The fire resistance  $R_f(t)$  for zone method is determined – similarly to the 500°C isotherm method – using classical methods of concrete structures theory. Calculations are being carried out for the reduced geometry of cross-sections, reduced yielding stress for steel  $f_{y,red} = k_s(\theta_s) f_y(20^\circ\text{C})$  ( $\theta_s$  – temperature of reinforcing steel) and for reduced concrete compressive strength evaluated from the relationship  $f_{c,red} = k_c(\theta_M) f_c(20^\circ\text{C})$ .

### 2.3. Incremental-iterative method

A scheme for determining the ultimate bending moment – compressive force envelope  $M_u - N_u$  for reinforced concrete element by the incremental – iterative approach is presented in Fig. 5.

In this method, the ultimate load bearing capacity is determined for physical relationships of concrete  $\sigma_c = \sigma_c(\epsilon, \theta)$  with the “softening” branch within the zone of post-critical strains taken into account. The physical law for reinforcing steel  $\sigma_s = \sigma_s(\epsilon, \theta)$  may be assumed with or without hardening after reaching yielding stress.

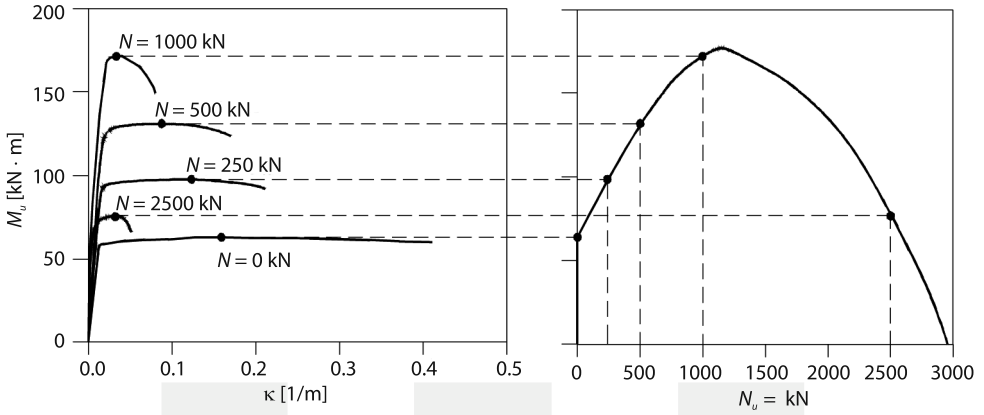


Fig. 5. Scheme for constructing  $M_u - N_u$  envelope by incremental-iterative procedure

The relationship between strains in the most compressed fibre of concrete  $\varepsilon_c$ , most tensile reinforcing bar  $\varepsilon_s$  and element curvature  $\kappa$  is expressed as (see: Fig. 6):

$$\kappa = \frac{\varepsilon_c - \varepsilon_s}{d} \quad (5)$$

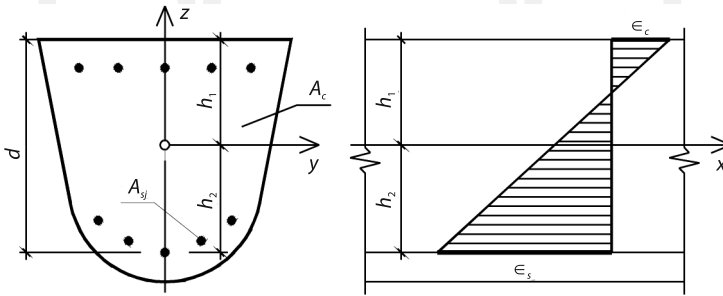


Fig. 6. Overall notations in incremental-iterative procedure

Assuming the plain cross-sections principle and appropriate physical laws of concrete and reinforcing steel, for each curvature  $\kappa$  there should be found such cross-section strain  $\varepsilon_c$  for which the resultant of normal stresses is equal to force  $N_u$ . Such an approach leads to a solution of the equation (with regard to  $\varepsilon_c$ ) in the following form:

$$\iint_{A_c} \sigma_c (\kappa \cdot (z - h_1) + \varepsilon_c; \theta(y, z)) dA_c + \sum_{j=1}^{N_s} A_{sj} \sigma_s (\kappa \cdot (Z_{sj} - h_1) + \varepsilon_c; \theta(Y_{sj}, Z_{sj})) - N_u = 0 \quad (6)$$

In equation (6).  $\theta(y, z)$  denotes the temperature field for the analyzed time  $t$ ,  $Y_{sj}$ ,  $Z_{sj}$  are the coordinates for  $j$ -th reinforcing bar with an area of  $A_{sj}$ .

The ultimate value of bending moment  $M_u$  that corresponds to normal force  $N_u$  is the maximum value for the function  $M = M(\kappa)$ :

$$M_u = \max \left[ \iint_{A_c} \sigma_c (\kappa \cdot (z - h_1) + \varepsilon_c; \theta(y, z)) z dA_c + \sum_{j=1}^{N_s} A_{sj} Z_{sj} \sigma_s (\kappa \cdot (Z_{sj} - h_1) + \varepsilon_c; \theta(Y_{sj}, Z_{sj})) \right] \quad (7)$$

which is illustrated in Fig. 5.

It is worth mentioning that constructing  $M_u - N_u$  envelopes by the incremental-iterative procedure is a time-consuming process, requiring calculations based on solving  $n_i \times n_j$  equations ( $n_i$  denotes the number of levels of normal force  $N_u$  and  $n_j$  – number of considered curvatures) to determine the relationship  $M = M(\kappa)$  and find maximum values  $M_u$ . Hence, this approach is used mainly in theoretical analyses, usually as a reference method with which results obtained from other methods are compared.

### 3. Parametric study

In order to compare the results provided by the above described methods for determining fire load capacity, the parametric study for a few of the most commonly used in everyday design practice cross-sections of reinforced concrete elements was carried out. Two shapes of the cross-sections were analysed: square – with the dimensions of 30 cm × 30 cm and 40 cm × 40 cm and circular – with the diameters of 30 cm, 50 cm and 70 cm. The reinforcement of the square cross-sections consists of 8ø20 bars (reinforcement ratio  $\rho_s = 2.8\%$ ) and 8 ø25 bars ( $\rho_s = 2.5\%$ ) respectively for the 30 cm × 30 cm and the 40 cm × 40 cm elements. For the circular cross-sections, the reinforcement consists of 8ø16 ( $\rho_s = 2.3\%$ ), 8ø25 ( $\rho_s = 2.0\%$ ), 10ø32 ( $\rho_s = 2.1\%$ ), for diameters of 30 cm, 50 cm, 70 cm, respectively. The calculations were performed for normal strength concrete (NSC)  $f_c = 30$  MPa and high strength concrete (HSC)  $f_c = 90$  MPa for the elements with square cross-sections. In the case of the members with circular cross-sections, the compressive strength of 55MPa was taken into account. The yield strength of steel was the same for all considered cross-sections and equal to 420 MPa.

#### 3.1. Thermal analysis

Each element was heated uniformly along the perimeter according to the ISO834 time-temperature fire scenario. The heat transfer between the fire environment and a structural element is held by convection (Newton's Law) and thermal radiation (Stephan-Boltzman's Law). The physical parameters describing convective and thermal radiation heat fluxes at the element surface were taken to analysis according to Eurocode 1-1-2 [17]: the coefficient of heat transfer by convection  $\alpha_k = 25$  W/(m<sup>2</sup>K); emissivity of the heat source (fire)  $\varepsilon_f = 1.0$ ;

surface emissivity of a structural member  $\varepsilon_f = 0.8$ ; surface configuration factor equal to 1.0; Stephan-Boltzman constant  $\sigma_{S-B} = 5.67 \cdot 10^{-8} \text{ W}/(\text{m}^2\text{K}^4)$ .

Thermal profiles were obtained by solving the classical Fourier-Kirchhoff equation:

$$\frac{d\theta}{dt} \rho(\theta) c_p(\theta) = \nabla(\lambda(\theta) \nabla \theta) \quad (8)$$

where:

- $\rho$  – density of concrete,
- $c_p$  – specific heat and  $\lambda$  denotes thermal conductivity.

Numerical computations were carried out using the finite element code ANSYS [18] for the following thermal properties of concrete:

- for NSC, the thermal properties according to [3] were applied as for siliceous aggregate concrete with moisture content equal to 3% and the upper limit of thermal conductivity,
- for HSC, the thermal properties were taken according to [19] as for siliceous aggregate concrete.

The circular cross-sections were modelled in axisymmetry (temperature fields are only the function of radius), whereas for the square cross-sections, the two-dimensional analysis was conducted. For the sake of simplicity, the influence of steel on the thermal fields was neglected. The temperature of steel bars were taken equal the temperature of concrete at a centroid of the steel bar. The examples of calculated thermal fields are presented in Fig. 7 and 8 for circular and square cross-sections, respectively.

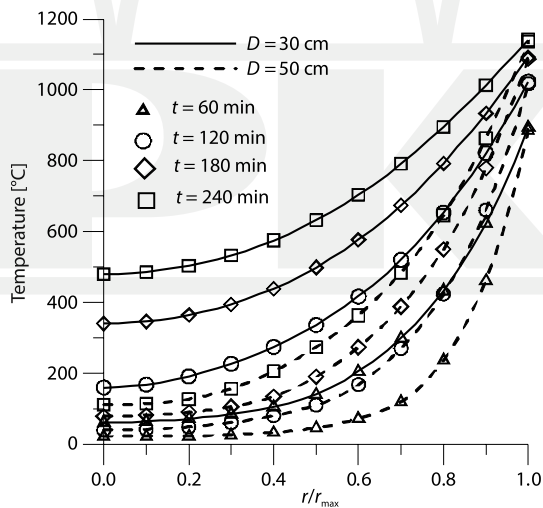


Fig. 7. Temperature profiles for circular cross-sections

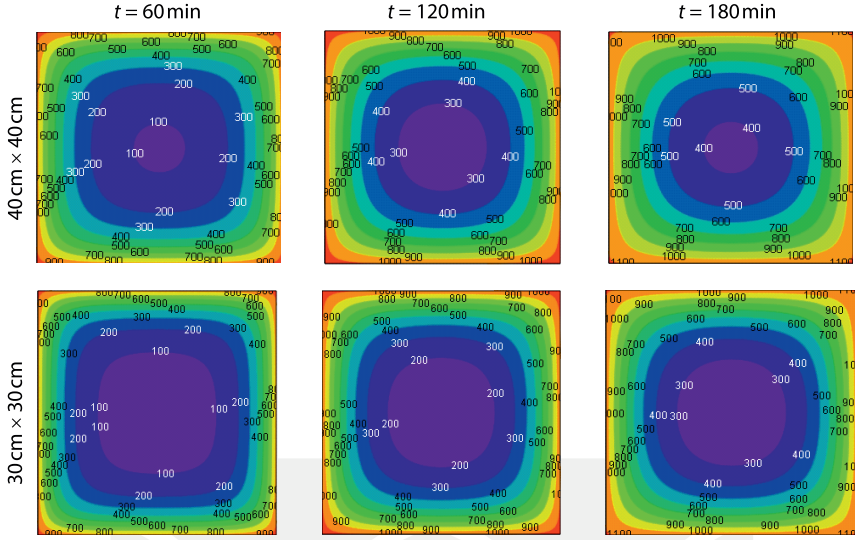


Fig. 8. Temperature profiles for square cross-sections

### 3.2. Mechanical analysis

The mechanical calculations were performed according to the assumptions listed in paragraph 2. For the 500°C isotherm method, the classical stress-strain relationships for concrete in the form of “Madrid parabola” [20] were used. The same  $\sigma_c - \varepsilon_c$  curves were applied to the zone method, although the compressive strength of concrete was reduced to  $k_c(\theta_M)f_c$ . The elastic ideal plastic physical relationships for steel with reduced yield strength to  $k_s(\theta_s)f_y$  were taken into account, both for the 500°C isotherm method and the zone method. Interaction envelopes  $M_u - N_u$  for the reduced dimensions of the analysed cross-sections were constructed according to the classical limit strain analysis for reinforced concrete sections at normal temperature [20].

The stress-strain relationships of concrete with the full softening branch were used for the reference method – incremental – iterative procedure. The pre-peak behaviour of NSC is described by the equations given in Eurocode 2-1-2 [3]. Since the Eurocode 2-1-2 [3] does not provide the formula for descending branch of  $\sigma_c - \varepsilon_c$  relationships, the following equation is proposed [21]:

$$\sigma_c(\varepsilon_c, \theta) = f_c(\theta) \cdot 10^{-p} \left( 1 - \frac{\varepsilon_{c1}(\theta)}{\varepsilon_c} \right)^2 \quad \varepsilon_c > \varepsilon_{c1}(\theta) \quad (9)$$

where  $\varepsilon_{c1}(\theta)$  is the strain at the peak in the  $\sigma_c - \varepsilon_c$  diagram and  $p = 3.0$ .

The pre-peak behaviour of  $\sigma_c - \varepsilon_c$  curves of HSC were taken from [22], however, the values of  $f_c(\theta)/f_c(20^\circ\text{C})$  and  $\varepsilon_{c1}(\theta)$  were assumed according to experimental results given in [23]. The post-peak behaviour of HSC was described by equation (9) with  $p = 2.5$ . The above

described stress-strain relationships are compared in Fig. 9 with experimental results for NSC [24, 25], and HSC [26], respectively. Temperature dependent stress-strain curves for steel were taken from [3] for hot rolled steel.

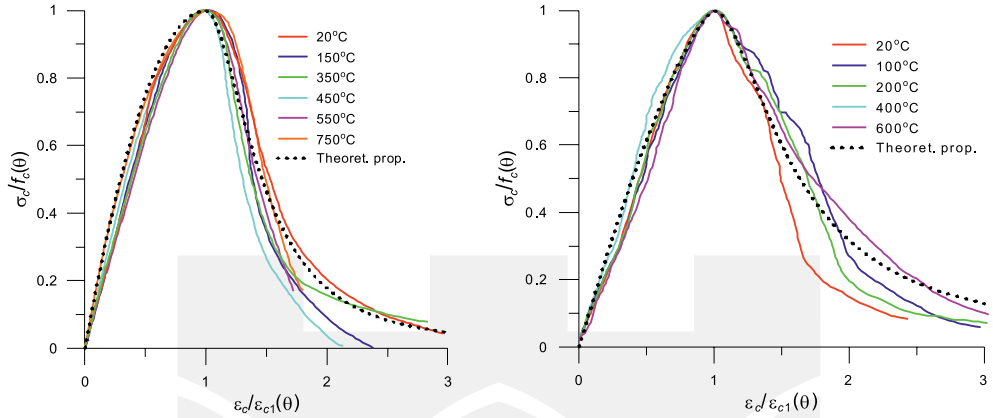


Fig. 9. Stress-strain relationship for concrete – theoretical proposition versus experimental tests: a) NSC [24, 25], b) HSC [26]

### 3.3. Results of calculations

The results of calculations in the form of bending moment – normal force envelopes for different periods of fire duration  $t$  are presented in Fig. 10 – for square cross-sections and in Fig. 11 – for circular ones. The incremental-iterative approach was used as a reference method.

In Fig. 10 a, c, e with red lines there are marked results obtained from incremental-iterative approach, with the black lines – from zone method and with blue lines – for 500°C isotherm method. As Eurocode 2-1-2 [3] does not include the method for reduction of circular cross-section for the zone method, the value of  $a_z$  was determined on the basis of the general assumption:

$$a_z = r \cdot \left( 1 - \sqrt{\frac{2 \sum_{i=1}^n \left( i - \frac{1}{2} \right) k_c(\theta_i)}{n^2 k(\theta_M)}} \right) \quad (10)$$

In all calculations carried out by means of the zone method, there was assumed the same number of cross-section divisions into zones:  $n = 6$ .

The changes in characteristic values for each interaction curve, i.e. the maximum bending moment, the maximum compressive force and the value of bending moment at the normal force equal to zero, are given in Fig. 11 and 12 b, d, f in the form of relative capacities defined in the following way:

$$\alpha_1 = \frac{N_{\max}^t}{N_{\max}^{t=0}}, \quad \alpha_2 = \frac{M_{\max}^t}{M_{\max}^{t=0}}, \quad \alpha_3 = \frac{M_{N=0}^t}{M_{N=0}^{t=0}} \quad (11)$$

where:

- $N_{\max}^t, M_{\max}^t, M_{N=0}^t$  – maximum compressive force, maximum bending moment and maximum bending moment for normal force equals zero carried out at the moment  $t$  of heating, respectively,
- $N_{\max}^{t=0}, M_{\max}^{t=0}, M_{N=0}^{t=0}$  – as above, but calculated for the beginning of the heating process of the element.

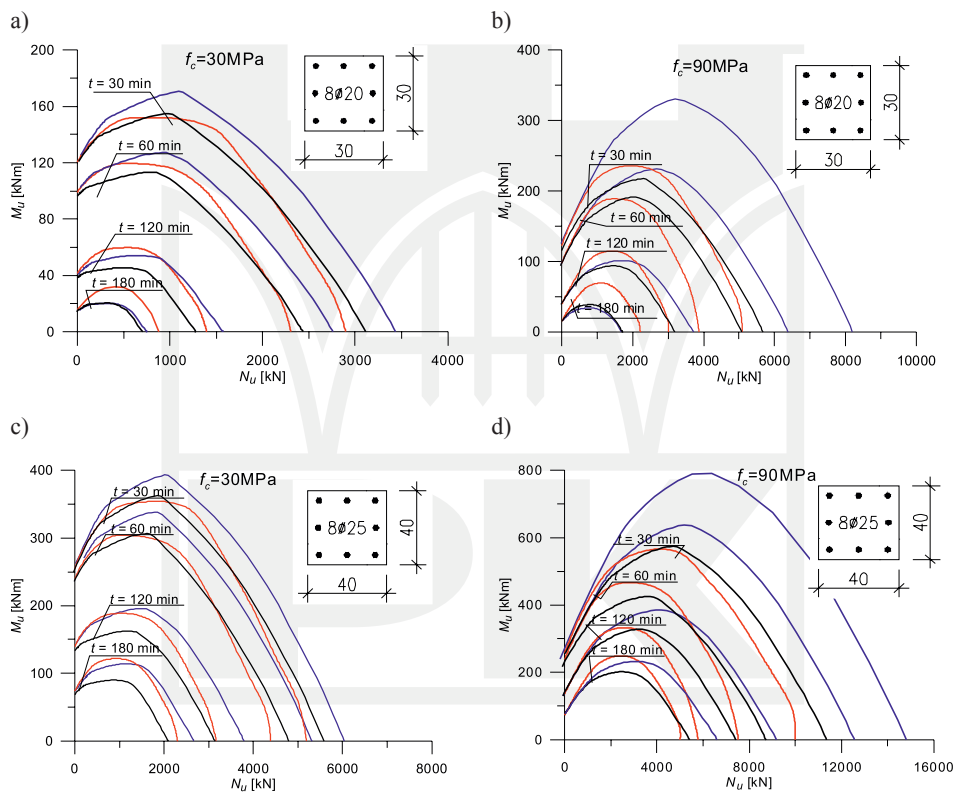


Fig. 10.  $M_u - N_u$  interaction envelopes for the incremental-iterative procedure (red line), the zone method (black line), and the 500°C isotherm method (blue line) – square cross-section

The resulting interaction curves are similar for all analysed types of cross-section. With the increase of heating duration, ultimate curves  $M_u - N_u$  are subjected to “shrinking” and deformation of shape.

All presented methods lead to similar results for cross-section subjected to a bending moment – see: Fig. 11 e, f and 12 f. This observation converges well with earlier results that were published in the literature [13–14]. Bent cross-sections with ratio of reinforcement of about 1% exhibit the tensile failure mode. The exertion levels of compressive zone of cross-section, plays a less significant role here despite the fact that it is also subjected to fire effects.

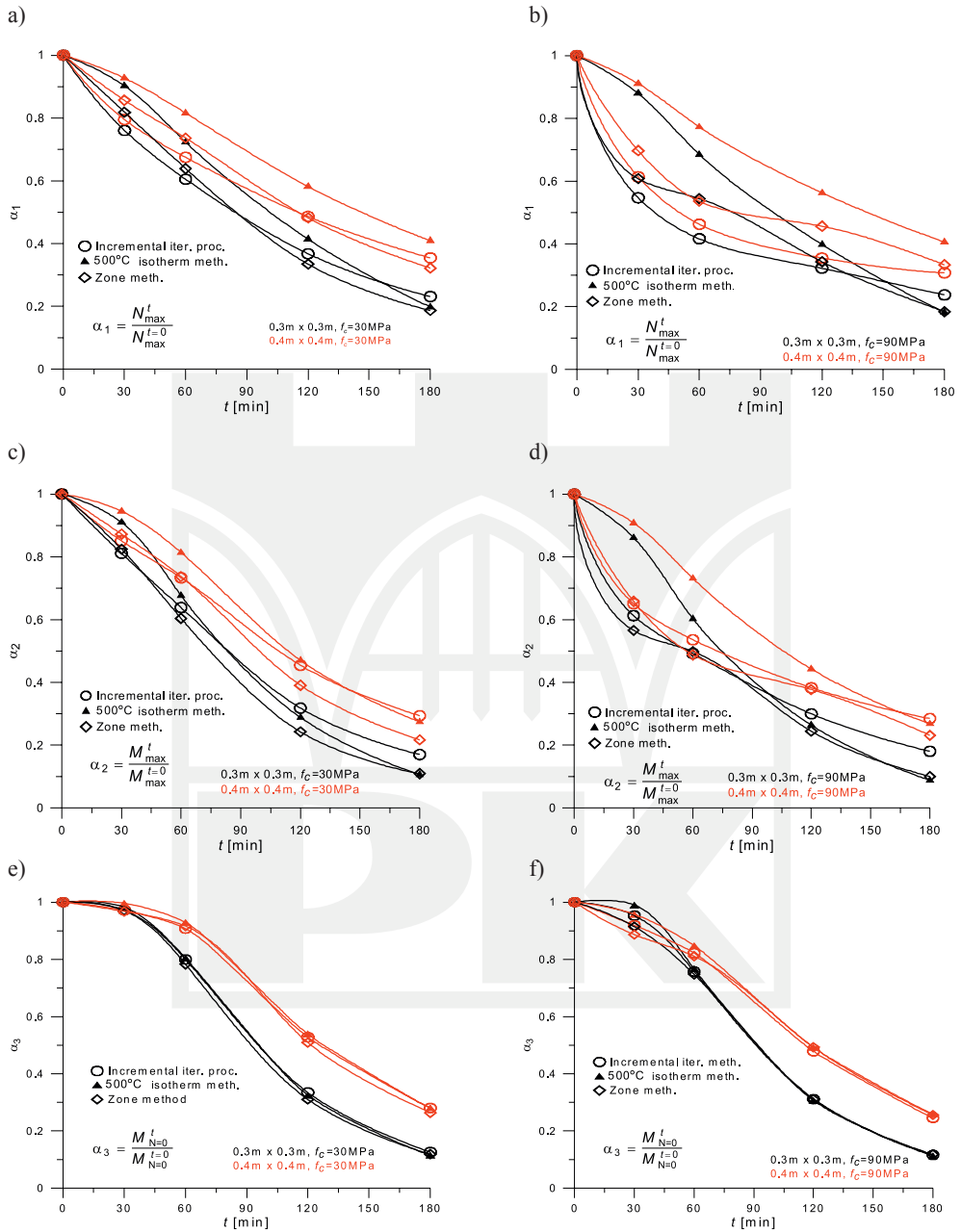


Fig. 11. Relative capacities for NSC members – a), c), e); HSC members – b), d), f)

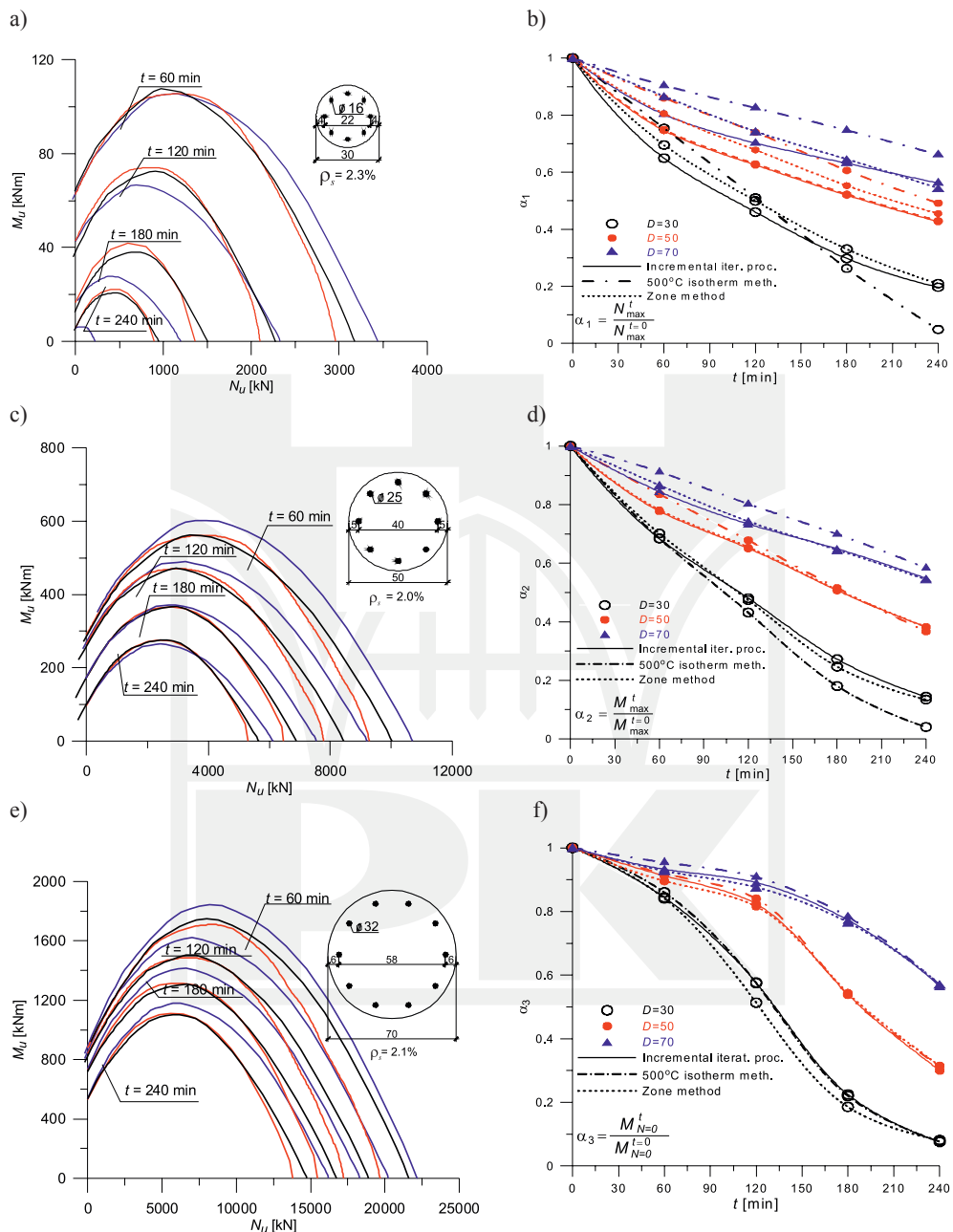


Fig. 12. a), c), e):  $M_u - N_u$  interaction envelopes for the incremental-iterative procedure (red line), the zone method (black line), and the 500°C isotherm method (blue line) – circular cross-section; b), d), e) – relative capacities

The differences in results between the incremental-iterative approach and the effective cross-section methods are observed for the cases where normal force is of great significance – see: Fig. 11 a–d and 12 b, d. It is especially important for elements made of HSC, where differences between incremental – iterative and 500°C isotherm methods are up to 40% for the unfavourable side of structural safety. For the zone method, differences are less important and do not exceed 15%, but they are also on the unsafe side.

#### 4. Comparison of calculations with results of experiments

The analysis of the results for fire resistance for reinforced concrete cross-sections obtained from different considered methods (500°C isotherm method, zone method and incremental-iterative approach) is supplemented by the comparison of calculated values and by results from experiments carried out on elements subjected to a normal force usually acting on an accidental eccentricity.

Fire tests provide information of vital importance as to the real behaviour of reinforced concrete structural elements during the action of high temperature. Results from tests may be directly used for determining or checking the necessary standard fire resistance for elements. But most of all, they are useful as the reference value for determining the accuracy and validity range for calculation methods for structural elements under fire conditions.

For the estimation of accuracy of the results from the analytical methods with experiments, there were selected tests presented in [27–31]. Some results were excluded from the comparative analysis as during the tests there were observed the phenomenon of explosive spalling of concrete that led to a premature failure of these elements in the conducted experiments. The total number of test results selected for the comparison was equal to 56, from which 27 elements were made of high strength concrete and 29 – from normal strength concrete.

For each of 56 considered columns, calculations of temperature distribution were carried out whilst taking into account the aggregate type used for the concrete mix and the appropriate value of compressive concrete strength. Thermal conductivity and specific heat for normal strength concrete on silicate aggregate were assumed in compliance with [3] as for concrete with humidity equal to 3%. For normal strength concrete on calcareous aggregate, the thermal conductivity was also taken based on [3], but specific heat was assumed according to [19]. Thermal properties for high strength concrete were taken from [19]. There was assumed the same fire scenario according to ISO834 standard fire time – temperature curve for all 56 elements. Thermal analyses did not take into account the influence of reinforcing steel and stirrups onto the resulting temperature fields. For elements made of normal strength concrete, calculations were conducted twice – with accounting for the upper and the lower limits of thermal conductivity. The temperature distribution that provided results closest to those obtained from experiments was chosen for further analysis.

The first series of tests used for the comparative study was carried out in the laboratories at the University of Ghent and University of Liège. Four types of cross-sections were investigated in the experiments: 20 cm × 20 cm, 20 cm × 30 cm, 30 cm × 30 cm, 40 cm × 40 cm and two different heights of columns 2.1 m and 3.9 m. All columns were made of normal strength concrete with gravel aggregate. The heating process was realized according to the

ISO 834 standard fire curve. A detailed description of the tests can be found in [27]. Due to severe spalling, the premature failure was observed in some columns. Those elements were excluded from the theoretical analysis. In the present study, only nine columns with square cross-section of 30x30cm and 40 × 40 cm are analysed.

The second set of tests was done in National Research Council in Canada [28–31]. The effects of a load level, end conditions (pinned or fixed), section sizes and shapes (square, rectangular, circular), reinforcing steel ratio (1.7–4.38%), concrete strength (28–127 MPa), concrete admixtures (steel or polypropylene fibres) and kinds of coarse aggregate (siliceous, calcareous) on fire resistance of columns were investigated. All columns had the same height of 3.81 m and were subjected to the ASTM 119 fire curve which is very similar to the standard fire time – temperature curve according to ISO 834. Only these columns with a square cross-section and dimension of 30.5 cm × 30.5 cm, 40.6 cm × 40.6 cm were used in the comparative study.

Columns constitute structural elements for which second order effects play an important role. In the literature, there are only a few reports on the simplified methods of taking into account second order effects in calculating fire resistance of compressed reinforced concrete elements. Appropriate proposals consist in application of classical Rankine – Merchant formula [10, 11] used for steel elements or in modification of national recommendations for calculating the columns in normal temperature conditions [4–7].

Due to the lack of methods for taking into account the second order effects, there was proposed the approach based on recommendation of Eurocode 2-1-1 [20] with determination of a buckling force on the basis of ACI 318-99 [32] and with modification being analogous to that presented in [6, 7]. The first order moment is multiplied by the factor:

$$\eta = 1 + \frac{\frac{\pi^2}{c_o}}{\frac{N_B}{N_u} - 1} \quad (12)$$

where:

$N_B$  – Euler buckling force,

$N_u$  – an applied load,

$c_o$  – a constant dependent on the first order moment distribution.

The Euler buckling force is calculated from the following equation:

$$N_B = \frac{\pi^2 \left( 0.2 I_c \cdot \iint_{A_c} E_{cm}(\theta(y, z, t)) dA + I_s \cdot \sum_i E_s(\theta_i) \right)}{l_o^2} \quad (13)$$

In eq. (13)  $I_c$ ,  $I_s$  are moments of inertia for concrete and steel sections, respectively,  $E_{cm}(\theta)$  is the temperature dependent concrete elasticity modulus,  $E_s(\theta)$  is the steel elasticity modulus,  $\theta(y, z, t)$  is the temperature field,  $\theta_i$  is the temperature of  $i$ -th bar,  $l_o$  is an effective length of column.

The load bearing capacity is strongly dependent on an accidental eccentricity  $e_{imp}$ . For the present computations,  $e_{imp} = 0.005$  m was used for all analysed elements.

The comparison of the experimental results and calculated (theoretical) values obtained by the discussed methods for the considered set of cases is presented in Fig. 13. The calculated values of fire resistances  $N_{calc}$  in most of the analysed examples differ from the test results  $N_{exp}$ . One of the reasons of this fact is that there is a lack of experimental data for physical properties of concrete used for experiments. The assumed thermal properties were taken from the literature which results in differences between the measured and calculated temperature distributions in the cross-sections. Moreover, during the initial phase of heating, there was observed (especially for HSC elements) local and surface thermal spalling. This effect, which results in faster heating of reinforcing steel bars and increased penetration of the heat within the cross-section, was not considered in the calculations.

The results obtained from the incremental-iterative approach, are the closest to the experimental ones, both for NSC and for HSC – Fig. 13 e, f. The mean value of the  $N_{calc}/N_{exp}$  distribution for this method is the closest to 1.0 with the lowest variation coefficient obtained. The methods of the effective cross-section – the 500°C isotherm method and the zone method – lead to the reliable results only for elements made of NSC (Fig. 13 a, c).

The analysis of  $N_{calc}/N_{exp}$  distributions for HSC elements – Fig. 13 b, d – indicates that the methods of the effective cross-section provide an unreliable estimation of fire load capacity. This is particularly true for the 500°C isotherm method which in most cases leads to meaningful under-estimation or over-estimation of fire resistance.

## 5. Summary and conclusions

The analysis of reinforced concrete members subjected to a fire action may be performed by many methods with different levels of complexity and accuracy. On the simplest practical level, descriptive methods in the form of tabulated data may be applied, but only within the ranges specified by appropriate codes. On the other hand, in recent years there has been observed significant progress in working out more and more sophisticated methods for the fire design of reinforced concrete members, taking advantage of modern computational tools and advanced material modelling.

In the paper, the emphasis was placed onto simplified methods for determining fire load capacity of reinforced concrete sections subjected to bending moment and normal force (also called engineering methods), which can be located between the two aforementioned extreme approaches. Despite advanced thermal and mechanical models for reinforced concrete elements (or the whole structures), there is still a strong need for developing and improving simplified design methods for everyday practices that are usually limited to more typical engineering solutions. Such methods should allow an engineer to exert control over calculation procedures carried out for fire design situations and may also constitute initial designs for complex, non-typical structures.

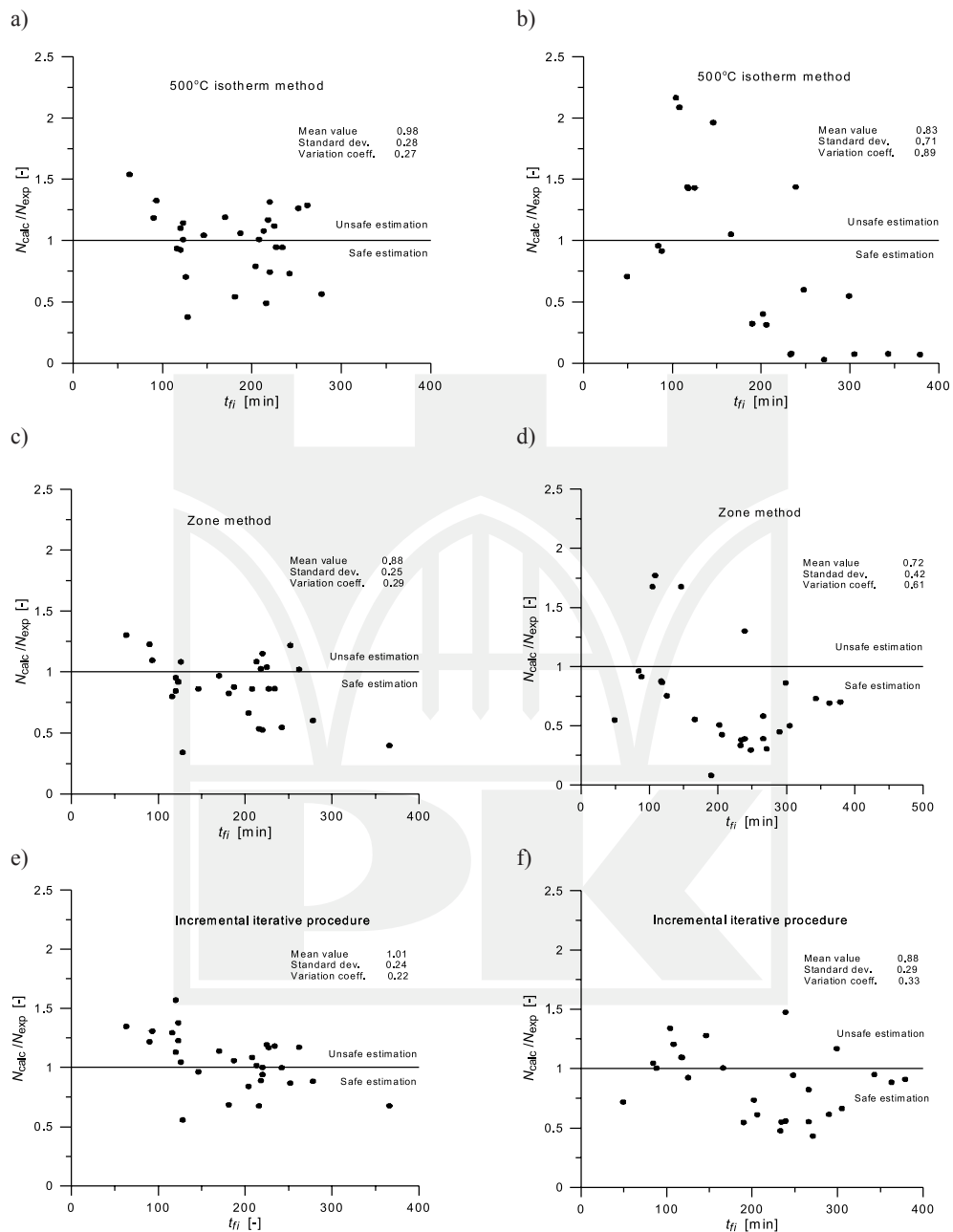


Fig. 13. Comparison of calculation and experimental results for NSC columns a), c), e) and HSC columns b), d), f) for the analysed methods

The simplified methods that were presented, discussed and compared in the paper include those given in Eurocode 2-1-2 – two methods based on the effective cross-section (500°C isotherm method and zone method) and incremental-iterative approach. The basic aim of the conducted analysis was to compare results obtained by those different methods (treating the incremental-iterative approach as the reference method) as well as to compare calculated values of fire resistance with the experimental results for reinforced concrete columns taken from the literature, which would make it possible to evaluate the accuracy and possible safe range of the application of considered methods. Major variables in the parametric study were: concrete class (NSC, HSC), values of normal force eccentricity, cross-section shape and reinforcement ratio. The following general conclusions can be drawn from the conducted analysis:

The discussed methods provide similar results in the form of  $M_u - N_u$  envelopes for all analysed cross-section shapes and concrete classes but only for load cases close to pure bending. When normal force accompanies the bending moment, there are observed significant differences in results, especially for HSC members. Taking the incremental-iterative approach as a reference method, the difference may reach 40% for the isotherm method and 15% for the zone method – in both cases for unfavourable side of structure safety. This observation converges quite well with the findings of other researchers [13–14]. The differences in results obtained from the 500°C method for HSC members may to some extent be reduced by assuming a lower than 500°C level of limit temperature (as high strength concretes are characterized with faster reduction in compressive strength with increasing temperature in comparison with normal strength concrete) [14].

- In comparison with experimental results, the incremental-iterative approach indicates relatively constant levels of accuracy within the whole analysed range of concrete class expressed by similar values of  $N_{calc}/N_{exp}$  distribution parameters. For the methods of the effective cross-section, the differences between calculated and experimental results are more pronounced with significant dispersion of  $N_{calc}/N_{exp}$  values, especially for HSC columns.
- The methods of the effective cross-section are to be considered as reliable only for elements made of NSC and generally subjected to bending. For normal force that accompany bending moments and for HSC members, they may significantly over or under-estimate fire resistance (in particular – the 500°C isotherm method).
- Incremental-iterative procedures applied for determining  $M_u - N_u$  interaction curves provide results closest to experimental ones within the whole analysed range of variables (concrete class, amount of reinforcement, duration of fire action, cross-section shape). Although this constitutes a more time-consuming process than designs based on effective cross-section methods, in general, it may operate with different real stress-strain relationships for materials (structural concrete and reinforcing steel) thus giving a possibility to account for variation in basic parameters for the whole set of materials used.

## References

- [1] *Fire Design of Concrete Structures – materials, structures and modelling. fib bulletin 38*, Lausanne, Switzerland, April 2007.
- [2] EN 1990:2004 Eurocode. Basis of Structural Design, European Committee For Standardization, Brussels 2002
- [3] EN 1992-1-2:2004. Eurocode 2: Design of concrete structures – Part 1.2: General rules – Structural fire design, European Committee For Standardization, Brussels 2004.
- [4] Dotreppe J.-C., Fransen J.M., Vanderzeypen Y., *Calculation method for design of reinforced concrete columns under fire conditions*, ACI Structural Journal, 96 (1), January-February 1999.
- [5] Franssen J.-M., Dotreppe J.-C., *Fire tests and calculation methods for circular concrete columns*, Fire Technology, 39 (1), January 2003.
- [6] Tan K.H., Yao Y., *Fire resistance of four-face heated reinforced concrete columns*. Journal of Structural Engineering, 129 (9), September 2003.
- [7] Tan K.H., Yao Y., *Fire resistance of reinforced concrete columns subjected to 1-, 2-, and 3-face heating*, Journal of Structural Engineering, 130 (11), November 2003.
- [8] *Fire Design of Concrete Structures – structural behaviour and assessment. fib bulletin No. 46*, Lausanne, Switzerland, April 2008.
- [9] *Fire Design of Concrete Structures in Accordance with CEB/FIP Model Code 90. CEB Bulletin D'Information No. 208*, Lausanne, Switzerland, July 1991.
- [10] Tan K.H., Tang C.Y., *Interaction formula for reinforced concrete columns in fire conditions*, ACI Structural Journal, 101 (1), January-February 2004.
- [11] Tan K.H., Yao Y., *Rankine method for reinforced concrete columns under fire conditions*, In Proceedings of the 18th Australian Conference on the Mechanics of Structures and Materials, Developments in Mechanics of Structures and Materials, vol. 1, Perth, Australia, December 2004.
- [12] Andenberg Y., *Analytical fire design of reinforced concrete structures based on real fire characteristics*, In FIB Eight Congress Proceedings, Part 1, London 1978.
- [13] Bamonte P., Meda A., *Towards a simplified approach for the sectional analysis of R/C members in fire*, In Proceedings of the 2nd International Congress Keep Concrete Attractive, Naples, Italy, June 5–8 2005.
- [14] Meda A., Gambarova P.G., Bonomi M., *High-performance concrete in fire-exposed reinforced concrete sections*, ACI Structural Journal, 99 (3), May-June 2002.
- [15] Seręga S., *A new simplified method for determining fire resistance of reinforced concrete sections*, In Proceedings of 6th International Conference Analytical Models and New Concepts in Concrete and Masonry Structures, 2008.
- [16] Hertz K.D. *Design of fire exposed concrete structures*, Technical Report no. 160, CIB W15/81/20(DK), Technical University of Denmark, Lyngby 1981.
- [17] EN 1991-1-2:2004 Eurocode 1: General Actions – Actions on structures exposed to fire. European Committee For Standardization, Brussels 2002.
- [18] Kohnke P., editor, *ANSYS, Inc. Theory Manual Twelfth Edition*, 1994.
- [19] Kodur V.K.R., Sultan M.A., *Effect of temperature on thermal properties of high-strength concrete*, Journal of Materials in Civil Engineering, 15 (2), April 2003.
- [20] EN 1992-1-1: Eurocode2: Design of concrete structures – Part 1: General rules and recommendations for buildings. European Committee for Standardization, Brussels, 2004.

- [21] Seręga S., *Behaviour of high performance concrete columns at fire temperatures*, PhD thesis, Cracow University of Technology, 2009, in Polish.
- [22] Kodur V.K.R., Wang T.C., Cheng F.P., *Predicting the fire resistance behaviour of high strength concrete columns*, *Cement & Concrete Composites*, 26 (2), February 2004.
- [23] Cheng F.P., Kodur V.K.R., Wang T.C.W., *Stress-strain curves for high strength concrete at elevated temperatures*, *Journal of Materials in Civil Engineering*, 16 (1), January-February 2004.
- [24] Schneider U., *Behaviour of concrete at high temperatures*, *Deutscher Ausschuss für Stahlbeton*, 337, 1982.
- [25] Schneider U., *Modelling of concrete behaviour at high temperatures*, [w:] R.D. Anchor, H.L. Malhotra, J.A. Purkiss, editors, *Design of structures against fire*, 1986.
- [26] Fu Y.F., Wong Y.L., Poon C.S., Tang C.A., *Stress-strain behaviour of high-strength concrete at elevated temperatures*, *Magazine of Concrete Research*, 57 (9), November 2005.
- [27] Dotreppe J.-C., Franssen J.M., Braus R., Vandeveld P., Minne R., Van Nieuwenburg D., Lambotte H., *Experimental research on the determination of the main parameters affecting the behaviour of reinforced concrete columns under fire conditions*, *Magazine of Concrete Research*, 49(179), June 1996.
- [28] Kodur V.K.R., Cheng F.P., Wang T.C., Latour J.C., Leroux P., *Fire resistance of high-performance concrete columns*, Technical Report No. 834, National Research Council, Institute for Research in Construction, Ottawa, December 2001.
- [29] Kodur V.K.R., McGrath R., Latour J.C., MaClaurin J., *Experimental studies on the fire endurance of high-strength concrete columns*, Technical Report No. 919, National Research Council, Institute for Research in Construction, Ottawa, October 2000.
- [30] Kodur V.K.R., McGrath R., Leroux P., Latour J.C., *Experimental studies for evaluating the fire endurance of high-strength concrete columns*, Technical Report No. 197, National Research Council, Institute for Research in Construction, Ottawa, May 2005.
- [31] Lie T.T. Wooleton J.L., *Fire resistance of reinforced concrete columns – test results*, Technical Report No. 596, National Research Council, Institute for Research in Construction, Ottawa 1988.
- [32] Building code requirements for structural concrete (ACI 318-99) and commentary (ACI 318R-99), American Concrete Institute, 1999.

WIT DERKOWSKI, ARKADIUSZ KWIECIEŃ, BOGUSŁAW ZAJĄC\*

## CFRP STRENGTHENING OF BENT RC BEAMS USING STIFF AND FLEXIBLE ADHESIVES

### WZMOCNIENIE ZGINANYCH ELEMENTÓW ŻELBETOWYCH PRZY UŻYCIU CFRP NA SZTYWNYCH I PODATNYCH KLEJACH

#### Abstract

The paper presents new research on the use of a flexible adhesive layer in CFRP strengthening applications for bent RC beams, which was carried out at the Cracow University of Technology. The Flexible Joint Method, developed at the Cracow University of Technology, uses PU polymers as adhesives in bonding FRP composites to concrete structures. In the tests, reinforced concrete beams were strengthened with CFRP strips, using an epoxy adhesive and five kinds of polymer adhesives of different flexibility. The beam strengthened by means of CFRP strips on middle hard flexible polymer, demonstrates the most uniform CFRP strain distribution along its length and the smallest deflection. The use of the presented technology could allow for the overcoming of some obstacles which occur when repairing concrete structures, however it is obvious that a lot of tests on such adhesives have to be carried out.

*Keywords: CFRP strengthening, polymer flexible adhesive, RC structures, displacement reduction, laminate slip*

#### Streszczenie

W artykule przedstawiono badania belek żelbetowych wzmocnionych taśmami CFRP aplikowanymi na podatnych złączach. Metoda złączy podatnych, opracowana na Politechnice Krakowskiej, polega na stosowaniu polimerowych warstw adhezyjnych przy łączeniu materiałów CFRP z podłożem betonowym. W badaniach belki żelbetowe wzmocniono taśmami CFRP klejonymi na warstwie epoksydowej i pięciu warstwach polimerowych o różnych sztywnościach. W belce wzmocnionej taśmą CFRP na warstwie polimerowej o średniej sztywności wykazano najbardziej równomierny rozkład odkształceń taśmy na jej długości i równocześnie najmniejsze jej ugięcie spośród wszystkich badanych belek. Stosowanie omawianej technologii we wzmacnianiu konstrukcji z betonu może przynieść dodatkowe korzyści, ale obecnie konieczne są dalsze badania nad tym zagadnieniem.

*Słowa kluczowe: wzmocnienie CFRP, podatne złącza polimerowe, żelbet, redukcja ugięć, poślizg taśmy*

\* PhD. Wit Derkowski, Institute for Building Materials and Structures, Civil Engineering Faculty, Cracow University of Technology, PhD. Arkadiusz Kwiecień, PhD. Bogusław Zajęc, Institute of Structural Mechanics, Civil Engineering Faculty, Cracow University of Technology.

## 1. Introduction

Many of the existing structures require repairs or strengthening. The need to increase bearing capacity or serviceability of a whole structure or its part is usually connected with the increase of acting live loads (for example: a change in the load class for a bridge), mechanical damages, ageing or corrosion of materials, a change of static system and sometimes design or execution errors.

Since the early 1990s, fiber reinforced plastics (FRP) glued on epoxy adhesives have been used for external strengthening of reinforced concrete structures. This solution is proven to be an economically competitive alternative to traditional methods of repair, especially where durability and speed of construction are of primary concern. Many scientific research centers are involved in extensive research projects on the behavior of structures strengthened with those materials. Unfortunately, strengthening of reinforced concrete bent elements with externally bonded FRP laminates is not fully effective because of the stress concentrations appearance in adhesive layer. The advantages of CFRP materials are not fully utilized because of the low tensile and shear surface strength of adherent materials like epoxy resins. Shear and normal interfacial stress peaks occur in this layer at the end of CFRP plates or in discontinuous places (cracks).

The possibility for use of a flexible adhesive layer in CFRP strengthening applications for flexural strengthening of reinforced concrete elements as an innovative solution in civil engineering, is presented in this paper. A brief description is given of experimental research carried out at the Institute for Building Materials and Structures at the Cracow University of Technology, where five RC beams strengthened with CFRP strips on various polymer adhesives were tested under monotonic load. The research done so far has shown that the use of flexible polymer joints, made of polyurethane mass, reduces the peaks of stress concentration and can become an effective method in the repair of concrete structures [1].

## 2. Flexible joint method application in adhesive layer

### 2.1. Stiff and flexible adhesives

Epoxy resin adhesives, which are widely used in FRP strengthening technologies, are relatively stiff. They have high shear and tensile strength (up to 30 MPa) but they have a low ultimate range of strain (under 4%), and thus are inappropriate in applications where high deformability or high stress concentrations exist. On the other hand, polymer flexible adhesives made of polyurethane mass (PU) are of elastomeric behaviour and have the ultimate strength of several MPa but the ultimate range of strain over several dozen percentage points or several hundred percentage points. Adhesive joints made of polyurethanes are characterized by a higher value of deformation energy and ductility than epoxies, which can be measured by the area under the curves of  $\sigma - \varepsilon$  [2].

## 2.2. Reduction of stress concentration by flexible adhesives

The Flexible Joint Method, developed at the Cracow University of Technology, uses PU polymers as adhesives in bonding FRP composites to concrete and masonry substrates. This method is registered in the Polish Patent Department as No. P-368173. The proper selection of polymer properties is very important in the flexible bonding of FRP to concrete substrates. Two approaches are adopted in using flexible polymers. In the first approach, the newly constructed polymer joint is assumed to be of higher strength than the substrate (concrete elements) but the flexibility of the polymer causes a reduction of stress concentration thereby increasing the strength of the structure [3]. In the second approach, the newly constructed polymer joint is assumed to be of lower strength than the substrate to assure no damage appears in the joined structural elements. In bending of RC beams, stress concentrations attack the adhesive layer and next FRP in places where cracks appear in the concrete zone between FRP reinforcement and steel reinforcement. Because of the brittleness of typically joining materials (epoxy resins), the peak of stress concentration exists at the boundary of the crack (Fig. 1) and it is higher the stiffer the adhesive is [4].

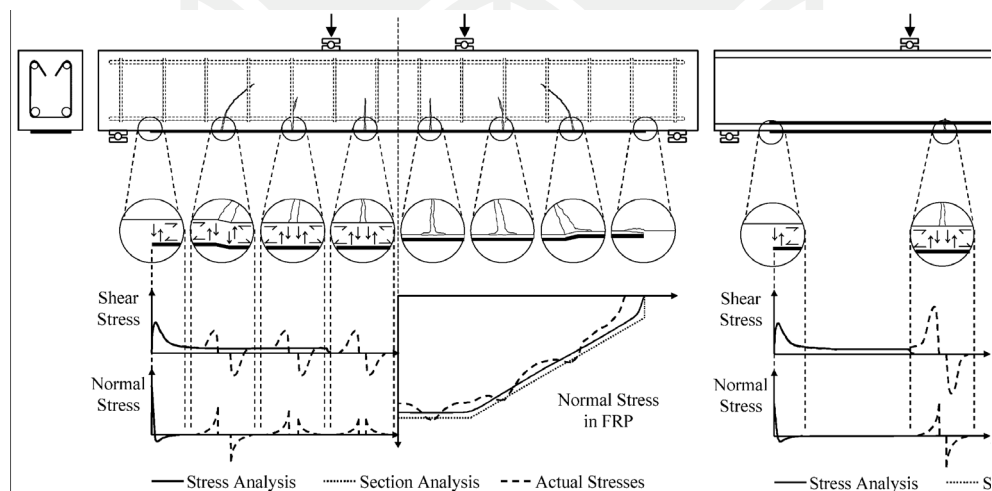


Fig. 1. Stress concentrations at boundary of cracks [7]

In these critical points (Fig. 2a), debonding occurs when the local deformation of the FRP strip is greater than can be carried by the bond between the strip and concrete substrate. After the cracking of the stiff adhesive layer, the notch effect is active (Fig. 2b). There are two modes of failure [5]: debonding of the laminate from its end and mid-span shear debonding (Fig. 2a). Tests of polymer flexible adhesive layers bonding CFRP laminates to a concrete substrate [6] showed that the use of flexible polymer adhesives allows stress concentrations to be reduced in places where the notch effect acts and thus protects CFRP laminates against failure (Fig. 3).

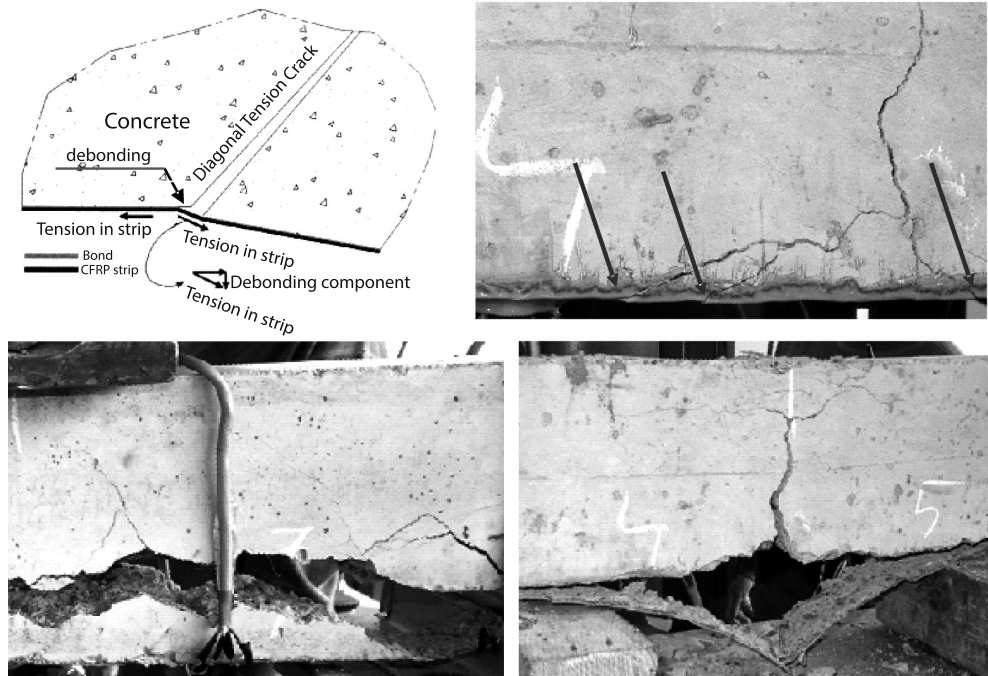


Fig. 2. Failure in a beam strengthened with CFRP laminate bonded on stiff epoxy resin adhesive: a) scheme of debonding [7], b) local damages of epoxy adhesive (notch effect) generating high stress concentrations [6]

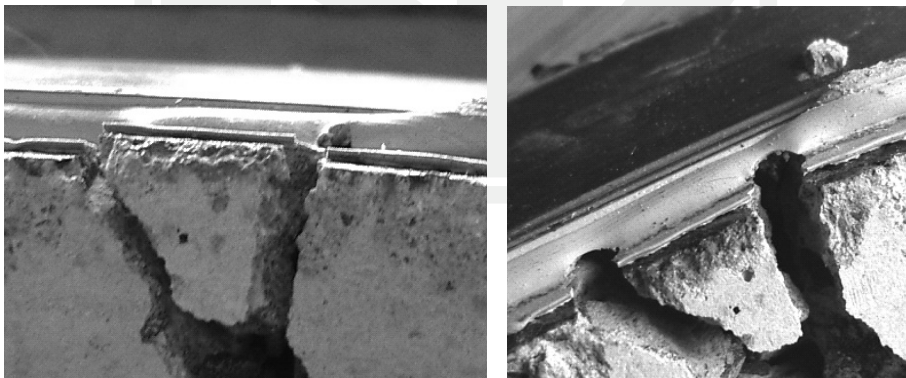


Fig. 3. Protection of CFRP laminate against stress concentration by flexible polymer adhesive

### 3. Description of experimental investigation

To find more information about the work of polymer flexible adhesives in comparison with the traditionally used stiff adhesives made of epoxy resin, new laboratory tests were carried out at the authorized Testing Laboratory for Building Materials and Structures at the Cracow University of Technology.

#### 3.1. Tested beams

Reinforced concrete beams of the same geometry, were investigated during the experimental research. The beams had a total length of 3,20 m and a rectangular cross-section ( $h = 25$  cm,  $b = 15$  cm). All the beams were cast at the same time from the same materials. Concrete grade C30/37 and reinforcing steel grade RB500W (design yield strength  $f_{yd} = 500$  MPa) were used. The longitudinal tensile reinforcement consisted of two 8 mm rebars and the transverse reinforcement was selected to ensure a flexural failure of the beam.

One non-strengthened beam and five strengthened ones with CFRP S512 strips ( $E \geq 165$  GPa,  $\epsilon_u = 1,7\%$ ) on different adhesive layers were tested. The bottom face of the beams were prepared for strengthening by sand blasting. One end of the CFRP laminate was always additionally fixed to the beam, using CFRP unidirectional sheet.

All specimens were tested in a 4-point bending test and forces were located 1,0 m from the supports. The beams were loaded by means of electronically controlled hydraulic IST pulsator with displacement control of constant velocity of 2 mm/minute, up to the beam

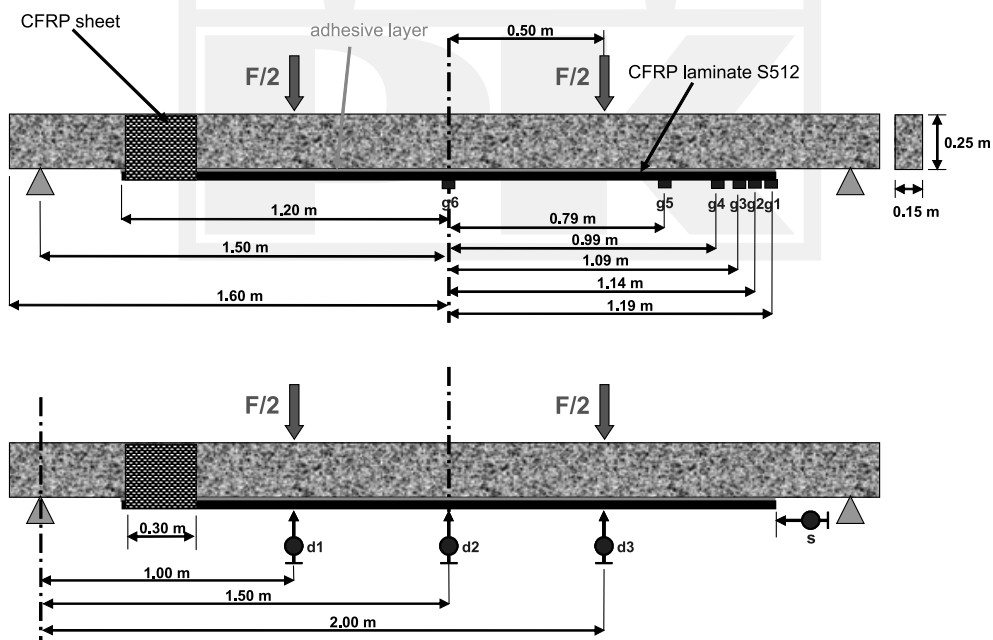


Fig. 4. Test setup for strengthened beams (g1-g6 – strain gauges, s and d1-d3 – LVDT sensors)

failure. Continuous data acquisition (the values of time, external force, deflections, CFRP strain and end slip) was carried out with the electronic HBM devices connected to a PC. The deflections were measured with three LVDT gauges located at the midspan of the beam and under the load forces. The CFRP laminate strains were measured at one half of the laminate, not fixed on its end, with foil electric resistance strain gauges. The scheme of a strengthened beam and measurement points are presented in Fig. 4.

### 3.2. Characteristics of adhesive materials used

In tests of RC beams strengthened with the CFRP laminates S512, one kind of epoxy adhesive Sikadur 30 (E) and four kinds of PU adhesive: hard flexible polymer (PT), middle flexible polymer (PS), middle hard flexible polymer (PST) and middle soft flexible polymer (PSM) were used. The list of properties of tested adhesives (manufacturer's data) are presented in Table 1.

Table 1

**Mechanical properties of tested adhesives**

	Type of adhesive				
	E	PT	PS	PST	PSM
Young's modulus [MPa]	12 800	600	8	6	2.5
Tensile strength [MPa]	28	18	2.2	2.5	1.6
Shear strength [MPa]	18	18	0.8	1.2	1.6
Elongation [%]	0.22	10	45	110	150
Adhesion to concrete [MPa]	> 4	> 5	3.2	2.2	2.0

## 4. Analysis of obtained results

### 4.1. Comparison of obtained values and damage forms

The results obtained during the tests for the beams, described with symbols characteristic of each type of adhesive layers are presented in Table 2.

The failure of each strengthened beam was caused by a diagonal shear crack, localized close to the force loading point. For the strengthened beams, delamination of the CFRP laminates was observed. For the E and PT beams, the cohesive failure was localized in the concrete substrate (Fig. 5–6) and for the PS, PST and PSM beams, the cohesive failure was localized in polymer adhesive (Fig. 7–9).

In the case of the E, PS and PST, beams failures in the form of slip occurred at the laminate parts protected against debonding from its end, using CFRP sheets. In the case of the PT and PSM beams, failures occurred at the free part of laminates (Table 2). Protection was used to assure debonding failure at the site of the beam with strain gauges, but the stiffening effect caused an unexpected form of failure.

Table 2

**Maximum force, displacement and deformation energy of each tested beam**

	Type of tested beam					
	RC	E	PT	PS	PST	PSM
Max. force $F_{max}$ [kN]	25.6	59.7	65.5	64.7	54.4	48.7
Displacement at $F_{max}$ [mm]	30.0	33.9	37.4	28.6	29.9	29.1
Deformation energy – eq. (1) $W$ [1 J = 1 Nm]	629	1245	1461	1133	1065	942
Energy ratio [-]	$W_{RC}/W_E$ 0.50	$W_E/W_E$ 1	$W_{PT}/W_E$ 1.17	$W_{PS}/W_E$ 0.91	$W_{PST}/W_E$ 0.85	$W_{PSM}/W_E$ 0.75
Failure mode	yielding of reinforcing bars	delamination at fixed end	delamination at free end	delamination at fixed end	delamination at fixed end	delamination at free end

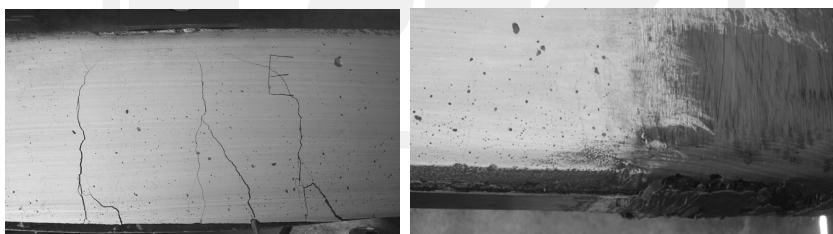


Fig. 5. Damages of beam (E) strengthened with CFRP bonded on epoxy adhesive



Fig. 6. Damages of beam (PT) strengthened with CFRP bonded on polymer adhesive

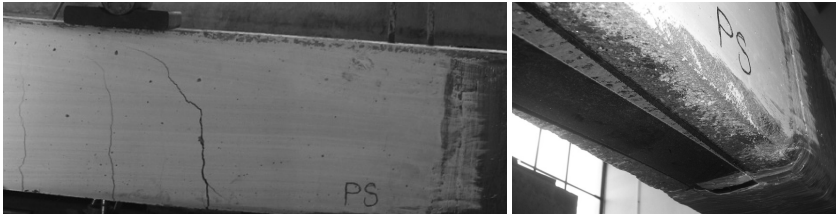


Fig. 7. Damages of beam (PS) strengthened with CFRP bonded on polymer adhesive

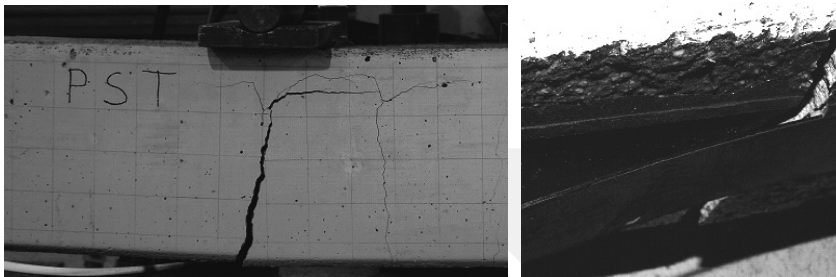


Fig. 8. Damages of beam (PST) strengthened with CFRP bonded on polymer adhesive



Fig. 9. Damages of beam (PSM) strengthened with CFRP bonded on polymer adhesive

#### 4.2. Comparison of measurements

The diagram presenting vertical displacements of beams (measured at point d2 – Fig. 4) versus loading force (Fig. 10) enables a comparison of the work of the maximum force (deformation energy), calculated according to equation (1). The characteristic values of the curves are compared in Table 2.

$$W = \int_0^{\text{displacement\_at\_}F_{\max}} F dy \quad (1)$$

where:

- $F$  – loading force changing from 0 to  $F_{\max}$ ,
- $y$  – deflection (vertical displacement).

Polymer adhesives PT and PS assure a higher value of maximum force than epoxy ones (E) and comparable values of deformation energy indicate that polymer flexible adhesives (PT and PS) are as efficient as epoxy resin adhesives. Polymer adhesives PST and PSM are of a slightly worse parameters than adhesives E, PT and PS.

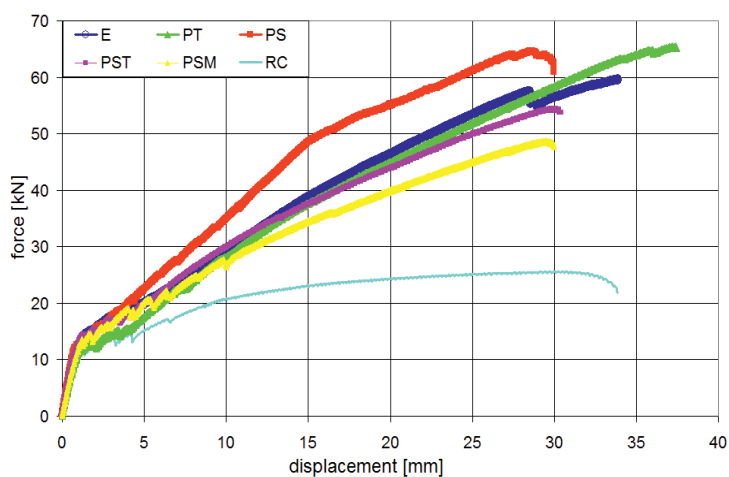


Fig. 10. Force-displacement curves of tested beams

The charts of CFRP end slips (measured at point  $s$  – see Fig. 4) versus applied load for the strengthened beams are given in Fig. 11. The occurrence of a much higher CFRP end slip is proportional to elongation and inversely proportional to stiffness (Young's modulus) of adhesives (Table 1). The curves of CFRP slip, characteristic of the tested adhesives, confirm that flexible adhesives deform significantly along all bonding surface, even if the load is low. As shown in the chart, for beam E the strip's end slip was practically associated with the loss of beam capacity (CFRP debonding). For all the beams strengthened with polymer joints, the end slip was noticeable, but did not involve direct loss of beam capacity. Even with the stiffest of the polymer joints used (beam PT), where the slip of CFRP laminate did not occur until the final phase of the test, flexibility of the adhesive layer helped to increase the scope of the beam work in relation to the stiff joint (beam E). The adhesive used in the PSM beam proved to be so soft that an increase of the end slip was observed from the very beginning of the test, and in the final stage of the test, the strip end displacement was so big that a measuring disturbance occurred as a result of sensor tip drifting.

The graphic comparisons of the CFRP laminate strain distribution measured at force level 40 kN is presented in Fig. 12 (diagrams concern half of the length of the laminate and the distance was measured out from the midspan of the beam). Strains were measured at points  $g_1, g_2, g_3, g_4, g_5, g_6$  located on the axis of the CFRP laminate – distances between the points are shown in Fig. 4. The discontinuity of the graph for the PT beam results from damage to the strain gauge  $g_3$ , located 11 cm from the strip end.

This graph shows that applying flexible polymer adhesives in FRP strengthening systems results in more uniform CFRP strain distribution along its length in relation to stiff (epoxy) adhesive. In the case of the epoxy bond, the end of the strip is practically unloaded.

The graphic comparisons of the CFRP laminate strain changing with the load level are presented in Fig. 13–18. These graphs show that applying flexible polymer adhesives in FRP strengthening systems results in a more regular CFRP strain distribution with load level changing in relation to the stiff (epoxy) adhesive. Generally, strain distributions of CFRP laminates bonded on flexible polymer adhesives are comparable to the distribution obtained for the stiff epoxy adhesive classically used.

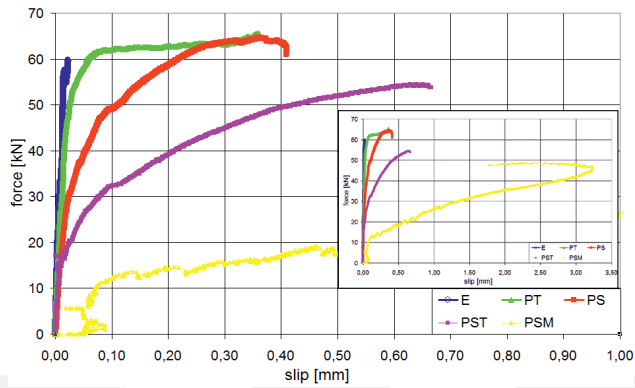


Fig. 11. Force-slip curves of the CFRP end obtained on strengthened beams in scale up to 3.5 mm and up to 1.0 mm

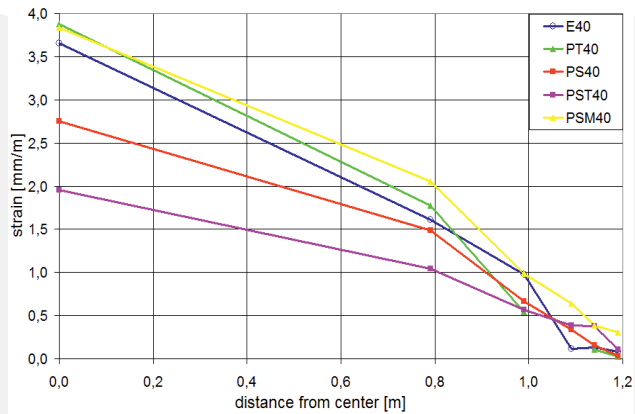


Fig. 12. Distribution of CFRP strain along its length obtained on reinforced beams under loading force  $F = 40$  kN

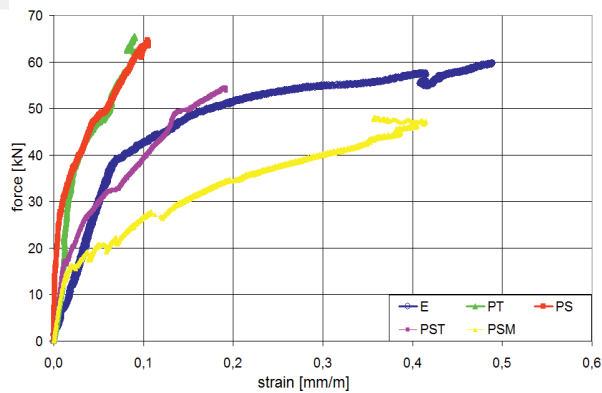


Fig. 13. Comparison of strain changing measured on strain gauge g1

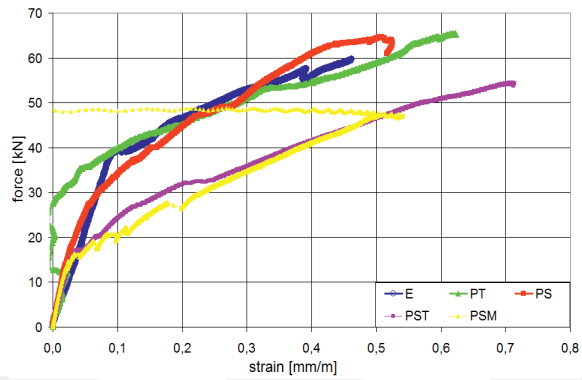


Fig. 14. Comparison of strain changing measured on strain gauge g2

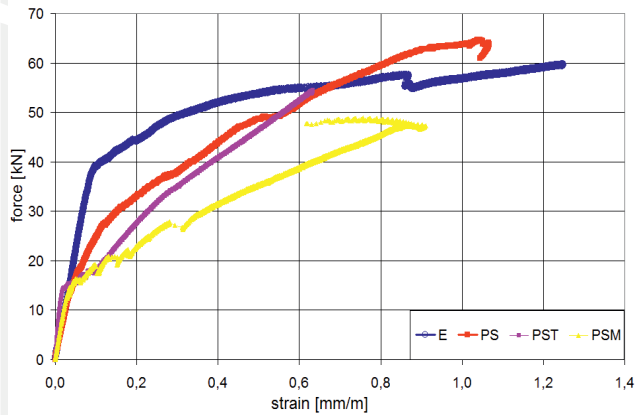


Fig. 15. Comparison of strain changing measured on strain gauge g3

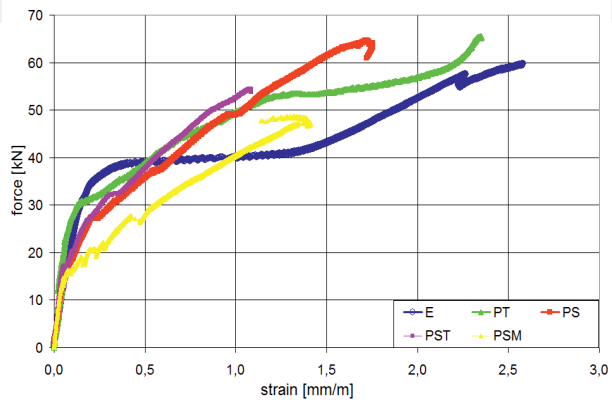


Fig. 16. Comparison of strain changing measured on strain gauge g4

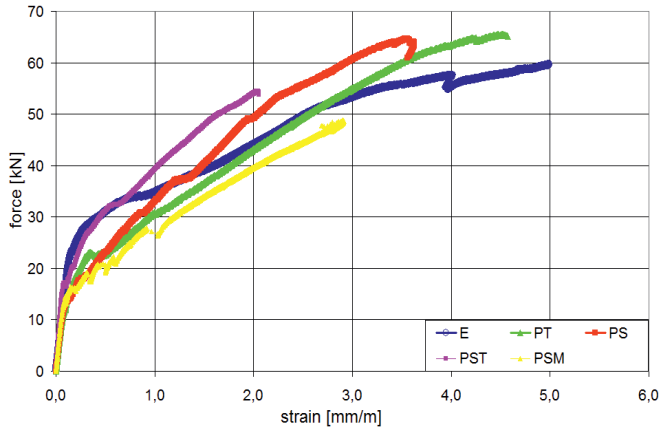


Fig. 17. Comparison of strain changing measured on strain gauge g5

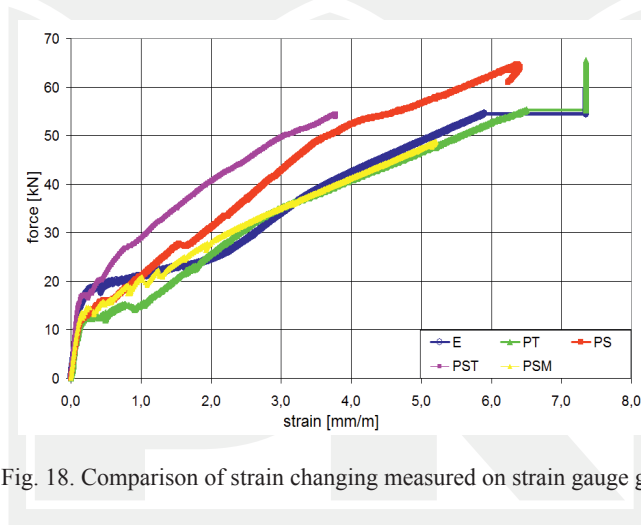


Fig. 18. Comparison of strain changing measured on strain gauge g6

#### 4.3. Deflection distribution

The deflections of the strengthened beams (measured at points d1, d2, d3 – Fig. 4) under load of 40 kN and under ultimate load for each tested beam are compared in Fig. 19, 20, respectively.

During the whole test, the measured vertical displacements of the beams strengthened by use of the middle flexible polymer adhesive (PS) were smaller than those of the remaining strengthened beams. Attention should be paid to the fact that at close values of failure loads for all the strengthened beams, the deflections of the PS, PST and PSM beams were clearly smaller than the deflections of the other strengthened beams, and were similar to the deflection of the RC non-strengthened beam under about twice smaller load.

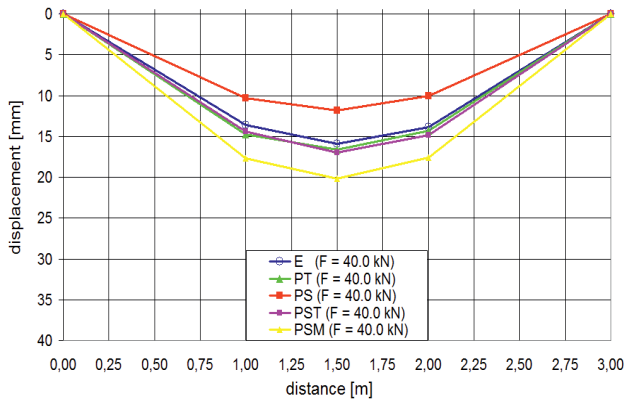


Fig. 19. Comparison of deflections of tested beams under load of 40 kN

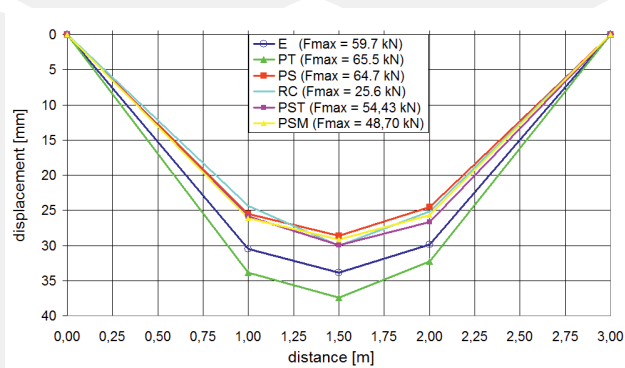


Fig. 20. Comparison of deflections of tested beams under ultimate load

## 5. Analysis of obtained results

### 5.1. Focus on stress concentration generated by a crack

Directly in the place of crack appearance (Fig. 21) a new state of tension stress  $\sigma_{\text{CFRP}}$  in a CFRP laminate (strip) is generated, caused by a shear component  $\tau$  and a debonding component  $\sigma_n$ . The value of tension stress can be calculated using equation (2).

$$\sigma_{\text{CFRP}} = \sqrt{\sigma_n^2 + \tau^2} \quad (2)$$

Additionally, the stress concentration phenomenon [3–4, 7] occurs in the debonded part of CFRP laminate, caused by the action of shear and normal stress concentrations, directly under the crack space (Fig. 21). Thus in reference to equation (2), the tension stress level is much higher than in the laminate joined to a concrete substrate.

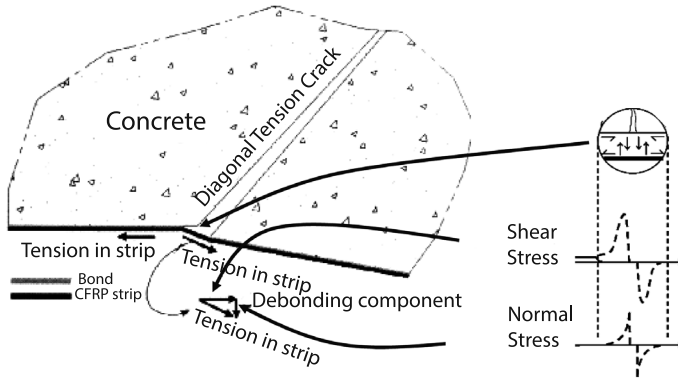


Fig. 21. Shear and normal stress concentration in a CFRP laminate under crack

## 5.2. Redistribution of stress after crack appearance

Moreover, the high level of tensile stress in CFRP laminate derives from the redistribution of tensile stress in a working cross-section after crack appearance. Tensile forces  $F$ , calculated according to equation (3), are always in the state of balance before and after crack appearance, which is illustrated in Fig. 22. Before crack appearance (Fig. 22a), the resultant tensile force  $F_t$  in the tension zone is balanced by a sum of force components acting in structural materials: concrete  $F_C$ , epoxy adhesive  $F_A^{\text{epoxy}}$  and CFRP laminate  $F_{\text{CFRP}}$  – equation (4).

$$F = E \cdot \varepsilon \cdot A = \sigma \cdot A \quad (3)$$

$$F_t = \begin{cases} F_C + F_A^{\text{epoxy}} + F_{\text{CFRP}} \\ F_{\text{CFRP}} \\ F_A^{\text{polymer}} + F_{\text{CFRP}} \end{cases} \quad (4)$$

where:

$E$  – Young's modulus,

$e$  – strain,

$A$  – working cross-section of material under tension.

After crack appearance in the structure with stiff epoxy adhesive (Fig. 22b), the resultant tensile force  $F_t$  in the tension zone is balanced only by CFRP laminate  $F_{\text{CFRP}}$  – equation (4), because stiff adhesive cracks in a brittle way almost at the same time as concrete, thus  $F_{\text{CFRP}}$  has to be higher. On the other hand, if a flexible polymer adhesive is applied (Fig. 22c), the resultant tensile force  $F_t$  in the tension zone is balanced by a sum of force in polymer adhesive  $F_A^{\text{polymer}}$  and in CFRP laminate  $F_{\text{CFRP}}$  – equation (4). Tensile force in polymer  $F_A^{\text{polymer}}$  still appears after cracking because a flexible adhesive layer reduces stress concentrations [3, 4] and protects CFRP laminate against the notch effect during debonding (Fig. 3, 21).

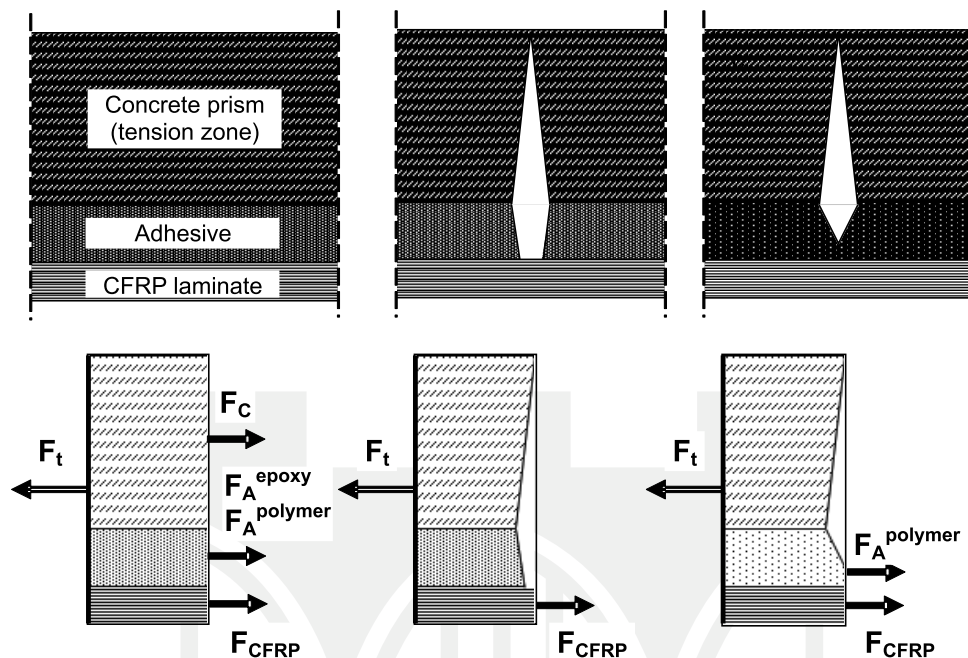


Fig. 22. Comparison of the tensile force balance in the tension zones for strengthened structures: a) before crack appearance (epoxy adhesive), b) after crack appearance (epoxy adhesive) and c) after crack appearance (polymer adhesive)

### 5.3. Deflection reduction in the case of flexible polymer adhesive application

The observed reduction of beams deflection (Fig. 19, 20) in the case of flexible polymer adhesive (PS) application, is caused by protection against an increase of tensile stress  $\sigma_{CFRP}$  in CFRP laminate in the place of cracking. Because CFRP deformation  $\Delta l$  is proportional to tensile stress  $\sigma_{CFRP}$ , the lower stress in the CFRP laminate is the lower is the CFRP deformation and thus lower deflection of strengthened beams.

In the case of stiff adhesive, many wide cracks with high stress concentration appear, thus the sum of the CFRP local deformations  $\Delta l$  is higher than in the case of the flexible adhesive. On the other hand, the slips of CFRP ends are higher in the case of the flexible adhesive than in the case of stiff one. Comparing deflections for the same load (Fig. 19) of CFRP bonded on adhesives E and PS, it can be found that the E deflection is almost 1.5 higher than the PS deflection. Because the total elongation of the beam bottom is the sum of the local deformations ( $\Sigma \Delta l$ ) and the sum of the slips ( $s$ ) on both ends, and it is proportional to the deflection, the total elongation of CFRP bonded on a flexible adhesive is lower than the total elongation of CFRP bonded on a stiff adhesive.

## 6. Conclusions

It is commonly expected, taking a more flexible adhesive into consideration, that a higher slip of CFRP laminate should cause a higher value of beam deflection. Unexpectedly, the deflection of the PS beam (in the whole measured range) was clearly smaller than the deflections of other strengthened beams and the ultimate deflections of PS, PST, PSM beams were similar to the deflection of the RC non-strengthened beam under about twice smaller load. It was an effect of protection against an increase of tensile stress  $\sigma$  in CFRP laminate in the place of cracking. In the case of a stiff adhesive, many wide cracks with high stress concentration appear, thus the sum of the CFRP local deformations is higher than in the case of a flexible adhesive. Moreover, in the case of a flexible adhesive, cracks do not go through ductile polymer but are stopped in it and stress redistribution occurring in the adhesive layer allows for even distribution of load to the CFRP laminate.

The new approach to strengthening of RC beams with CFRP laminates using polymer flexible adhesives is innovative and opens a new branch in research analysis. It is obvious that a lot of tests on such adhesives have to be carried out to also check durability and rheological properties of the proposed system. The obtained results raise the authors' hopes that solutions with application of polymer flexible adhesives will enable an increase in the efficiency of FRP in strengthening methods in the near future.

## References

- [1] Derkowski W., Kwiecień A., Zając B., *Comparison of CFRP strengthening efficiency of bent RC elements using stiff and flexible adhesives*, 3rd International fib Congress and PCI Convention, Washington D.C., USA, June 2010.
- [2] Cognard P., *Technical Characteristics and Testing Methods for Adhesives and Sealants*, Adhesives and Sealants Basic Concepts and High Tech Bonding, V. 1, Elsevier, 2005.
- [3] Kwiecień A., *Polymer flexible joints – an innovative repair system protecting cracked masonries against stress concentrations*, Proceedings of Protection of Historical Buildings, PROHITECH 09, V.2, 2009.
- [4] Fitton M.D., Broughton J.G., *Variable modulus adhesives: an approach to optimized joint performance*, International Journal of Adhesion & Adhesives 25, 2005.
- [5] Shrive N.G., Reda Taha M.M., Masia M.J., *Restoration and strengthening with fiber reinforced polymers: issues to consider*, Proceedings of 4th International Seminar on Structural Analysis of Historical Constructions., V. 2, 2004.
- [6] Kwiecień A., *Bonding of CFRP composites to structure using flexible polymer joint* (in Polish), Zeszyty Naukowe Politechniki Łódzkiej, Budownictwo, Nr 55, 993, 2006.
- [7] Buyukozturk O., Gunes O., Karaca E., *Progress on understanding debonding problems in reinforced concrete and steel members strengthened using FRP composites*, Construction and Building Materials 18, 2004.

KRZYSZTOF GROMYSZ\*

## DISSIPATIVE FORCES IN JOINT SURFACE OF COMPOSITE REINFORCED CONCRETE FLOORS

### SIŁY ROZPRASZAJĄCE ENERGIĘ W ZESPOLENIU ŻELBETOWYCH STROPÓW WARSTWOWYCH

#### Abstract

It is assumed that longitudinal shearing in joint surface (interface) of composite floors is balanced by: elastic forces, force of cohesion and kinetic friction. Moreover, internal friction occurs in the interface. Due to their nature, not all the above mentioned phenomena occur at the same time; however they are together responsible for deformation of interface. The paper discusses dissipative forces (non elastic). An interface model is built and test results of six floors are presented. All slabs are the same size – 3 m span and 0.6 m width and 0.18 m high. All slabs have the same longitudinal reinforcement. There are four types of join surface tested: smooth, very smooth, with eliminated adhesion and indented.

*Keywords: Composite floor, concrete structures, dissipative forces*

#### Streszczenie

Przyjęto, że siły podłużnego ścinania w płaszczyźnie zespolenia żelbetowych stropów warstwowych są równoważone przez: siły sprężyste, kohezję oraz tarcie kinetyczne. Ponadto w zespoleniu pojawia się tarcie wewnętrzne. Ze względu na swoją naturę nie wszystkie siły wywoływane są równocześnie, jednakże wspólnie odpowiadają za obserwowane odkształcenia w zespoleniu. W artykule zrelacjonowano badania sześciu płyt, które cechowały się takimi samymi wymiarami – rozpiętość 3 m, szerokość 0,6 m, wysokość 0,18 m i taką samą ilością zbrojenia przęsłowego. W płytach zastosowano cztery rodzaje powierzchni zespolenia: gładką, bardzo gładką, z usuniętą przyczepnością oraz z wrębami.

*Słowa kluczowe: stropy zespolone, konstrukcje żelbetowe, siły rozpraszające energię*

\* Phd. Eng. Krzysztof Gromysz, Department of Building Structures, Silesian Technical University.

## 1. Introduction

Steel reinforced composite floors consist of two layers of concrete: the bottom one being a prefabricated slab and a top one which is cast in situ. The surface of the prefabricated element is usually rough or indented. Transverse reinforcement protrudes from the prefabricated slab (Fig. 1). The prefabricated slab serves as a form-work for cast in situ concrete.

Capacity of one-way steel reinforced concrete composite floor depends on several factors [1]: capacity of main reinforcement anchored in support, bending capacity but mainly the capacity of the shear stress in joint surface (interface) [2].

Longitudinal shear in the interface of two concretes in element of width  $b$ , according to [3] is equal to:

$$q_{sj} = \frac{V}{z}, \quad (1)$$

where:

$V$  – transverse shear force and  $z$  is the lever arm of the composite section.

The model of interface between concretes is the contact layer (Fig. 2). In this layer, shear stress causes elastic and plastic strains. Thus, the longitudinal shear in the interface  $q_{sj}$  in the assumed model is balanced by elastic force (conservative force) and non-elastic (non-conservative force). Occurrence of elastic force  $q_{el}$  is caused by non-dilatational elastic strain of the contact layer and elastic strain of transverse reinforcement. The value of restoring forces is the arithmetic product of displacement of top and bottom layers of concrete ( $w$ ) and stiffness of the contact layer ( $k_{q,w}$ ) [4]. The value of  $k_{q,w}$  varies in the broad brackets from 1 GPa to 140 GPa and was the subject of the research presented in [5–6].

Occurrence of dissipative forces, which are the subject of research presented in the paper, depends on initial cohesion ( $q_{coh}$ ) and kinetic friction ( $q_{fr-int}$ ) that appears in the interference between top layer and bottom layer. In the interference, internal friction also occurs, which in the model discussed below does not transmit loading, but is responsible for maintaining plastic strain. Due to its nature, not all the above mentioned phenomena occur at the same time; however they are together responsible for contact layer strain. The analysis leads to the obvious conclusion that longitudinal shear in interface causes elastic and plastic strain. The two types of strain always occur at the same time and are caused by two corresponding forces: elastic force and dissipative force.

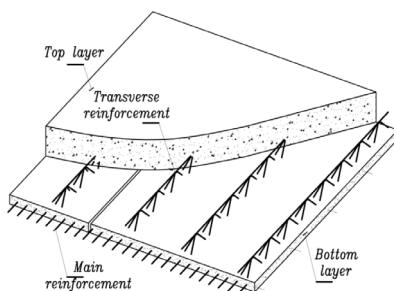


Fig. 1. Unidirectional reinforced concrete composite floor

The paper analyses work of dissipative forces occurring in the contact layer and compares it to energy accumulated in the layer. Analysis of dissipative forces occurring in the interface of composite floors wasn't done before. In the former author's paper just capacity of selected slabs and interface stiffness were investigated.

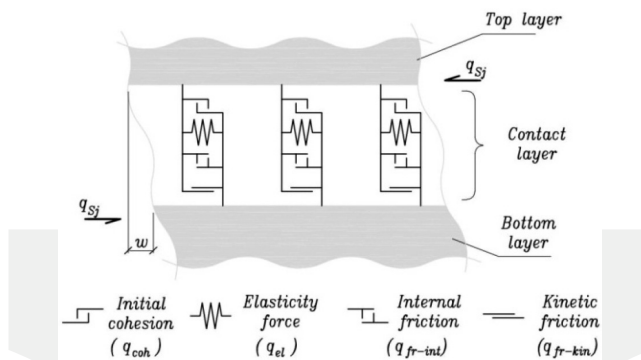


Fig. 2. Contact layer as a model of interface between top layer and bottom layer. Forces  $q_{coh}$ ,  $q_{el}$ ,  $q_{fr-int}$ ,  $q_{fr-kin}$  are balancing longitudinal shearing  $q_{sj}$

## 2. Research of interface in composite floors

The research concerns six simply supported slabs, each of 3300 mm length, 590 mm width, 180 mm height and 3000 mm span. Five slabs: P1, P3, P4, P5, P6 were composite slabs, while one – P2 was a monolithic slab.

The bottom reinforcement of each slab consisted of six ribbed rebars of 20 mm diameter; their axis was 30 mm apart from the bottom surface of the slabs. In the case of five slabs P1, P2, P3, P4, P6 transverse reinforcement in form of two trusses made of plain bars of 6 mm diameter welded to main rebars were used (rebar number 2 shown in Fig. 3).

In the case of composite slabs, four types of joint surface were employed (Fig. 4):

- smooth – a free surface left without further treatment after vibration (P1, P6),
- very smooth – a surface cast against a plywood panel formwork (P3),
- with eliminated adhesion (P4),
- indented with indentations 5/5 mm every 50 mm, cast against a plywood panel formwork (P5).

In the case of composite slabs, the bottom layer was made first, the top layer was cast three weeks later. The very smooth surface and the indented surface were obtained by pouring the concrete into a positioned formwork in an upside-down orientation with the interface down. The bottom of the formwork was made of smooth plywood in the case of slabs P3 and P4, while in the case of slab P5, 5/5 mm battens were screwed every 50 mm to the plywood which gave indentations in the cast. The bottom layer of slabs P1 and P6 was prepared in traditional way – a free surface left without further treatment after vibration. On the top of the surface, cement wash appeared.

The width of the interface was equal to the slab's width or, as in the case of slab P6, was reduced to 200 mm. Description of slabs, their types and surface types is shown in Fig. 4.

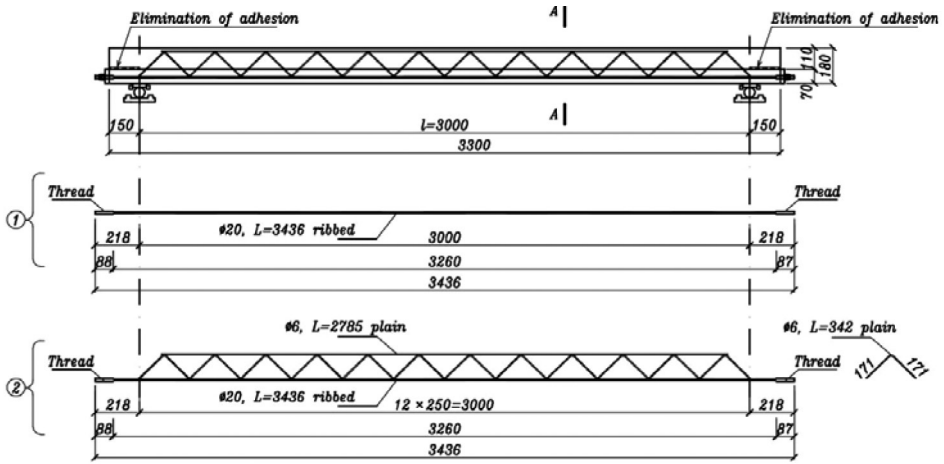


Fig. 3. Reinforcement of examined slabs. A-A sections of slabs are shown in Fig. 4

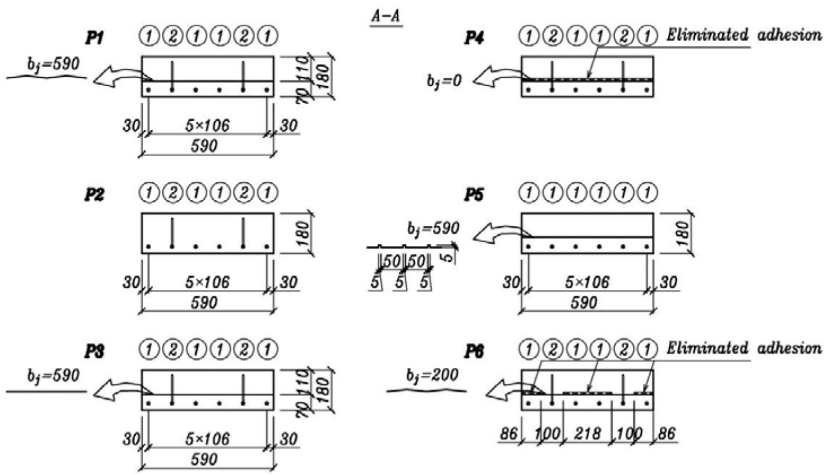


Fig. 4. Cross-sections of tested slabs,  $b_j$  – width of interface

Elimination of adhesion of two layers of concrete was ensured by two layers of oil covered foil. Moreover, in the case of all the slabs, adhesion was eliminated along the 150 mm parts of the joint surface beyond the axis of support. The following values were measured during the research:

- external loading force –  $Q$  (Fig. 5a),
- deflection in the centre of span –  $a$  (Fig. 5a),
- mutual displacement of bottom and top layers of concrete  $w_{7p}, w_{6p}, w_{5p}, w_{4p}, w_{3p}, w_{2p}, w_1, w_{2p}, w_{3p}, w_{4p}, w_{5p}, w_{6p}, w_{7l}$  (Fig. 5b, c),

Indices in denotation of layer displacement measurements include designation of symmetrically loaded slab side – “ $r$ ” denotes right side while “ $l$ ” denotes left side. Deflections and displacements were recorded with the use of a recording system, ensuring 0.001 mm

resolution. The testing system was ensuring applying the  $Q$  force of resolution 0,01 kN. The level of resolution was the effect of analog-digital converter limitation and not inaccuracy of inductive sensors. The range of the measuring device was 20 mm.

All the slabs, apart from the two cases discussed below, were loaded in the centre of the span with concentrated force  $Q$ . Loading was increased from zero to a predetermined value, then the slab was unloaded. For each slab four predetermined levels of load force were used – these were denoted as  $Q_A$ ,  $Q_B$ ,  $Q_C$  and  $Q_D$ . Level  $Q_A$  corresponds to approximately 0.1 mm deflection in the midspan, level  $Q_B$  – 0.5 mm deflection, while level  $Q_C$  – 50% of tested load capacity of the slab. All slabs loaded with force  $Q_D$  (force  $Q_D$  is the tested load capacity) showed large deformation. The slabs were tested one month after the top layer of concrete was produced. The shrinkage of the top layer of concrete effected the stress state of the contact layer but, due to short time of slab's loading, didn't effect the measurement results.

In the case of slabs P1 and P2, force was applied differently – force  $Q$  was divided into two forces (four-point bending), which is presented in Fig. 5a.

The above presented program of research is a part of broader research, including an evaluation of the hysteresis loop for the first three forms of free vibrations, modal studies and studies of free vibrations for different states of slabs. Results of this research will be presented in other publications.

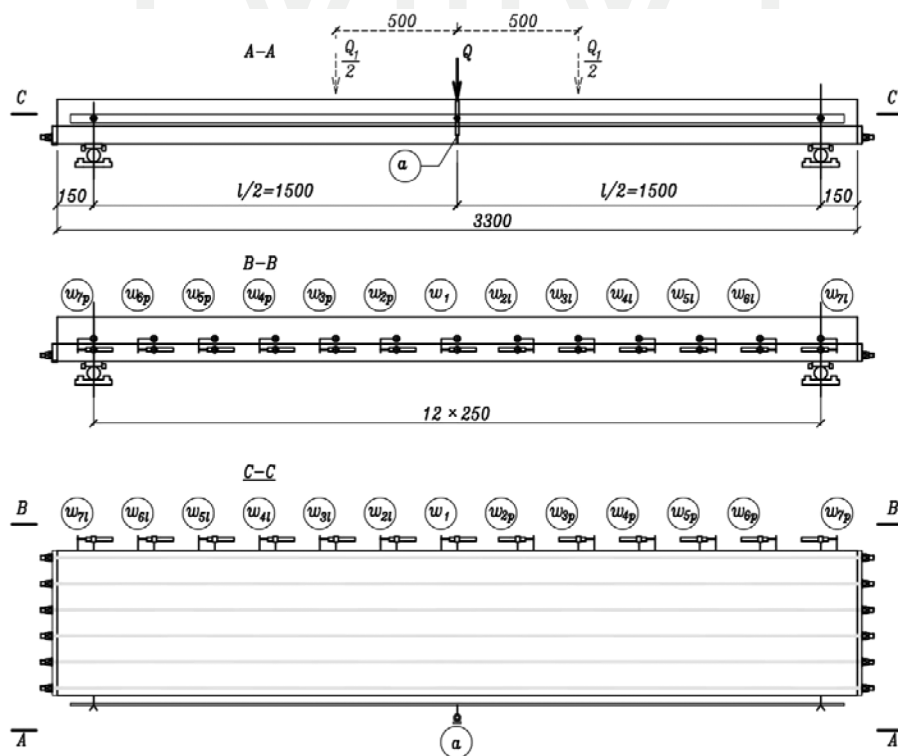


Fig. 5. Test setup for composite slab test

### 3. Test results

The research provided extensive investigational material. The paper is restricted to presenting those findings, which allow to describe non-conservative forces in joint surface. Fig. 6, 8 show measured values of displacement  $w_{ip}$  in function of loading, i.e. in correlation  $w_{ip}(Q)$  for all composite slabs. Measurements for three loading-unloading cycles, corresponding to forces  $Q_A$ ,  $Q_B$  and  $Q_C$  for slabs P4 and P6 are shown in Fig. 6 and Fig. 7. Results for slabs P1, P3 and P5 include values for cycles at loading force  $Q_C$ , only (Fig. 8). Resolution of the recording system did not allow for the recording of results corresponding to forces  $Q_A$  and  $Q_B$ .

Analysis of correlations  $w_{ip}(Q)$  (Fig. 6, 8) allow for stating that all the slabs are characterised by a hysteresis loop, that is, the curve of loading does not overlap the curve of unloading and that permanent displacement in joint surface ( $w_r$  – Fig. 9) is observed after unloading. Moreover, it can be noticed, that in the case of all measurements the sensors closest to the place, where loading force was applied, that is  $w_{2p}$  and  $w_{3p}$ , recorded displacement practically from the beginning of loading. In the range of loading forces  $Q_A$  and  $Q_B$  in slabs P4 and P6 as well as in the range of loading force  $Q_C$  in slab P3, all the curves  $w_{ip}(Q)$  in the part where loading force  $Q$  was increasing were almost straight. This observation was the basis for an assumption that the proportion of elastic and plastic strain is constant in the so called elastic phase of work in the interface.

Due to their shape, the hysteresis loops may be divided into two groups.

The first group includes curves presented in Fig. 6a, b, 7a, b, 8b, c in which the loading-unloading process proceed along approximately parallel straight curves. The hysteresis loop is a result of phase of unloading, when decrease in loading force  $Q$  does not cause a change in displacement of top and bottom ( $w$ ) layers (also Fig. 9a).

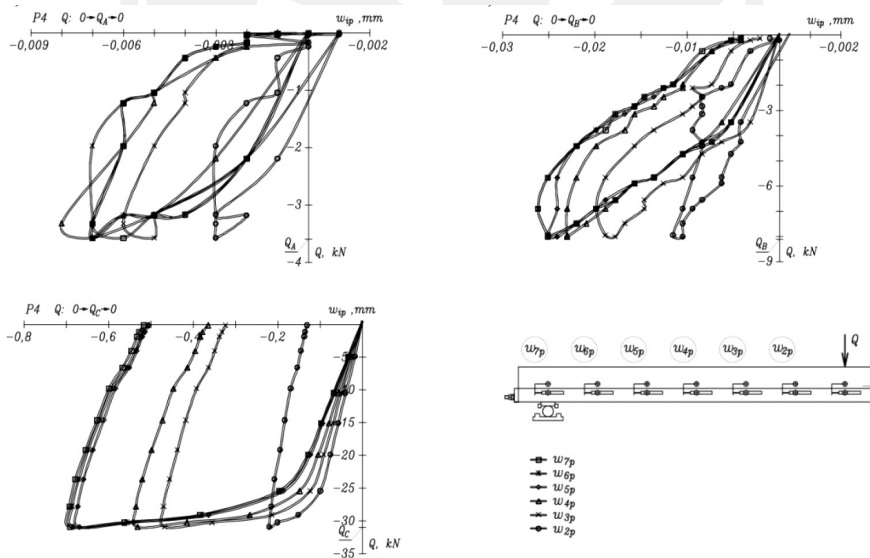


Fig. 6. Values of displacement in joint surface of slab P4 recorded in loading-unloading cycle corresponding to forces: a)  $Q_A$ , b)  $Q_B$ , c)  $Q_C$

The second group includes curves presented in Fig. 6c, 7c, 8a. In this group, the process of loading consists of two segments: first one, in which curve( $Q$ ) corresponding to the loading process, is inclined at an acute angle in relation to the horizontal axis (also Fig. 9b – inclination  $k_{w,fr-int}$ ), and the second one in which this curve is inclined at an obtuse angle to the horizontal axis (also Fig. 9b – inclination  $k_{w,fr-kin}$ ). Curve segment  $w(Q)$ , corresponding to unloading, is parallel to the first curve segment of the loading process.

The type of joint surface does not determine whether curve  $w_i(Q)$  belongs to the first or second group. For instance, for slab P6, curves shown in Fig. 7a, b belong to the first group while curves shown in Fig. 7c belong to the second group. The curves suggest that it is the value of displacement of two layers of concrete, corresponding to the maximum loading force  $Q$ , that decides whether it belongs to this or another group. If the maximum displacement is smaller than approximately 0.1 mm then the curve belongs to the group presented in Fig. 9a; if it is greater than approx. 0.1 mm, then the curve belongs to the group presented in Fig. 9b.

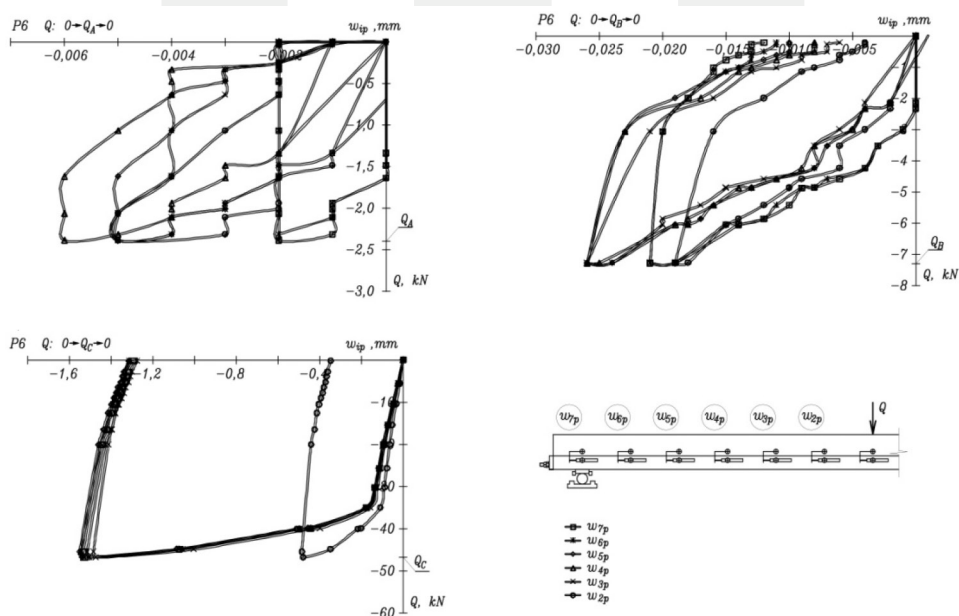
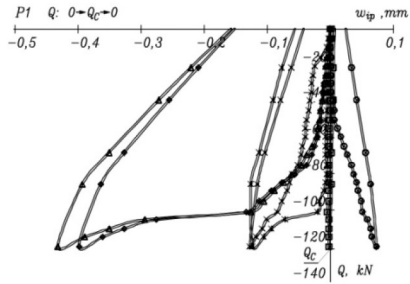


Fig 7. Diagrams of displacement in joint surface of slab P6 for loading-unloading cycles corresponding to forces: a)  $Q_A$ , b)  $Q_B$ , c)  $Q_C$

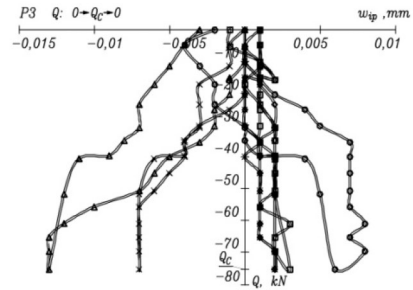
In the case of slabs P1, P4 and P6, delamination occurred as an effect of loading. Slabs P2, P3 and P5 were no longer loaded, as significant deflection occurred after loading with  $Q_D$  (yield of main reinforcement).

Slabs were statically loaded with forces  $Q_A$ ,  $Q_B$ ,  $Q_C$  generating corresponding deflections  $a_A$ ,  $a_B$ ,  $a_C$  whose values are presented in Table 1. After generating deflection, the slabs were statically unloaded. In the course of loading – unloading, cycle measurements were made of loading force, deflection and displacement according to Fig. 5. In the final stage of experiment, the slabs were loaded with load  $Q_D$ , which caused considerable deformation of slabs (slabs deflection was about 30 mm) that exceed the range of the measuring device.

a)



b)



c)

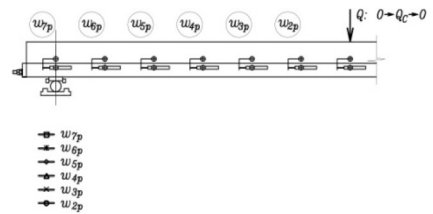
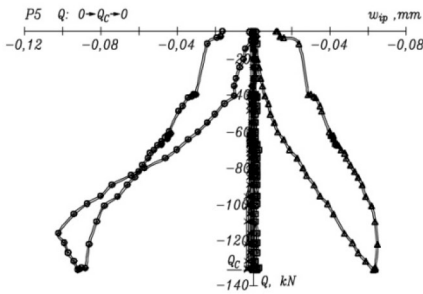


Fig. 8. Diagrams of displacement in joint surface recorded in loading-unloading cycle corresponding to  $Q_C$  force a) slab P1, b) slab P3, c) slab P5

Table 1

Maximum values of load forces ( $Q$ ) and deflection in the centre of span ( $a$ ) in cycles of loading

Element	$Q_A$ [kN]	$a_A$ [mm]	$Q_B$ [kN]	$a_B$ [mm]	$Q_C$ [kN]	$a_C$ [mm]	$Q_D^*$ [kN]
P1	5.46	0.083	6.10	0.381	120.41	11.988	165
P2	3.56	0.107	11.30	0.493	139.97	13.434	265
P3	4.54	0.113	–	–	75.27	7.625	260
P4	3.58	0.122	8.03	0.536	31.01	9.618	45
P5	2.69	0.110	9.94	0.540	131.29	17.808	270
P6	2.39	0.126	7.30	0.542	46.95	17.411	74

\* Deflection corresponding to load  $Q_D$  exceed the range of the measuring device equal to 20 mm

#### 4. Test results interpretation

As shown above in the obtained curves of correlation, loading force ( $Q$ ) displacement in joint surface ( $w$ ) in the cycle of loading and unloading may be related to one of the two loops of hysteresis presented in Fig. 9. Appearance of this loop indicates that elastic strain is accompanied by plastic strain. The area of the loop is the measure of work performed by dissipative forces.

In agreement with the model (Fig. 2), it was assumed that in the case of the loop presented in Fig. 9a, the work was performed by internal friction force, while in the case of the loop presented in Fig. 9b, the work was performed by force of kinetic friction. Alteration of gradient of  $Q(w)$  curve (Fig. 9b) in the course of loading indicates kinetic displacement of the bottom layer in relation to the top layer.

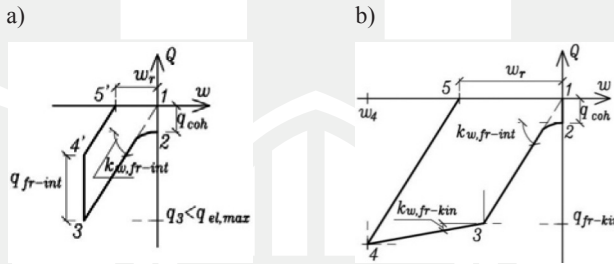


Fig. 9. Hysteresis loop of interface of composite floors: a) loop in the case when displacement  $w < 0.1$  mm is caused by forces of internal friction ( $q_{fr-int}$ ), b) loop in the case when displacement  $w > 0.1$  mm is caused by forces of kinetic friction ( $q_{fr-kin}$ )

##### 4.1. Energy dissipated by internal friction

When values ( $w_p, Q_i$ ) are known, the area of the hysteresis loop denoted as  $\Psi_w$  can be calculated from the formula:

$$\Psi_w = \frac{1}{2} \sum_{i=1}^n Q_i (w_{i+1} - w_{i-1}) \quad (2)$$

This area is marked with horizontal lines on Fig. 10

The area in Fig. 10, which is marked with vertical lines, is the measure of potential energy accumulated in the joint surface at the moment when the slab was loaded with maximum loading. This area was denoted as  $E_{p,w}$  and can be calculated from formula (2).

Table 2 shows individual loading – unloading cycles in which the value of displacement ( $w$ ) did not exceed approximately 0.1 mm, determined measures  $\Psi_w$  and  $E_{p,w}$  as well as coefficient of energy dissipation defined as:

$$\chi = \frac{\Psi_w}{E_{p,w}} \quad (3)$$

The results presented in this table show that in the case of slabs P1, P4 and P5, the value of the coefficient of energy dissipation  $\chi_{\text{stat}}$  increases with distance from the point where loading force was applied. For instance, in slab P1 for cycle corresponding  $Q_C$  force, this value increases from 0.259 for measurement  $w_{2p}$  to 0.863 for measurement  $w_{7p}$ . In slab P4 for cycle corresponding to force  $Q_A$ , value  $\chi_{\text{stat}}$  increases from 0.599 for measurement  $w_2$  to 0.765 for measurement  $w_6$ , while in slab P6, the cycle corresponding to force  $Q_A$  increases from 0.315 (measurement  $w_2$ ) to 0.923 (measurement  $w_7$ ). The results also show that the increase of parameter  $\chi$  is greater in the case of slabs P1 and P6, where concrete in contact layer also takes part in energy dissipation. In the slab P4, where the possibility of the generation of static friction stress on the surface of two layers of concrete was eliminated, energy is dissipated mainly by work performed by the surface of transverse reinforcement in the concrete canal.

Slabs P3 and P5, which show considerable value of elasticity coefficient and in which case no delamination occurred during destruction, are characterized by a lesser coefficient of energy dissipation. In these slabs, no increase of coefficient  $\chi_{\text{stat}}$  value was observed with increase of distance from point of force application.

The obtained results allow for the assumption that along with decrease of amplitude of loading force  $Q$ , the value of coefficient  $\chi$  increases at segments of slab which are further from point of force application. At sufficiently small amplitudes of exciting force and thus small deformation of slabs, segments of slabs close to support work as monolithic slabs, while in the area where force  $Q$  is applied, the slabs work as composite slab.

Table 2

**Results of analysis of elastic and non-elastic forces in elastic phase of work of joint surface**

P1, $Q_C$		$w_{2p}$	$w_{3p}$	$w_{4p}$	$w_{5p}$	$w_{6p}$	$w_{7p}$
$Q \in (0 \rightarrow Q_A \rightarrow 0 \text{ kN})$ $a \in (0 \rightarrow a_A \rightarrow 0 \text{ mm})$ $\chi_{\text{mead}} = 0,592$	$w_{i,\text{max}}$ [mm]	+0.073	-0.127	-0.430*	-0.362*	-0.127	-0.002
	$\Psi_w$ [N·m]	1.873	66.060	53.863	46.044	34.176	8.437
	$E_{p,w}$ [N·m]	7.245	101.01	98.73	83.39	50.48	9.777
	$\chi$	0.259	0.654	0.546	0.552	0.677	0.863
P3, $Q_C$		$w_{2p}$	$w_{3p}$	$w_{4p}$	$w_{5p}$	$w_{6p}$	$w_{7p}$
$Q \in (0 \rightarrow Q_C \rightarrow 0 \text{ kN})$ $a \in (0 \rightarrow a_C \rightarrow 0 \text{ mm})$ $\chi_{\text{mead}} = 0,481$	$w_{i,\text{max}}$ [mm]	+0.008	+0.007	-0.013	+0.002	+0.002	+0.003
	$\Psi_w$ [N·m]	0.261	0.067	0.268	0.077	0.070	0.027
	$E_{p,w}$ [N·m]	-	0.257	0.573	0.098	0.105	0.124
	$\chi$	-	0.259	0.467	0.790	0.671	0.216

P1, $Q_C$		$w'_{2p}$	$w'_{3p}$	$w'_{4p}$	$w'_{5p}$	$w'_{6p}$	$w'_{7p}$
P4, $Q_A$		$w_{2p}$	$w_{3p}$	$w_{4p}$	$w_{5p}$	$w_{6p}$	$w_{7p}$
$Q \in (0 \rightarrow Q_A \rightarrow 0 \text{ kN})$ $a \in (0 \rightarrow a_A \rightarrow 0 \text{ mm})$ $\chi_{\text{mead}} = 0,654$	$w_{i,\text{max}}$ [mm]	-0.003	-0.006	-0.008	-0.007	-0.007	-0.007
	$\Psi_w$ [N·m]	0.0047	0.0092	0.0099	0.0118	0.0132	0.0124
	$E_{p,w}$ [N·m]	0.0078	0.0148	0.0186	0.0170	0.0173	0.0175
	$\chi$	0.599	0.620	0.530	0.698	0.765	0.709
P4, $Q_B$		$w_{2p}$	$w_{3p}$	$w_{4p}$	$w_{5p}$	$w_{6p}$	$w_{7p}$
$Q \in (0 \rightarrow Q_B \rightarrow 0 \text{ kN})$ $a \in (0 \rightarrow Q_B \rightarrow 0 \text{ mm})$ $\chi_{\text{mead}} = 0,527$	$w_{i,\text{max}}$ [mm]	-0.011	-0.019	-0.022	-0.025	-0.025	-0.025
	$\Psi_w$ [N·m]	0.0241	0.0465	0.0524	0.064	0.0696	0.0699
	$E_{p,w}$ [N·m]	0.0529	0.0907	0.104	0.120	0.121	0.121
	$\chi$	0.454	0.512	0.505	0.536	0.575	0.577
P5, $Q_C$		$w_{2p}$	$w_{3p}$	$w_{4p}$	$w_{5p}$	$w_{6p}$	$w_{7p}$
$Q \in (0 \rightarrow Q_C \rightarrow 0 \text{ kN})$ $a \in (0 \rightarrow a_c \rightarrow 0 \text{ mm})$ $\chi_{\text{mead}} = 0,494$	$w_{i,\text{max}}$ [mm]	-0.102	-0.003	+0.065	-0.001	-0.001	+0.003
	$\Psi_w$ [N·m]	-	0.131	2.849	-	-	0.050
	$E_{p,w}$ [N·m]	-	0.253	5.277	-	-	0.118
	$\chi$	-	0.517	0.539	-	-	0.426
P6, $Q_A$		$w_{2p}$	$w_{3p}$	$w_{4p}$	$w_{5p}$	$w_{6p}$	$w_{7p}$
$Q \in (0 \rightarrow Q_A \rightarrow 0 \text{ kN})$ $a \in (0 \rightarrow a_A \rightarrow 0 \text{ mm})$ $\chi_{\text{mead}} = 0,754$	$w_{i,\text{max}}$ [mm]	-0.005	-0.005	-0.006	-0.005	-0.002	-0.002
	$\Psi_w$ [N·m]	0.0048	0.00580	0.00565	0.00520	0.00402	0.00413
	$E_{p,w}$ [N·m]	0.0090	0.0090	0.0085	0.0076	0.0040	0.004
	$\chi$	0.531	0.645	0.667	0.686	0.999	0.994
P6, $Q_B$		$w_{2p}$	$w_{3p}$	$w_{4p}$	$w_{5p}$	$w_{6p}$	$w_{7p}$

P1, $Q_C$		$w'_{2p}$	$w'_{3p}$	$w'_{4p}$	$w'_{5p}$	$w'_{6p}$	$w'_{7p}$
$Q \in (0 \rightarrow Q_B \rightarrow 0 \text{ kN})$ $a \in (0 \rightarrow a_B \rightarrow 0 \text{ mm})$ $\chi_{\text{mead}} = 0,702$	$w'_{i,\text{max}}$ [mm]	-0.019	-0.026	-0.026	-0.026	-0.021	-0.021
	$\Psi_w$ [N·m]	0.0531	0.0672	0.0800	0.0862	0.0920	0.0954
	$E_{p,w}$ [N·m]	0.0880	0.117	0.121	0.124	0.111	0.113
	$\chi$	0.604	0.577	0.660	0.698	0.827	0.847

\* displacement in the range of 0.1 mm were exceeded

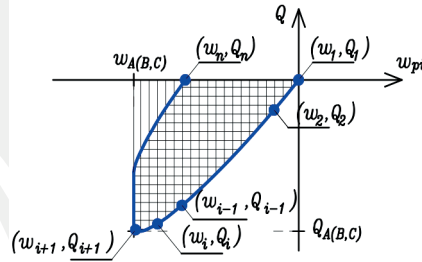


Fig. 10. Elastic potential energy  $E_{p,w}$  in joint surface (area marked with vertical lines) and energy dissipated  $\Psi_w$  at segment of joint surface (area marked with horizontal lines – the area of hysteresis loop)

#### 4.2. Energy dissipated by kinetic friction

When the possibility of load transfer by elastic forces is exhausted, which is interpreted in the model as a loss of continuity of strain ( $w > 0.1$  mm), forces of kinetic friction  $\tau_{fr-kin}$  are generated in the joint surface. The model assumes that these forces are distributed uniformly along the joint surface and that they do not depend on loading. Increase of loading force  $Q$  effects in considerable increase of displacement between top and bottom layers ( $w$ ).

In the course of discussed research kinematic friction, stress was generated in the joint surface of two slabs. In slab P4, it was generated under loading  $Q_{kin} = 25.05$  kN while in slab P6, it was generated under loading  $Q_{kin} = 35.20$  kN. Values  $q_{fr,kin}$  determined on equation (1), are equal correspondingly 98.24 kN/m and 138.04 kN/m.

It was also observed that relationship  $Q(w_i)$  is not a straight line. It means that stiffness of the contact layer is a non-linear parameter. Similar was observed in [1, 7, 8–9].

**Values of kinetic friction stress in joint surface in non-elastic phase of work of joint surface**

P4, $Q_C$	$w_{2p}$	$w_{3p}$	$w_{4p}$	$w_{5p}$	$w_{6p}$	$w_{7p}$
$w_{i,max}$ [mm]	-0.220	-0.467	-0.532	-0.676	-0.684	-0.91
$w_{i,kin}$ [mm]	-0.075	-0.091	-0.104	-0.123	-0.128	-0.128
$\Psi_w$ [N·m]	3.611	10.075	11.301	14.838	14.947	15.166
P6 $Q_C$	$w_{2p}$	$w_{3p}$	$w_{4p}$	$w_{5p}$	$w_{6p}$	$w_{7p}$
$w_{i,max}$ [mm]	-0.479	-1.483	-1.545	-1.545	-1.545	-1.533
$w_{i,kin}$ [mm]	-0.089	-0.123	-0.134	-0.136	-0.131	-0.136
$\Psi_w$ [N·m]	15.479	56.202	57.192	57.295	56.043	56.677

## 5. Conclusions

Performed experiments vindicate the model's assumption that shear in the interface of two concretes is balanced by elasticity forces and two kinds of non-elastic forces: initial cohesion and kinetic friction.

The outcome of the research indicates that in the interface between the top and bottom layers, internal friction appears. Internal friction appears when displacement between the top and bottom concrete layers is smaller than approximately 0.1 mm. This friction is responsible for generating the loop of hysteresis in the loading – unloading process, it means it is responsible for energy dissipation in the interface. The coefficient of the energy dissipation in the interface varies from 0.259 to 0.92. The value of the coefficient depends on the load value and the distance of considered cross-section from the place of applied concentrated load.

Kinetic friction appears in cases where mutual displacement of the bottom and top layers of concrete is larger than 0.1 mm. This friction takes part in balancing longitudinal shearing in the interface only when the stiffness of the contact layer is small. The value of kinetic friction varies in tested slabs of 0.59 m width, from 98.24 kN/m to 138.04 kN/m.

*This paper was sponsored by program POIG.01.01.02-10-106/09-00.*

## References

- [1] Halicka A., *A study of the stress – strain state in the interface and support zones of composite structures with shrinking and expansive concretes*, Wydawnictwo Politechniki Lubelskiej, Lublin 2007.
- [2] Gromysz K., *Combined floors. Normative calculations guidecurves and capacity of actual structures*, 5-th international conference AMCM Analytical Models and New Concepts in Concrete and Masonry Structures, Gliwice-Ustroń June 12–14, 2005.

- [3] Eurocode 2: Design of Concrete Structures – Part 1–1: General rules and rules for buildings. EN 1992-1-1:2004. European Committee for Standardization, Brussels, 2004.
- [4] Gromysz K., *Longitudinal Shearing Balancing in Joint Surface of Composite Concrete Slabs*. Inżynieria i Budownictwo, 2010.
- [5] Gromysz K., *Testing stiffness of contact layer in composite concrete slabs*, 56 Konferencja Naukowa Komitetu Inżynierii Lądowej i Wodnej PAN oraz Komitetu Nauki PZITB, Kielce–Krynica 19–24 września 2010.
- [6] Gromysz K., *Calculation of deflection of delaminated reinforced concrete composite floor based on assumed frictional – elastic model of joint surface*, AMCM' 2008 6th International Conference, June 9–11, Łódź.
- [7] Diazmati B., Pincheira J.A., *Shear Stiffness and Strength of Horizontal Construction Joints*. ACI Structural Journal, Vol. 101, No. 4, July–August 2004.
- [8] Gohnert M., *Proposed theory to determine the horizontal shear between composite precast and in situ concrete*. Cement and Concrete Composites, No. 22, 2000.
- [9] Momayez A., Ramezaniapour A.A., Rajaie H., Ehsani M.R., *Bi-Surface test for Evaluation Bond between Existing and New Concrete*, ACI Materials Journal, Vol. 101, No. 2, March–April 2004.



ELŻBIETA HABIERA, ARTEM CZKWIANIANC\*

REDISTRIBUTION OF FORCES BETWEEN  
REINFORCEMENT BARS AND PROFILES IN THE  
INTERMEDIATE SUPPORT ZONE IN THE DOUBLE SPAN,  
DOUBLE COMBINED BEAMS

REDYSTRYBUCJA SIŁ POMIĘDZY ZBROJENIEM  
PRĘTOWYM I KSZTAŁTOWYM W STREFIE PODPORY  
ŚRODKOWEJ W DWUPRZĘŚŁOWYCH BELKACH  
PODWÓJNIE ZESPOŁONYCH

Abstract

The aim of the study was to analyse the behaviour of the innovative precast beams, where the prestressed concrete and specially prepared steel profile were combined. This paper deals with the results of the tests and the analysis of redistribution of internal forces between reinforcement bars and steel profiles in the intermediate support zone in the proposed double span beams.

*Keywords: composite structures, prestressed concrete, redistribution, steel profile*

Streszczenie

Celem badań była analiza zachowania innowacyjnych belek prefabrykowanych, w których zespolono beton sprężony i specjalnie przygotowany profil stalowy. Artykuł przedstawia wyniki badań i analizę redystrybucji sił wewnętrznych pomiędzy prętami zbrojeniowymi, a profilem stalowym w strefie podpory środkowej w proponowanych dwuprzęsłowych belkach.

*Słowa kluczowe: elementy zespolone, beton sprężony, redystrybucja, profil stalowy*

\* PhD Student Elżbieta Habiera, Professor Artem Czkwianianc, Department of Concrete Structures, Faculty of Civil Engineering, Architecture and Environmental Engineering, Technical University of Lodz.

### 1. Introduction

The subjects of research were precast beams, where the prestressed concrete and specially prepared steel profile were combined. The presented specimen is an innovative solution, indirectly inspired by the concept of hybrid beams, produced by Preflex & Flexstress [1]. It was estimated that this kind of beams will be able to cooperate with monolithic slabs or precast slabs (e.g. hollow plates) with topping concrete. The study verified behaviour of elements in both situations. Additionally, it was predicted that these kind of beams could be applied in buildings with highly loaded binders or in road structures such as bridges etc.

### 2. Test specimens

#### 2.1. Assumptions

The experimental tests comprised of six double span specimens. Each of the beams consisted of two single span precast, prestressed elements with a length of 4.0 m. Those precast beams were made by Ergon Poland company. The beams were loaded with two concentrated forces in every span (Fig. 1).

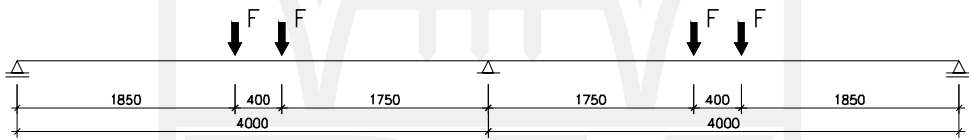


Fig. 1. Loading scheme

In the precast elements, a steel profile of a height of 290 mm height (Fig. 2) was used, composed of 1/2 H-section (top chord) and T-section (bottom chord). The top and bottom flange were connected with vertical double flat irons ( $6 \times 25$  mm), spaced equally at the beam length with 164 mm spacing. Double flat irons were welded on to the chords by fillet welds, with a thickness of 4mm and a length of 40 mm for the top chord and 44 mm for the bottom chord. The steel grade of the profile and the irons was 18G2 (steel grade due to Polish codes).

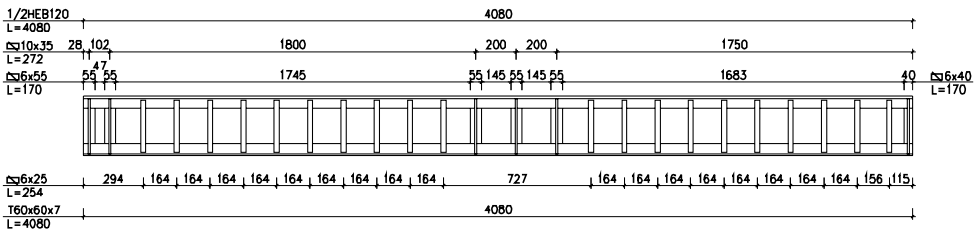


Fig. 2. The view of the steel profile used in tests

For the bottom longitudinal reinforcement, the prestressing strands were used. In Total, 8 strands Y1860 S7 with section  $A_p = 93 \text{ mm}^2$  were provided. Six of the strands were tensioned with a force of 138kN ( $\sigma_{pmo} = 1488 \text{ MPa}$ ) and the remaining two strands with a force of 20 kN ( $\sigma_{pmo} = 215 \text{ MPa}$ ).

As the upper reinforcement over the intermediate support the reinforcement bars were utilized. The steel had the characteristic yielding strength  $f_{yk} = 500 \text{ MPa}$ . Three different upper reinforcement ratios were assumed. For the beams denoted as 301 and 311, the reinforcement ratio was 0.013 (4#20), for beams 302 and 312 the reinforcement ratio was 0.020 (4#20+2#22) and finally for beams 303 and 313 it was 0.026 (5#22+2#20). It should be noticed that this assumption imposes a different redistribution of internal forces for each of the beams.

Sections of the particular beams are shown on Fig. 3. For each beam, there are also presented the values of ultimate forces and calculated capacities with the assumption of full redistribution of internal forces.

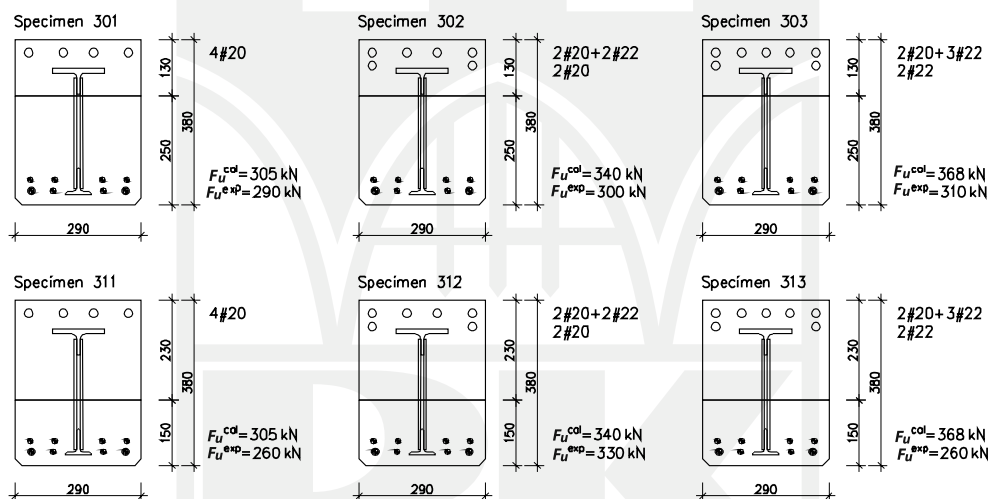


Fig. 3. Sections of the particular beam

As the reinforcement for shear there were used only exclusively flat irons with  $6 \times 25 \text{ mm}$  section that connected welded to the flanges of steel chords. profile. During the designing of this reinforcement, it was assumed that the inclination of the compressed strut (according to the truss model) satisfy a condition  $\cot \theta \approx 2$  [2].

In the strands anchoring zone, the horizontal loops were applied, together with additional vertical stirrups made from 8mm bars to prevent damage due to prestressing. Those stirrups were also designed under point loads to protect concrete from local crushing. Along the entire length of the beam, the horizontal joints were used to connect precast concrete and steel profile.

In the supports zones, the additional bars with threaded ends were designed to prevent the separation of the precast concrete and the topping concrete. Figure 4 shows the location of those bars for the extreme and the intermediate supports. The delamination force was transferred by the double iron flats of the steel profile together with those bars.

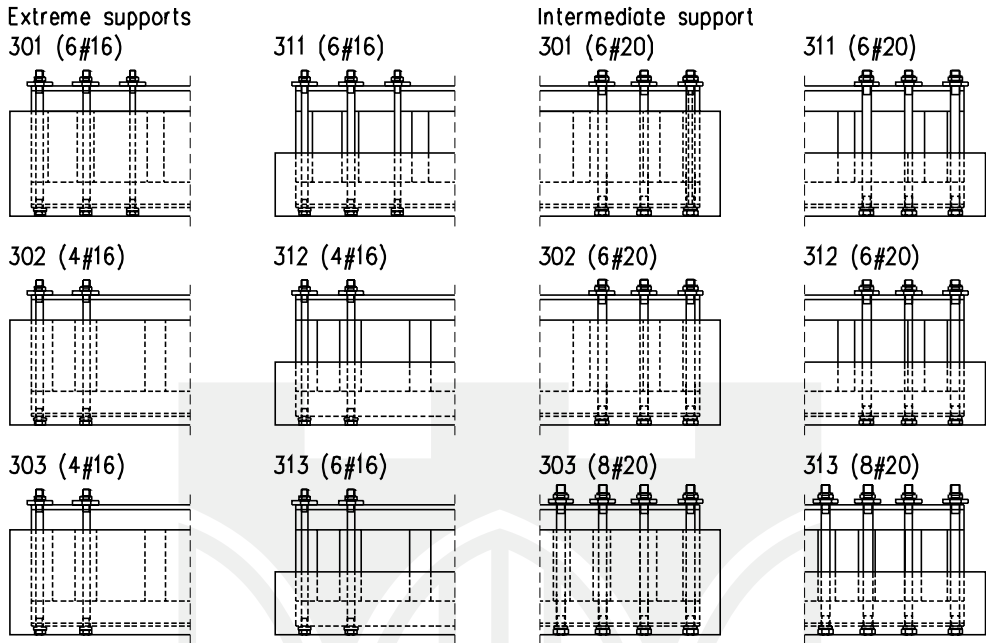


Fig. 4. Bars with threaded ends on the extreme and the intermediate supports

## 2.2. Materials

The elements were made in precast plant on the long production line with heat treatment. For all beams, the compressive strength of the precast concrete at the moment of the strands release was  $f_{c,cube} = 50.4$  MPa, while during the tests the compressive strength was  $f_c = 74.4$  MPa and  $f_{c,cube} = 84.5$  MPa. The topping concrete at the moment of the study reached the compressive strength equal  $f_c \approx 60$  MPa and  $f_{c,cube} \approx 70$  MPa.

The reinforcement steel had yielding strength equal  $f_y = 520$  MPa, while the profile steel had  $f_y = 434$  MPa for the 1/2 H-section and  $f_y = 289$  MPa for the T-section.

Full description of the element's reinforcement, the characteristics of the materials and properties of the composite cross-section are presented in [3].

## 2.3. Test preparations

The precast elements were imported from plant to the Laboratory of the Department of Concrete Structures of Technical University of Lodz, where they were prepared for the study. Two identical elements were arranged in a line on four leveled bases. The gap between elements with a 10mm thickness was filled with the epoxy. In the bottom zone of connection between two beams, the additional irons were mounted due to transportation and assembly on the testing stand. After the application of the strain gauges on the steel profile, the upper reinforcement was added and the topping concrete was provided. Fig. 5 shows activities performed during the preparation.



Fig. 5. Photos of the preparations of elements in the research laboratory

After approximately two weeks, the system was boarded and erected on the test stand (Fig. 6). The beam was placed on three supports. The intermediate support was set as the non-movable and to make good contact between support and the bottom of the beam the cement mortar pad was made. The extreme supports were movable. One support was leveled to the intermediate support, the other one was free to rotate around the axis of the beam.



Fig. 6. Photos of the test stand, extreme and intermediate supports

## 2.4. Measurements

The mechanical extensometers with base 200 mm and 400 mm, electric strain gauges and Linear Variable Differential Transformers (LVDT) were used to measure the strains of the concrete and steel.

After the concreting of the precast specimen, just before the prestressing strands release (on the surface of the concrete at the bottom part of the steel profile and on the top chord part of this profile) the special markers were applied to make the measurements bases. Reading measurements on these bases were performed before compression, immediately after compression and before performance the topping concrete. With these measurements, losses of prestressing force caused by elastic deformation of concrete and rheological losses in the period from compression to the tests were estimated.

Also after setting the final specimen on the test stand, just before studies, on the one side along the axis of the beam, the special markers were applied to measure the longitudinal strains –  $\epsilon_x$  (Fig. 7) and the vertical strains –  $\epsilon_y$ .

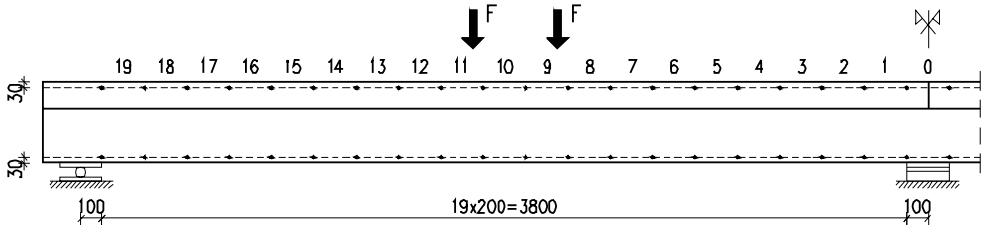


Fig. 7. Measurement bases – the mechanical extensometers with base 200 mm

In the tests, the load was applied by four hydraulic presses cylinders. The force was increased in fixed steps. After increasing and stabilizing of the force, the measurements were taken. The cracking development was observed together with crack width measurements. The total time of the one specimen test was about 5–6 hours.

### 3. Test results and analysis

In the intermediate support zone, calculations were carried out in the two sections – directly above the support for moment  $M_p$  ('0' base) and in the  $\alpha - \alpha$  section, which was 30 cm away from the support ('1' and '2' bases). Details of the connection of two precast beams and the reinforcement of the intermediate support zone are shown in Fig. 8.

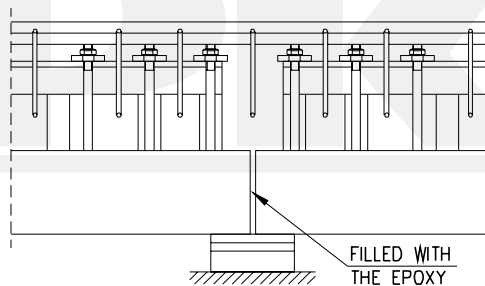


Fig. 8. Detail of the connection of two precast beams

Calculated strains were obtained by using the authors' program, which takes into account nonlinearity of concrete and reinforcement [4]. The calculations were performed twice. The first calculation took into account the presence of the reinforcement bars only in the intermediate support zone – relationship 'cal (fi)'. The second calculation also included the  $\frac{1}{2}$  H-section profile – relationship 'cal (fi + H)'. Fig. 9, 10, 11 present the comparison of the calculated relationships with real strains measured with mechanical extensometer (relationship 'exp').

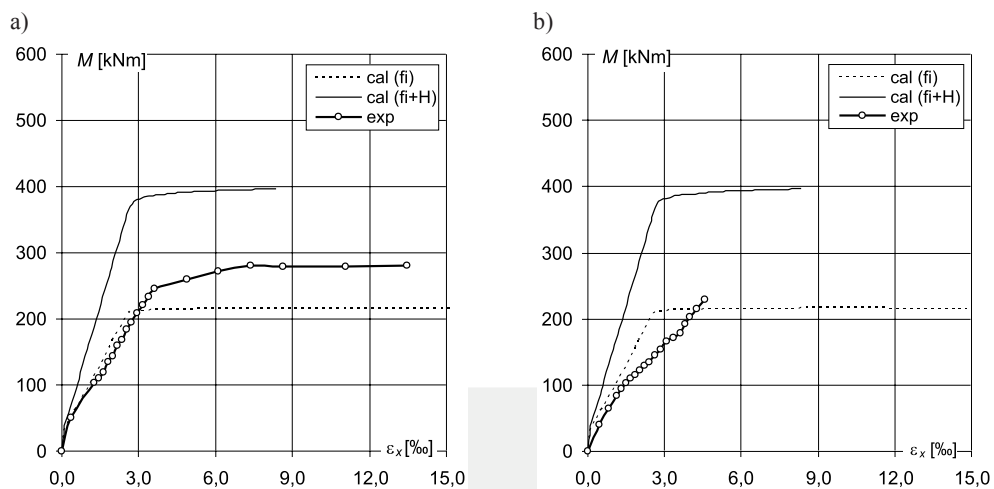


Fig. 9. Moment – strain relationships directly above the intermediate support a) beam 301, b) beam 311

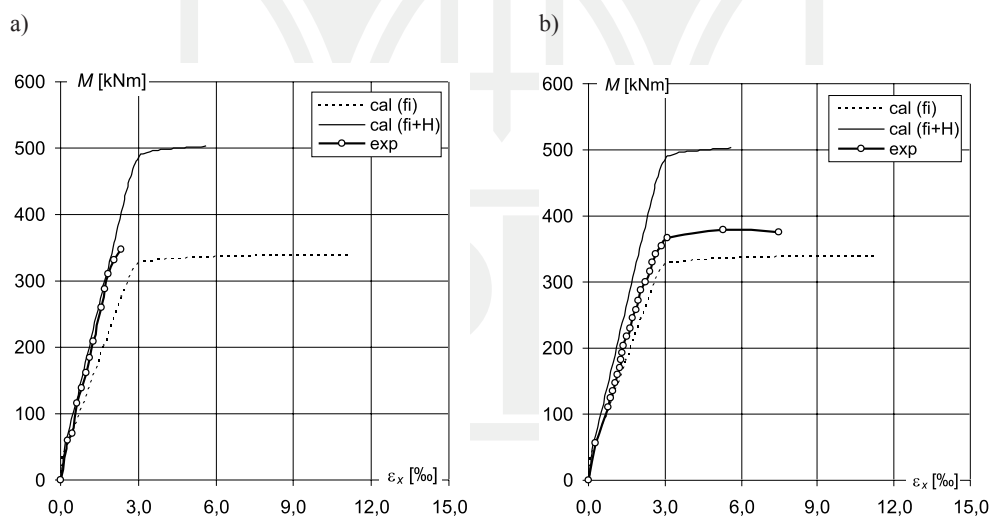
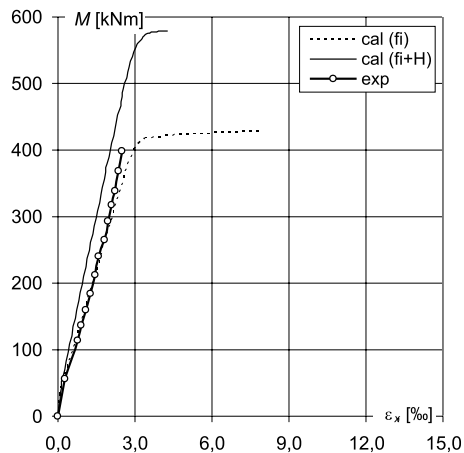


Fig. 10. Moment – strain relationships directly above the intermediate support a) beam 302, b) beam 312

The analysis shows clearly the influence of the steel profile at the strains directly above intermediate support zone, despite the fact that profiles were not continuous over the support. It is confirmed for different ratios of the upper reinforcement.

For example in beam 301, it is clear that after the beam reaches the capacity of the pure bar – reinforced section, local redistribution of the forces from bars to the steel profile emerges, and the capacity of the intermediate section is about 40% greater than the pure bar reinforced section. In specimen 303, this local redistribution of forces takes place before reaching the

a)



b)

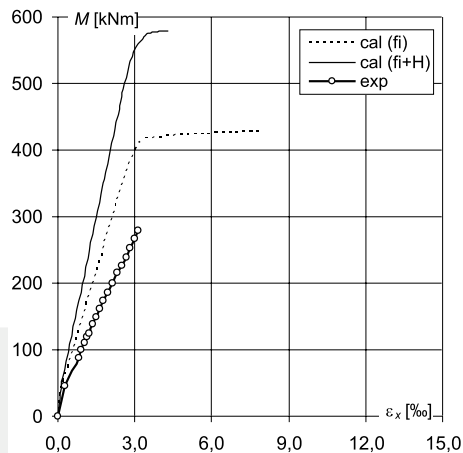
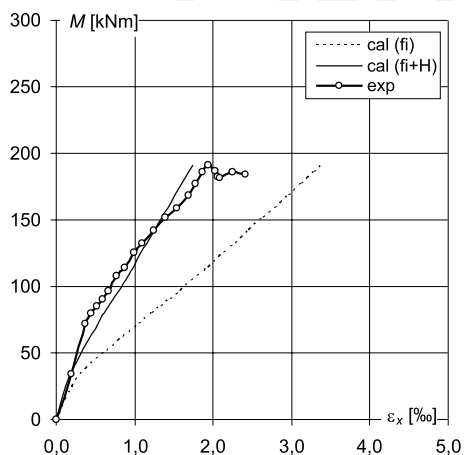


Fig. 11. Moment – strain relationships directly above the intermediate support a) beam 303,

a)



b)

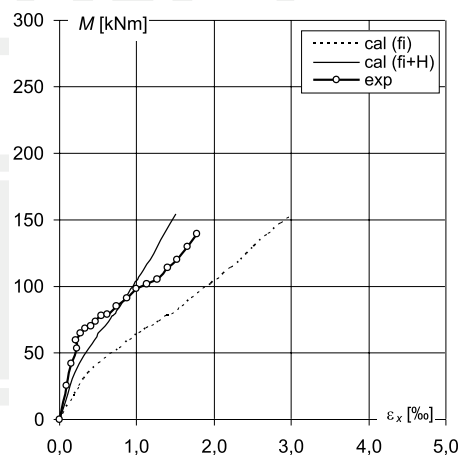


Fig. 12. Moment – strain relationships in the  $\alpha$ - $\alpha$  section a) beam 301, b) beam 311

bending load capacity calculated for reinforcement bars only. It can be noticed by observing the relationship  $M - \varepsilon$ , which at first is concurrent with relationship for the reinforcement bars only and then after reaching the value 320 kN approaching to the analytical relationship taking into consideration also rigid steel profile. Even more clearly, the impact of rigid reinforcement on the support load capacity is visible in beam 302, where in the entire range of load, strains coincide with the calculations for bars and steel profile. Obviously, the impact of the used steel profile is observed in specimen 312. The support load capacity here was higher than the calculations for bars only by about 20%. The situation is different for beam 313. In this case, the capacity for the support cross-section is definitely lower even in comparison

with the pure bar-reinforced section. This situation has come as a result of filling the gap between precast elements with too flexible material which caused different behaviour of the compression zone. A similar situation was observed in beam 311 – although in this case, despite far less rigidity of the intermediate section observed after cracking, the load capacity is higher than when taking into account only the reinforcement bars. To sum up, it can be said that in each of the beams, to greater or lesser extent, the impact of a steel profile on the relationship  $M - \varepsilon$  is visible. Of course, this also has an influence on the support load capacity.

There were also analyzed the relationships  $M - \varepsilon$  for  $\alpha - \alpha$  section, remote from the axis of the intermediate support of 30 cm. In Fig. 12–14, these strain diagrams are shown.

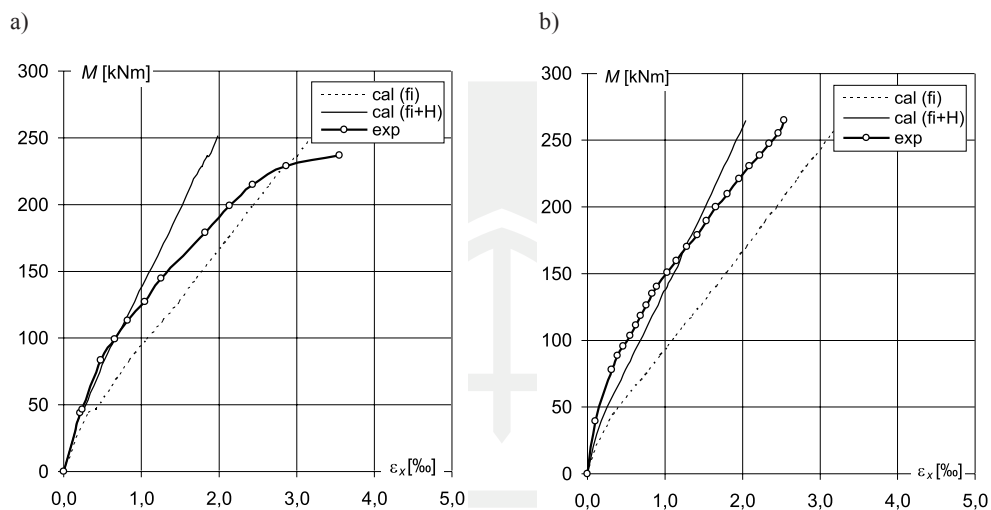


Fig. 13. Moment – strain relationships in the  $\alpha - \alpha$  section a) beam 302, b) beam 312

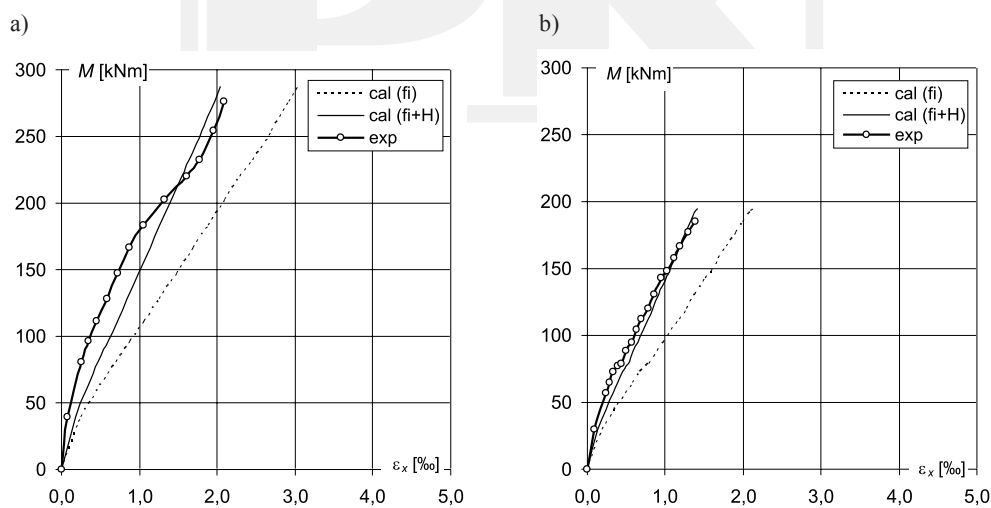


Fig. 14. Moment – strain relationships in the  $\alpha - \alpha$  section a) beam 303, b) beam 313

In the  $\alpha - \alpha$  section, according to the assumptions of a truss model, the strains depend also on the value of the shear force and accepted safety ratio for shear, thus the accepted angle  $\theta$  between the concrete compression strut and the beam axis perpendicular to the shear force, according to:

$$\cot \theta = \frac{1}{\eta} \quad (1)$$

where:

$\eta$  – safety ratio for shear.

The diagrams show the results of tests on the background of calculated relationships. dependences. Calculations include the calculated angle determined on the basis of the cross-section area, the spacing between shear reinforcement, and the shear force assuming the full redistribution (see Table 1). In these cases, the calculations were also performed twice.

Table 1

**The values of the shear forces and safety ratios for shear**

No. of the beam	Shear force [kN]	Safety ratio for shear
301, 311	365	0,55
302, 312	435	0,46
303, 313	491	0,41

In beam 301, there was observed a clear conformity of measurements with calculated values taking into account the rigid reinforcement. In specimen 302, it was also evident up to about 40% of load capacity. However, beyond this level of effort, the actual strains were higher than it would be apparent from the calculations. It should be noted that just for this specimen in the section directly over the support measured strains were fully consistent with the calculations for the reinforcement bars and rigid steel profile. The actual stiffness of the element in the beam 303 in the  $\alpha - \alpha$  section was higher, up to 80% of load capacity compared with calculations even for both reinforcements. Only when the effort was 0.8, the actual strains were similar to analytical ones. In the specimen 311 up to cracking, sectional rigidity was higher than that computed. Only after the crack strains were comparable with calculations for bars and rigid reinforcement. a similar relationship between the measurements and calculations can be observed in element 312. Instead, in the specimen 313 compliance between measured and analytical strains is directly perfect. To summarize, in the  $\alpha - \alpha$  section the influence of the rigid steel profile on the sectional stiffness is noticeable in each beam.

#### 4. Conclusions

The conducted experimental studies have shown unequivocally that despite the lack of continuous rigid reinforcement directly over the intermediate support, the influence of the steel profile on both the load capacity and stiffness is readable in both examined sections (the support section and the  $\alpha - \alpha$  section). The authors believe that this is the effect of the use of the bars with threaded ends, which anchored the rigid profile (located in tension zone) in the compression zone.

*The tests were performed under the research project No. 0348/TO2/2006/01, funded by the Ministry of Science and Higher Education in Poland.*

#### References

- [1] Staquet S., Rigot G., Detandt H., Espion B., *Innovative composite precast prestressed precambered U-shaped concrete deck for Belgium's high speed railway trains*, PCI Journal, vol. 49, no. 6, 2004.
- [2] Eurocode 2: Design of Concrete Structures – Part 1–1: General rules and rules for buildings. EN 1992-1-1:2004
- [3] Czkwianianc A., Bodzak P., Pawlica J., Habiera E., *Badania sprężonych elementów betonowych zespolonych z profilem stalowym*, Badania doświadczalne elementów i konstrukcji betonowych, Zeszyt 17/2009, Department of Concrete Structures, Lodz University of Technology, 2009.
- [4] Czkwianianc A., Kamińska M., *Metoda nieliniowej analizy żelbetowych elementów prętowych*, Studies of civil engineering, issue no. 36, KILiW, IPPT, Warsaw 1992.



MARTA KAŁUŻA, JAN KUBICA\*

## BEHAVIOUR OF UNREINFORCED AND REINFORCED MASONRY WALLETTES MADE OF ACC BLOCKS SUBJECTED TO DIAGONAL COMPRESION

### ZACHOWANIE SIĘ NIEZBROJONYCH I ZBROJONYCH MUROWANYCH ELEMENTÓW WYKONANYCH Z BLOCZKÓW Z AUTOKLAWIZOWANEGO BETONU KOMÓRKOWEGO PODDANYCH UKOŚNEMU ŚCISKANIU

#### Abstract

For more than 10 years, masonry units made of ACC turned out to be one of the most popular materials used in the construction of residential buildings in Poland and other European countries. The recommended technology for erecting such structures requires using thin bed joints and non-filled head joints. Unfortunately, masonry buildings erected using this technique are prone to damage and cracks. One of the methods to guarantee improvement of cracking resistance of this type of structure is using a special prefabricated reinforcement to be placed in bed joints. The main objective of the investigation presented here was to analyse the behaviour of unreinforced and reinforced, with prefabricated truss-type called MURFOR®, masonry wallttes. All specimens were subjected to diagonal compression. Three groups of specimens were tested, each using a different mortar coating. Testing was especially focused on the main technological problem of the proper adhesion between mortar and the reinforcement surface.

*Keywords: ACC blocks, diagonal compression, reinforced masonry, shear strength*

#### Streszczenie

Od ponad 10 lat elementy wykonane z autoklawizowanego betonu komórkowego są jednym z najbardziej popularnych materiałów stosowanych do wznoszenia budynków mieszkalnych zarówno w Polsce, jak i Europie. Zalecana technologia wykonywania konstrukcji z takich materiałów wymaga stosowania cienkich spoin wspornych i niewypełnionych spoin czołowych. Niestety konstrukcje wznoszone w tej technologii są podatne na zarysowania. Jedną z metod ograniczania zarysowań jest wprowadzenie do spoin wspornych prefabrykowanego zbrojenia. Głównym celem prezentowanych badań jest analiza zachowania się muru niezbrojonego oraz zbrojonego zbrojeniem typu MURFOR®. Badane elementy poddano ukośnemu ścisaniu. Przebadano trzy grupy elementów próbnych, różniące się sposobem otulenia zbrojenia zaprawą. W trakcie analizy zwrócono szczególną uwagę na główny technologiczny problem, dotyczący zapewnienia prawidłowej przyczepności zbrojenia do elementu murowego.

*Słowa kluczowe: bloczki z betonu komórkowego, ukośne ścisanie, zbrojone mury, wytrzymałość na ścinanie*

\* Ass. Prof. Marta Kałuża, Prof. Jan Kubica, Department of Structural Engineering, Faculty of Civil Engineering, Silesian University of Technology, Gliwice.

## 1. Introduction

It is often found that the introduction of new products in the construction market results in both positive and negative consequences. An example here may be solid blocks made of AAC with grip holes on both sides of the head. Such masonry units are recommended for erecting masonry wall structures using non-filled vertical joints. It was found that masonry structures built using this type of masonry unit displayed different behaviour than popular masonry made of other materials, especially in the case of stiffening walls typically subjected to horizontal wind loads. As a result of stress caused by horizontal shear forces, diagonal cracks are often found to develop. This situation is unacceptable mainly from a serviceability point of view. Therefore, the solution for improving crack resistance for these types of walls is in wide demand. One of the methods used is to introduce a special reinforcement which will be placed in bed joints. The most popular method recommended worldwide is to use one of the custom-prefabricated steel reinforcement types specified in EN 845-3:2000 [1]. Occasionally, and especially during last ten years, we find attempts to use composite materials (such as FRP laminates) introduced in masonry due to their improvement properties [2]. Finally, the authors also tested availability and effectiveness of CRFP and GRFP used to improve crack resistance when AAC block masonry with thin joints is subjected to in-plane shearing loads [3].

Unfortunately, the basic part of European masonry standard EN 1996-1-1:2005 [4] (Eurocode 6) does not offer any design method or formulae for the determination of the load-bearing capacity of reinforced masonry walls made of any masonry units and types of mortar which are subjected to vertical and horizontal loads. Theoretical and experimental studies on the subject have been carried out worldwide for more than 20 years. Studies carried out in other countries focus mostly on the behaviour of masonry walls with different types of reinforcement placed in bed joints and subjected to shearing and shearing with precompression – see [5], [6] and [7]. In past years, similar studies were also carried out at the Silesian University of Technology. Masonry wallettes made of solid clay bricks and general purpose class M7 mortar were subjected to horizontal shearing [8] and vertical shearing with and without precompression [9]. This type of reinforced wall was also tested and analysed in terms of seismic and dynamic shear loads and influences, especially in countries with seismic activity [10]. Unfortunately, most research works refer to using different types of bed joint reinforcement – mainly in masonry walls made of solid clay bricks or other types of bricks and blocks excluding AAC blocks. As a result, a significant lack of knowledge in this field is still found, especially in terms of the technological requirements of bed joint reinforcement application. To fill this gap, comparative tests of unreinforced and reinforced masonry wall specimens were conducted with truss-type prefabricated bed joint reinforcement. The tests were performed at the Department of Structural Engineering of Silesian University of Technology in Gliwice.

This article is an extended version of the paper presented at 7<sup>th</sup> International AMCM 2011 Conference, held in Cracow in 2011 [11]. It presents the analysis of the behaviour of unreinforced and reinforced masonry wallettes made of AAC blocks with thin joints and non-filled head (vertical) joints, based on the results of tests conducted. The experimental tests were carried out using specimens subjected to diagonally compressive loading, according to RILEM LUMB 6 [12] and American Standard ASTM E519-81 [13] regulations. These two standards are almost fully compatible. The problem of bed joint reinforcement,

correctly coated with mortar to ensure required adhesion, was identified and analysed. The article presents a comparison of two series of reinforced specimens which differed in terms of the number of mortar layers covering the steel bed joint reinforcement with the unreinforced elements taken as reference. During laboratory tests, shear stresses resulting in the development of micro-cracks and visible cracks ( $\tau_{cr}$ ), as well as ultimate shear stresses ( $\tau_u$ ) were determined and analysed. Additionally, the in-plane deformability of loaded walls (values of no-dilatational strain angle of  $\theta$  and shear modulus) during cracking and at failure was presented. To identify the impact of the reinforcement application method (using of one or two layers of mortar coating for reinforcement) on the behaviour as well as the mechanical and deformability properties of masonry, the modes of failure of all tested specimens were observed, analysed and discussed.

## 2. Tested elements and test technique

### 2.1. Description of the test specimens

Laboratory tests were carried out using small masonry wallettes made of AAC solid blocks (Ytong Planblockstyp W) and a typical thin joint mortar recommended by the block manufacturer. Specimens were prepared with non-filled head (perpend) joints with rectangular shape and overall dimensions of  $900 \times 805 \times 240$  mm (Fig. 1). AAC blocks used for preparation had the density of  $\rho_v = 600$  kg/m<sup>3</sup> and the normalised compressive strength of  $f_b = 4.65$  N/mm<sup>2</sup>. The dimensions (length  $\times$  height  $\times$  width) of individual masonry units with rectangular prism shapes were  $599 \times 199 \times 240$  mm. Each masonry unit had grip holes on both sides of the head. The mean (tested) compressive strength cement mortar supplied by the manufacturer was  $f_m = 12.4$  N/mm<sup>2</sup>.

In two series of specimens, a prefabricated truss-type steel reinforcement (compatible with the requirements specified in EN 845-3 [1]) with the characteristic value of yield strength of  $f_{yd} = 350$  N/mm<sup>2</sup> was placed in each bed joint. The reinforcement density ratio was 0.056% – which is slightly higher than the minimum value specified in Eurocode 6 [4] ( $\rho = 0.05\%$ ) for improving the material properties of masonry reinforced with this method.

In the first phase of testing, marked as **(Y-UR)** series, the specimens were unreinforced. The other two series, **(Y-R-1)** and **(Y-R-2)** included specimens with reinforced bed joints – see the test programme in Table 1. Reinforced elements differed in terms of the number of layers of mortar coating the reinforcement in each bed joint. In specimens of **(Y-R-1)** series, only one layer of mortar, located in every bed joint was applied. The reinforcement was placed into the fresh mortar. The outcome of using this method, especially if the workmanship quality is poor, is that some parts of longitudinal flat wires were not properly covered by mortar (the thickness of the mortar layer was 3 mm, but the thickness of the flat longitudinal steel wire was 1.25 mm). The reinforcement technology applied in masonry wallettes tested in the **(Y-R-2)** series was slightly changed. The reinforcement was placed between two layers of mortar (with the thickness of each layer of 2 mm). This allowed for the adequate coating of reinforcement and guaranteed a higher adhesion rate between the reinforcement and mortar; however, the total thickness of the bed joint exceeded 5 mm. Such value of the bed joint thickness is too high in relation to the maximum specified in Eurocode 6, where the thickness of thin joints is limited to 3 mm.

### Test programme

Series	Number of tested elements	Type of specimens	The number of layers of covering/ thickness of each mortar layer
<b>Y-UR</b>	5	unreinforced	1 mortar's layer/thickness of 3 mm
<b>Y-R-1</b>	5	reinforced	1 mortar's layer/thickness of 3 mm
<b>Y-R-2</b>	5	reinforced	2 mortar's layers /thickness of 2 mm each

Type of used prefabricated reinforcement, shape of tested specimens, their overall dimensions and localisation of measuring devices are shown in Fig. 1.

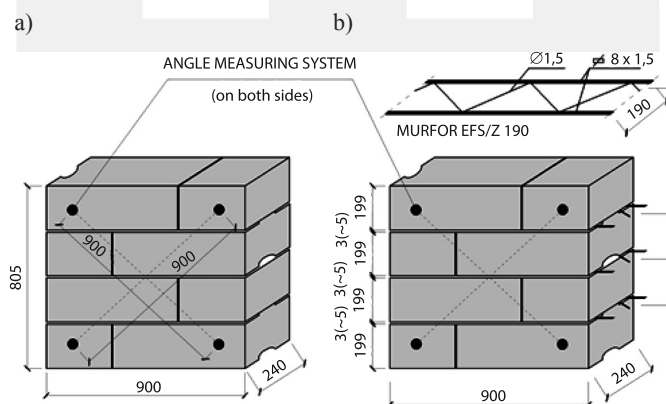


Fig. 1. Shape and overall dimensions of the test specimens: a) unreinforced specimens (**Y-UR** series), b) wallettes with truss type reinforcement in bed joints (**Y-R-1** and **Y-R-2** series)

## 2.2. Test stand and techniques

All specimens were subjected to a diagonally compressive load according to RILEM LUMB 6 [12]. This international standard also provides the procedures for the explanation of results and their analysis. The compressive load was applied using a hydraulic press machine with the range up to 2000 kN through steel blocks positioned on two diagonally opposite corners of the specimen. The load was applied in one cycle – from zero up to the failure. The diagram of the test stand is shown in Fig. 2 and the view of the specimen prepared and ready to be tested is shown in Fig. 3.

When testing each specimen, the load force level and the displacements were measured with LDV gauges. The gauges were fixed to both surfaces of each wallette (using stiff resin-epoxy glue) along two diagonals of each model. The length of the base was 900 mm taken according to the guidelines of American Standard ASTM E519-81 [13], and should cover the greater part of the length of the specimens. Additionally, at failure, the crack pattern of each specimen was observed and recorded.

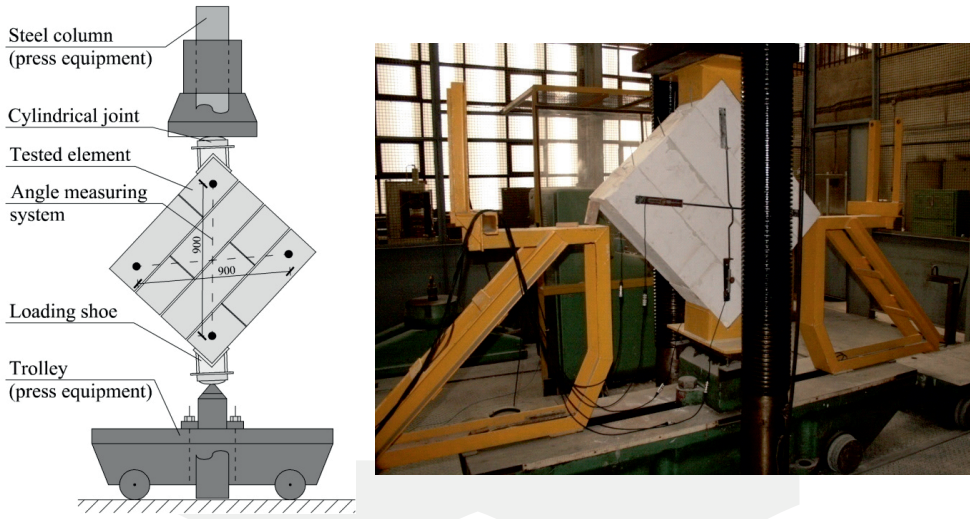


Fig. 2. Scheme of the test stand and view of the masonry wallettes ready to test

For each re-ordered force level  $F_i$  (at the  $i$ -th load level) the average value of the shear stresses  $\tau_{v,i}$ , defined as the quotient of load force  $F_i$  and the vertical cross-section area of the wall specimen  $A_h$  (along the diagonal), was calculated:

$$\tau_{v,i} = \frac{F_i}{A_h} = \frac{F_i}{t\sqrt{l^2 + h^2}}$$

where:

- $F_i$  – is the vertical load value at the  $i$ -th loading level,
- $t$  – 240 mm is the thickness of the wall specimens,
- $l$  – 922 mm is the length of the wallette,
- $h$  – 1009 mm is the height of the specimen.

To measure the in-plane deformability of each specimen during load application, inductive, measurement (LDV) system was mounted on both surfaces of the tested wallette (Fig. 2).

The values of the non-dilatational strain angle (shear strain)  $\Theta_i$  were calculated on the basis of the horizontal and vertical length changes according to trigonometric (deformed base measurement) relationship, separated as shown in Fig. 3.

The non-dilatational strain angle at  $i$ -th level was determined by the following formula:

$$\Theta_i = 2 \arctg \left( \frac{|\Delta x| + |\Delta y|}{x + y + |\Delta x| - |\Delta y|} \right)$$

where:

- $\Delta x$  – is the change in length of the horizontal measuring base ( $x$  – direction),
- $\Delta y$  – is the change in length of the vertical measuring base ( $y$  – direction),
- $x, y$  – is the primary length of the bases (900 mm), as appropriate.

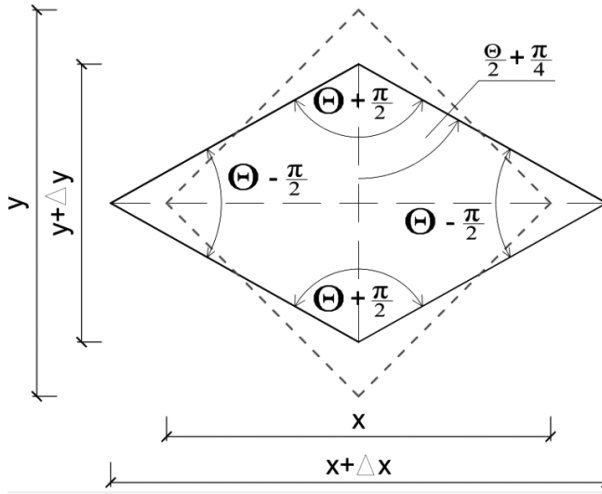


Fig. 3. Scheme for determination of non-dilatational strain angle (shear strain)

The shear modulus  $G_i$  (at the  $i$ -th load level) defined as the quotient of stresses  $\tau_{v,i}$  and average value of corresponding to its' non-dilatational strain angle  $\Theta_i$  was calculated from well-known formula:

$$G_i = \frac{\tau_{v,i}}{\Theta_i}$$

When a visible crack or cracks (with width greater than 0.1 mm) were observed, the values of the shear modulus  $G_{cr}$  was determined with the adequate level of  $F_{cr}$ , shear stresses  $\tau_{cr}$  to be loaded and their corresponding values of shear strains of  $\Theta_{cr}$ .

At failure, the ultimate load level taken as the ultimate value of compressive force  $F_u$  was recorded and the maximum shear stresses  $\tau_u$  and shear strain of in-plane deformation  $\Theta_u$ , together with shear modulus  $G_u$  were calculated.

### 3. Results and analysis

#### 3.1. Mode of failure

The modes of failure of unreinforced specimens (Y-UR) were typical for the diagonally compressed elements. In all masonry wallettes, the crack was running diagonally across the whole specimen. This crack was oriented perpendicularly to the direction of principal tensile stresses. Fig. 4 shows an exemplary view of unreinforced elements with visible diagonal cracks.

In two groups of reinforced specimens in the (Y-R-1) and (Y-R-2) series, the modes of failure were completely different and significantly dependent on the number of mortar layers used to coat the bed joint reinforcement. In all specimens where reinforcement

consisted of only one layer of mortar (**Y-R-1**), the damage was caused by splitting. The splitting occurred between the masonry units and reinforcement, always in the location where the mortar coating did not suitably cover the whole surface of the reinforcement (flat steel longitudinal rods of the truss-type reinforcement). This type of failure shows that using only one layer of mortar in reinforced masonry was not sufficient to guarantee a full connection (adhesion) between the reinforcement and mortar. Additionally, based on the deformation observed, the resulting damage was dangerous for the stability of the whole structure.

In (**Y-R-2**) series, a completely different mechanism of failure for all specimens with two layers of mortar coating was observed. No splitting effect between the reinforcement and masonry units was noticed. The damage was caused by a roughly vertical crack, which was always running through the non-filled perpend joints. As in the case of cracks observed in unreinforced specimens (the failure which is typical for the elements subjected to diagonal compression), the crack was located along the axis which was perpendicular to the direction of the diagonal tensile stresses. The failure was pronounced when the crack width exceeded 1 mm. A vertical crack, with the width smaller than 0.1 mm was considered to be a secondary cracking state because no other type of damage was noticed at that time. The failure mode of all specimens of (**Y-R-2**) series can be considered safe, with no visible significant deformation and rapid action. The failure mode observed demonstrated a better behaviour of the bond between the reinforcement and masonry mortar when two layers of mortar were used. This situation was different than the modes of failure noticed in specimens in (**Y-R-1**) series, where the destabilisation of the elements inside the wallette occurred.

The pictures of damaged reinforced specimens are shown in Fig. 5. Fig. 5a and 5b present elements with one layer of mortar (**Y-R-1**), while Fig. 5c and 5d show modes of failure of wallettes with two layers of covering mortar (**Y-R-2**). Additionally, in Fig. 5b the splitting surface and the reinforcement without covering mortar are clearly visible.



Fig. 4. View of typical modes of failure in case of unreinforced specimens

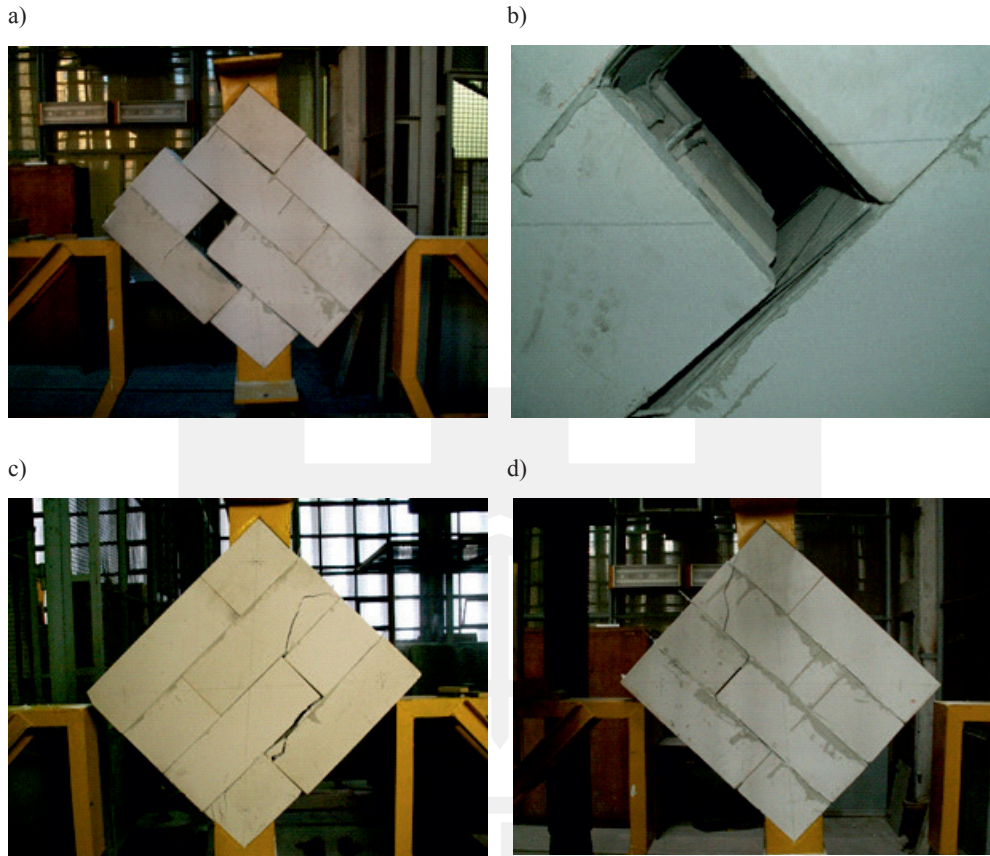


Fig. 5. Typical modes of failure of reinforced specimens: a) specimens made with one mortar layer (Y-R-1), b) splitting surface with visible reinforcement non-covered by mortar, c) and d) specimens made using two layers of mortar (Y-R-2)

### 3.2. State of cracking and ultimate stresses

During laboratory tests, at each measuring step (approximately every 30 seconds), the compressive force and displacements measured by inductive LDV gauges were recorded. Based on this, the characteristic values of forces and stresses (corresponding with the cracking moments and at the state of failure) were determined. Table 2 shows the values of cracking forces  $F_{cr1}$ ,  $F_{cr2}$  and the maximum forces (the ultimate value) recorded at the state of failure  $F_u$  and corresponding to each force of cracking stresses  $\tau_{cr1}$ ,  $\tau_{cr2}$  and the ultimate shear stresses  $\tau_u$  observed. Table 3 shows the mean values of all characteristic forces ( $F_{cr1,mv}$ ,  $F_{cr2,mv}$ ,  $F_{u,mv}$ ) and stresses ( $\tau_{cr1,mv}$ ,  $\tau_{cr2,mv}$  and  $\tau_{u,mv}$ ) grouped for unreinforced specimens (Y-UR), the reinforced wallethes with one layer of mortar (Y-R-1) and the reinforced specimens with reinforcement placed between two mortar layers (Y-R-2). Additionally, the reinforced specimens (both Y-R-1 and Y-R-2) were compared with the unreinforced specimens (Y-UR) in terms of the first cracking stresses and ultimate stresses.

Table 2

Values of diagonal compressive forces and calculated shear stresses at the state when first crack appear and at the state of failure

Element	$F_{cr1}$ [kN]	$\tau_{cr1}$ [N/mm <sup>2</sup> ]	$F_{cr2}$ [kN]	$\tau_{cr2}$ [N/mm <sup>2</sup> ]	$F_u$ [kN]	$\tau_u$ [N/mm <sup>2</sup> ]
<b>Unreinforced specimens</b>						
Y-UR-1	16.78	0.058	-	-	110.03	0.380
Y-UR-2	17.08	0.059	-	-	108.20	0.373
Y-UR-3	19.37	0.067	-	-	105.43	0.364
Y-UR-4	18.62	0.064	64.66	0.223	87.98	0.304
Y-UR-5	18.87	0.065	-	-	93.56	0.323
<b>Reinforced specimens with one layer of covering mortar</b>						
Y-R-1-1	17.69	0.061	-	-	102.50	0.354
Y-R-1-2	26.02	0.090	-	-	98.96	0.342
Y-R-1-3	18.19	0.063	60.57	0.209	97.04	0.337
Y-R-1-4	27.47	0.095	59.22	0.204	93.81	0.324
Y-R-1-5	19.29	0.067	-	-	108.46	0.375
<b>Reinforced specimens with two layers of covering mortar</b>						
Y-R-2-1	85.07	0.294	104.21	0.360	128.50	0.443
Y-R-2-2	51.89	0.179	120.36	0.415	135.69	0.468
Y-R-2-3	79.09	0.273	134.44	0.464	149.97	0.518
Y-R-2-4	80.55	0.278	110.10	0.380	132.46	0.457
Y-R-2-5	82.44	0.284	104.92	0.362	121.43	0.419

**Mean values of characteristics diagonal compressive forces and shear stresses for all series of tested elements**

Element	$F_{cr1,mv}$ [kN]	$\tau_{cr1,mv}$ [N/ mm <sup>2</sup> ]	$F_{cr-vis,mv}$ [kN]	$\tau_{cr-vis,mv}$ [N/mm <sup>2</sup> ]	$F_{u,mv}$ [kN]	$\tau_{u,mv}$ [N/mm <sup>2</sup> ]
UnreinforcedY- UR	18.14	0.063	–	–	101.04	0.359
Reinforced with 1 layer of mortar Y-R-1	21.73	0.075	59.90*	0.207*	100.15	0.346
Reinforced with 2 layers of mortar Y-R-2	75.81	0.262	114.81	0.396	133.61	0.461
Y-R-1/Y-UR		<b>1.19</b>				<b>0.96</b>
Y-R-2/Y-UR	–	<b>4.16</b>		–		<b>1.28</b>
Y-R-2/Y-R-1		<b>3.49</b>				<b>1.33</b>

\* uncertainty average values – obtained on the basis of only two results.

The analysis of both the cracking and maximum (ultimate) stresses at failure leads to very interesting conclusions. Development of the first cracking was recognised as a typical micro-crack, barely visible on the surface of the element. Their occurrence in masonry of non-filled perpend joints caused during the first load phase, the closing of internal spaces between the masonry units and tightening of the masonry wallettes structure. This phenomenon was noticed during the first cracking observed on the basis of the recorded data and recognised as disturbance on the displacements diagram. The next cracking state (the second crack), clearly observed in reinforced specimens with a proper bonding between the reinforcement and masonry units (using two layers of mortar **Y-R-2**), was found when visible vertical cracks appeared on the surface of the specimens. The typical width of the cracks was smaller than 0.1 mm. The development of the second crack was also noticed on the displacement diagrams as the changing of the inclination of the graph line.

In both reinforced elements, the values of cracking stresses (first and second) were higher than those noticed in the unreinforced specimens. In the unreinforced masonry wallettes, the first cracks were found for stresses in the range of  $\tau_{cr} = 0.058 \div 0.067$  N/mm<sup>2</sup>. Slightly higher values ( $\tau_{cr} = 0.061 \div 0.095$  N/mm<sup>2</sup>) were recorded for reinforced specimens with 1 layer of mortar. When using 2 layers of mortar coating, the increase of stresses at the cracking moment was significant because the stresses amounted to  $\tau_{cr} = 0.179 \div 0.294$  N/mm<sup>2</sup>. For both types of the reinforced masonry wallettes, the delay in development of cracks was noticed, but in the first group of reinforced elements (**Y-R-1**), the increase analysed for the average values amounted to only 19%, and in the reinforced elements with 2 layers of mortar coating (**Y-R-2**), it was much more significant and was as high as 316%. The comparison of both reinforced types of specimens shows that the introduction of two layers of reinforcement mortar coating corresponded with 249% increase in micro-cracking stresses.

Analysis of a possibility of a second crack occurrence shows that only specimens with two layers of mortar developed visible cracks with no ensuing danger of rapid damage to masonry wallettes. The value of stresses, at the time when the second crack was observed, was very high and was determined to be equal to 0.86% of the ultimate stresses. In unreinforced elements and the first series of reinforced elements (**Y-R-1**), a visible and safe second crack was practically not observed. The development of cracks in the unreinforced element occurred together with a simultaneous rapid damage of this element. In reinforced specimens with one layer of mortar coating, the crack development was the result of a splitting effect observed and recognised as the failure state of this element.

A similar tendency was found in the analysis of the ultimate stresses. Improvement of the maximum stresses was recorded only for two layers of mortar application. Unfortunately, when using only one layer of mortar, the failure occurred almost at the same moment as the failure of unreinforced specimens (the difference of the ultimate stresses amounted only up to 1% and should be neglected). This phenomenon was associated with a splitting effect observed in reinforced specimens (**Y-R-1**), which occurs instead of a wide vertical crack observed in unreinforced specimens (**Y-UR**).

In the second group of reinforced specimens (with two layers of mortar coating in **Y-R-2** series), failure occurred later than in unreinforced specimens. The maximum (ultimate) stresses were higher than 35% when compared to the maximum stresses noticed for unreinforced elements. In this case, reinforcement was placed between the two layers of mortar, which allowed for a better bonding between the reinforcement and ACC blocks and thus the lack of occurrence of the splitting effect.

### 3.3. In-plane deformations

An analysis of deformation characteristics for the tested elements was conducted on the basis of in-plane deformability parameters obtained from the displacement measured using inductive gauges sets fixed along the diagonals of both surfaces of the specimens. The recorded data allowed for the determining of values of the non-dilatational strain angles occurring in the in-plane stiffness of masonry wallettes subjected to diagonal compression. Additionally, the values and changes of shear modulus were also analysed.

In Table 4, the values of non-dilatational strain angles (shear strains), determined at the time of the appearance of first and second cracks  $\Theta_{cr1}$ ,  $\Theta_{cr2}$  and at the state of failure  $\Theta_u$  for all tested specimens are presented. The table also covers the average values of shear strains  $\Theta_{cr,mv}$ ,  $\Theta_{u,mv}$  and shear modulus for both cracking moment  $G_{cr}$  and the average value  $G_{cr,mv}$ .

A comparison of calculated values, presented in Table 4, indicates that deformation of both types of reinforced specimens should be discussed separately, because the behaviour of specimens of series (**Y-R-1**) was significantly different than that of the wallettes of (**Y-R-2**) series. Additionally, the deformation had to be analysed together with the values of stresses observed for characteristic moments, as shown in Table 2.

Using only one layer of mortar coating for the reinforced specimens (**Y-R-1**) resulted in the element's behaviour being almost the same as unreinforced specimens. The failure of both masonry wallettes (**Y-UR** and **Y-R-1**) was caused by the same shear stresses and the same deformability parameter. The non-dilatational strain angle calculated for reinforced specimens was  $\Theta_u=1.161$  mm/m, where the average value of strain angle for unreinforced

Values of deformation parameters and shear modulus

Element	$\Theta_{cr1}$ [mm/m]	$G_{cr1}$ [N/mm <sup>2</sup> ]	$\Theta_{cr2}$ [mm/m]	$G_{cr2}$ [N/mm <sup>2</sup> ]	$\Theta_u$ [mm/m]	$G_u$ [N/mm <sup>2</sup> ]
<b>Unreinforced specimens</b>						
Y-UR-1	0.169	343	-	-	1.074	345
Y-UR-2	0.333**	177**	-	-	2.942**	127
Y-UR-3	0.169	394	-	-	1.280	284
Y-UR-4	0.193	332	0.751	297	1.142	251
Y-UR-5	0.136	480	-	-	0.749	422
<b>Reinforced specimens with one layer of covering mortar</b>						
Y-R-1-1	0.062	981	-	-	1.069	331
Y-R-1-2	0.126	715	-	-	0.926	369
Y-R-1-3	0.089	782	0.257	833	0.797	565
Y-R-1-4	0.072	1312**	0.253	807	0.690**	469
Y-R-1-5	0.094	705	-	-	1.851	179
<b>Reinforced specimens with two layers of covering mortar</b>						
Y-R-2-1	0.828	354	1.048	343	2.416	184
Y-R-2-2	0.308	581	0.980	424	2.286	205
Y-R-2-3	0.527	518	1.081	429	2.330	222
Y-R-2-4	0.914	304	1.374	277	2.448	139
Y-R-2-5	0.774	368	1.063	341	1.436	292

\*\* uncertain value not taken into account in mean values determination.

specimens was only 10% lower ( $\Theta_u=1.061$  mm/m). Development of the second cracking state was not noticed in either element; however, in two cases of reinforced specimens (most likely due to the fact that the reinforcement coating was a little better) a vertical crack was observed, but the deformation observed at the moment of cracking was not very high. Only in the case of the first cracking recorded, the strain deformation of the reinforced element was different than the one observed for the unreinforced element. The first micro-cracks occurred almost at the same load level as for the unreinforced specimens, but the corresponding deformation was smaller.

Table 5

**Values of deformation parameter and shear modulus**

<b>Element</b>	$\Theta_{cr1,mv}$ [mm/m]	$G_{cr1,mv}$ [N/mm <sup>2</sup> ]	$\Theta_{cr2,mv}$ [mm/m]	$G_{cr2,mv}$ [N/mm <sup>2</sup> ]	$\Theta_{u,mv}$ [mm/m]	$G_{u,mv}$ [N/mm <sup>2</sup> ]
Unreinforced <b>Y-UR</b>	0.200	387	–	–	1.061	288
Reinforced with 1 layer of mortar <b>Y-R-1</b>	0.089	796	0.255*	820*	1.161	383
Reinforced with 2 layers of mortar <b>Y-R-2</b>	0.670	425	1.109	363	2.183	208

\* uncertain average values – obtained on the basis of only two results.

Analysis of the in-plane deformation of reinforced specimens, where reinforcement was fully covered by the mortar (two layers of mortar were used in **Y-R-2**), indicated a proper behaviour of these elements, especially in relation to masonry wallettes with the reinforcement placed only in one mortar layer (**Y-R-1** series). The micro-cracking in these elements occurred much later than in unreinforced specimens (the difference was about 330%). This is associated with higher deformation of specimens and relatively lower increase of shear modulus calculated at the development of the first crack. The increase of non-dilatational strain angles was up to 235% with a 10% increase in the values of shear modulus. This phenomenon was the result of a better adhesion between the reinforcement surface and masonry units. The reinforcement deforms together with the specimens when applying load and results in the masonry wallette being much more flexible and ductile. The increase of ductility was associated with the obvious development of the second crack and corresponded with intense in-plane deformation. The calculated average value of the non-dilatational strain angle for **Y-R-2** series of reinforced specimens ( $\Theta_{cr2} = 1.109$  mm/m) was comparable to the value determined for unreinforced elements (**Y-UR**) at failure ( $\Theta_u = 1.061$  mm/m). However, the second crack did not cause damage of reinforced elements (series **Y-R-2**). The in-plane deformation of reinforced masonry wallettes observed at failure was significant (when compared to the unreinforced specimens) and was as high as  $\Theta_u = 2.138$  mm/m. This resulted in a positive impact on the deformation of reinforced specimen by correct coating of the reinforcement by mortar. First of all, for reinforced

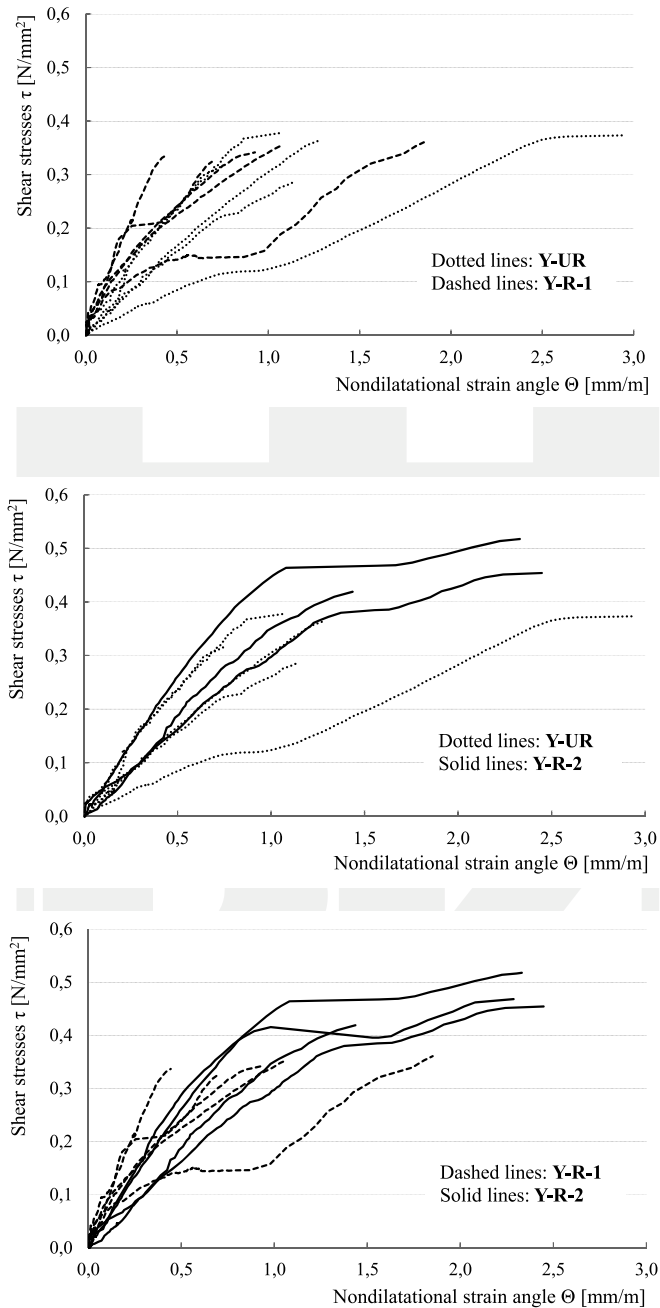


Fig. 6. Comparison of shear stress – non-dilatational strain angle ( $\tau - \Theta$ ) relationships for: a) unreinforced specimens (Y-UR) and reinforced specimens with one layer of mortar (Y-R-1), b) unreinforced specimens (Y-UR) and reinforced specimens with two mortar's layers (Y-R-2) c) both reinforced specimens (Y-R-1 and Y-R-2)

masonry wallettes, the no-crack phase was significantly extended (almost four times); secondly, the possibility of visible cracking development with no damage to the element was observed and thirdly, the deformation of the element at failure was two times higher than that of the unreinforced specimens. These phenomena are very desirable in the event of the occurrence of vertical forces (shearing).

In order to show noticed above remarks and observations, some diagrams with shear stress – shear strain ( $\tau - \Theta$ ) relationships of all specimens were presented. Figures 4a and 4b show the behaviour of deformation of unreinforced specimens (**Y-UR**) in comparison with reinforced specimens with one layer of mortar (**Y-R-1**) and with two layers of mortar (**Y-R-2**). In the Fig. 4c the comparison of both reinforced specimens was presented.

#### 4. Conclusions

The results of the carried out investigations of unreinforced and reinforced, using truss type bed joint reinforcement, masonry wallettes subjected to diagonally compressive loading were presented and discussed. Based on them, the significant influence of proper bed joint reinforcement covering by mortar on behaviour, mode of failure and positive modification of mechanical properties such reinforced masonry made of AAC blocks was recorded. The technological problem of bed joint reinforcement correct covering by mortar to ensure required adhesion was examined. Simultaneously, a very important influence of workmanship quality on behaviour and material properties of such masonry was stated.

In spite of testing only one type of masonry unit and mortar destined for thin joints, the obtained results permitted the formulation of some general conclusions for bed joint reinforced masonry walls subjected mainly to in-plane, especially shear loading:

1. A significant enhancement of material properties (i.e. shear strength) is observed only in situations where reinforcement is fully covered by mortar. Practically, this is not possible to guarantee using only one mortar layer. According to the presented investigation, in cases of masonry walls with bed joint reinforcement, two mortar layers (with the total thickness ca.  $2 \times 2$  mm) should be used.
2. Using two layers of mortar has a very positive influence on crack resistance and mode of failure, shear (diagonal tensile) strength, and state of in-plane deformations of sheared (diagonally compressed) masonry. Splitting effect at the state of failure was not observed, but a shear strength enhancement of over 20% was recorded.
3. Reinforced masonry wallettes with two mortar layers were characterised by over three times higher shear stresses recorded for the state of first crack appearance and quite similar values of corresponded to them shear modulus in comparison to unreinforced members.
4. In case of masonry walls made using thin joints, it is very important to ensure a good quality of workmanship.
5. It is necessary to introduce Eurocode 6 regulations using joints with medium thickness, i.e. between 5 to 8 mm. Using bed joint reinforcement in situations where the maximum permitted thickness for thin joints should not exceed 3 mm is practically not possible.

*Research works presented in this paper were carried out at the Department of Structural Engineering with partially financial support of BEKAERT S.A., Zwevegem, Belgium and own university grant of Politechnika Śląska in Gliwice.*

## References

- [1] EN 845-3:2000. Specification for ancillary components for masonry – Part 3: Bed joint reinforcement of steel meshwork, CEN, 2000.
- [2] Nolph S.M., *In-plane shear performance of partially grouted masonry shear walls*, Master thesis, Washington State University, 2010.
- [3] Kubica J., Kałuża M., *Diagonally compressed AAC Block's masonry – effectiveness of strengthening using CRFP and GRFP laminates*, Proceedings 8<sup>th</sup> International Masonry Conference, Masonry (11), Ed. by W. Jäger, B. Haseltine & A. Fried, Dresden 2010, 419-428.
- [4] EN 1996-1-1:2005 EUROCODE 6, Design of Masonry Structures – Part 1-1: Common Rules for Reinforced and Unreinforced Masonry Structures, CEN, 2005.
- [5] Sheppard P., Tercely S., Turnšek V. *The influence of horizontally placed reinforcement on the shear strength and ductility of masonry walls*, Proceedings 6<sup>th</sup> WCEE, New Dehli 1977.
- [6] Tercely S., Sheppard P., *The load-carrying capacity and deformability of reinforced and unreinforced masonry walls*, Proceedings CIB W23 Commission Symposium on Wall Structures, Vol. I, Warszawa 1984.
- [7] Tomažević M., Žarnić R., *The effect of horizontal reinforcement on the strength and ductility of masonry at shear failure*, Proceedings 7<sup>th</sup> International Brick Masonry Conference, Vol. II, Melbourne 1985.
- [8] Jasiński R., *Load-bearing capacity and deformability of reinforced masonry walls sheared horizontally*, (in Polish), PhD Thesis, Politechnika Śląska, Gliwice 2005.
- [9] Piekarczyk A., *Load-bearing capacity and deformability of reinforced masonry walls subjected to shearing in vertical direction* (in Polish), PhD Thesis, Politechnika Śląska, Gliwice 2005.
- [10] Tomažević M., Lutman M., *Design of reinforced masonry walls for seismic actions*, Proceedings 8<sup>th</sup> International Brick Masonry Conference, Vol. II, Dublin 1988.
- [11] Kubica J. Kałuża M., *Comparative tests of diagonally compressed unreinforced and bed joint reinforced masonry made of acc block*, Proceedings 7<sup>th</sup> International Conference AMCM'2011, Kraków, 2011.
- [12] RILEM LUMB 6, *Diagonal Tensile strength. Tests of Small Wall Specimens*, TC 73 – LUM, 1991.
- [13] ASTM E519-81 1981, *Standard Test Method for Diagonal Tension (Shear) in Masonry Assemblages*, American Society for Testing Materials.

BARBARA KLEMCZAK, AGNIESZKA KNOPPIK-WRÓBEL\*

## NUMERICAL MODEL FOR ANALYSIS OF EARLY-AGE THERMAL–MOISTURE EFFECTS IN AN RC WALL

### MODEL NUMERYCZNY DO ANALIZY WCZESNYCH WPLYWÓW TERMICZNO-WILGOTNOŚCIOWYCH W ŚCIANIE ŻELBETOWEJ

#### Abstract

The paper presents the original numerical model for simulation of thermal, moisture and mechanical effects in concrete structures with an example of application. The influence of different curing conditions on the temperature and moisture distribution in RC wall was investigated. The stress state and the damage intensity factor were determined and the areas of possible cracking were selected as well.

*Keywords: early-age concrete, FEM analysis, thermal–shrinkage stresses, RC wall*

#### Streszczenie

W artykule przedstawiono autorski model numeryczny do symulacji zjawisk termicznych, wilgotnościowych i mechanicznych w konstrukcjach betonowych wraz z przykładem jego zastosowania. Zbadano wpływ warunków betonowania i pielęgnacji na rozkład temperatur i wilgotności w ścianie żelbetowej. Wyznaczono stan naprężenia oraz wyężenia, określając również możliwe obszary zarysowania.

*Słowa kluczowe: młody beton, analiza MES, naprężenia termiczno-skurczowe, ściana żelbetowa*

\* DSc. Eng. Barbara Klemczak, MSc. Eng. Agnieszka Knoppik-Wróbel, Department of Structural Engineering, Faculty of Civil Engineering, Silesian University of Technology.

## 1. Introduction

In the phase of concrete structures erection, the loads originating from the material of which a structure is made play a significant role. These loads, caused by temperature and humidity changes of early-age concrete, are defined as indirect interactions. Temperature changes in a concrete structure are related to the exothermic nature of cement hydration. The concrete temperature increases as a result of heat released in this process. The cooling of surface layers of the structure and a relatively low value of concrete thermal conductivity result in temperature differences between the surface layers and the interior of the structure. Concrete curing is also accompanied by a migration of moisture. It is caused by the process of cement hydration and moisture exchange within the environment in conditions of variable temperatures. Thus the movement of moisture may result from moisture diffusion, i.e. from the existence of moisture concentration gradients, and from the thermal diffusion, i.e. due to the existence of temperature gradients.

The originating non-linear and non-stationary coupled thermal–moisture fields generate self-induced stresses in the structure (related to internal constraints of the structure, resulting from inhomogeneous distribution of thermal–moisture fields) and restraint stresses (related to limitation of structure deformations freedom). These stresses can reach a significant level and as a consequence, cracking may occur. Two kinds of cracking in early-age concrete can be distinguished. In massive members, such as thick foundation blocks, a significant temperature generated during the hydration process is generally different in each point of the structure. The tensile stresses are induced by differences between the interior and surface temperatures of the block. Although the interaction with subsoil limits the possibility of deformations, the self-induced stresses are predominant in such structures. In medium-thick structures such as walls, the thermal and shrinkage deformations are usually prevented by a restraint, e.g. if a wall is cast against an old set concrete. The cracking develops mainly due to restraint stresses generated by shrinkage and thermal effects.

## 2. Modeling strategy

Early-age concrete is undoubtedly one of the most difficult structural materials for modeling. The difficulties arise from a complex concrete structure which is additionally subjected to transformations as a result of cement hydration. Initially, it is a mixture of liquids and solids of varying diameters and shapes. Such a medium is characterized with strong viscous and plastic properties. With progressing cement hydration, concrete becomes a solid, with elastic, viscous and plastic characteristics, where the mutual proportions of these features depend on the concrete hardening advancement. Taking into account the concrete structure and its changes during hardening, two possibilities to model early-age concrete appear.

The first approach is related to structural models, in which a precise analysis of the physical phenomena and the material's internal structure influence on these phenomena is made. Appropriate constitutive equations describing the migration of heat, moisture and stress state are derived for the solid, liquid and gaseous phase of the medium and then averaged for a multi-phase medium. The second approach is related to phenomenological models where concrete is treated as a continuous medium. A detailed analysis of physical processes related

to phase transitions and chemical processes occurring in hardening concrete is neglected in these models and a macroscopic description of the thermal–moisture–mechanical phenomena is used. It should be mentioned that the phenomenological models are applied more often for the analysis of the discussed phenomena [1–6] but there are also some proposals of the structural models [7–9].

The next issue in modeling of the early-age concrete is an approach to coupling of temperature, moisture and stresses. In this field, it is possible to assume a full coupling of thermal–moisture–mechanical fields and to separate thermal–moisture and mechanical fields. The first approach takes into account the influence of mechanical field changes on changes of concrete temperature and humidity. In the second approach, the influence of the mechanical field on thermal diffusion processes is neglected. In such a model, the thermal–moisture fields are determined first. The stress state is determined assuming that the thermal–shrinkage strains, defined based on temperature and humidity changes, have a distortional nature. In turn, in the area of thermal–moisture fields modelling, it is possible to assume a full coupling of thermal and humidity fields to neglect the influence of humidity changes on temperature changes (partial coupling of equations) and also to assume uncoupled equations. At this point, it is important to mention that in many models proposed for the description of thermal and moisture fields, the equations are formulated independently, neglecting their coupling [10–11].

It is also necessary to assume appropriate material model of early-age concrete as the basis to define the stress state and the damage intensity of the structure. The material model should consider variability of concrete mechanical properties related to its aging as well as viscous effects. Viscous effects should not be neglected in the model, both due to a long-term nature of thermal–shrinkage loads and properties of early-age concrete, which shows features of this type much stronger than in the mature concrete. Now, to evaluate thermal–shrinkage stresses, a viscoelastic model is most often used [1–6] but attempts are also made to use more advanced models: viscoelasto–plastic [12], elasto–viscoplastic [13] or viscoelasto–viscoplastic [14] models.

### **3. Numerical model**

The presented numerical model can be classified as a phenomenological model. The influence of the mechanical fields on the temperature and moisture fields was neglected, but the thermal–moisture fields were modeled using the coupled equation of the thermodiffusion. Therefore, the complex analysis of a structure consists of three steps. The first step is related to the determination of temperature and moisture development, in the second one, thermal–shrinkage strains are calculated and these results are used as an input for computation of stress in the last step. For the purpose of determination of the stress state in the early-age concrete structures, the viscoelasto–viscoplastic model with a consistent conception was proposed. The proposed model is an extension of the earlier proposed viscoelasto–plastic model. With respect to the engineering application of the theoretical models, the computer programs were also developed. Some details of the model are given below and a full description of the model and computer programs: TEMWIL, MAFEM\_V EVP and MAFEM3D, is contained in [15].

## 3.1. Thermal and moisture analysis

The coupled temperature and moisture fields in early-age concrete can be described by the following equations [15–16]:

$$\dot{T} = \text{div}(\alpha_{TT} \text{grad } T + \alpha_{TW} \text{grad } c) + \frac{1}{c_b \rho} q_v \quad (1)$$

$$\dot{c} = \text{div}(\alpha_{WW} \text{grad } c + \alpha_{WT} \text{grad } T) - K q_v \quad (2)$$

where:

$T$	–	temperature [K],
$c$	–	moisture concentration [kg/kg],
$\dot{T} = \frac{\partial T}{\partial t}$	–	time derivative of temperature,
$\dot{c} = \frac{\partial c}{\partial t}$	–	time derivative of moisture concentration,
$\alpha_{TT}$	–	coefficient of thermal diffusion [m <sup>2</sup> /s],
$\alpha_{WW}$	–	coefficient of moisture diffusion [m <sup>2</sup> /s],
$\alpha_{TW}$	–	coefficient representing the influence of moisture concentration on heat transfer [m <sup>2</sup> K/s],
$\alpha_{WT}$	–	thermal coefficient of moisture diffusion [m <sup>2</sup> /(sK)],
$c_b$	–	specific heat [kJ/(kgK)],
$\rho$	–	density of concrete [kg/m <sup>3</sup> ],
$K$	–	coefficient of water–cement proportionality, which describes the amount of water bounded by cement during the hydration process with the rate of heat generated by cement hydration per unit volume of concrete [m <sup>3</sup> /J],
$q_v$	–	rate of heat generated by cement hydration per unit volume of concrete [W/m <sup>3</sup> ].

Initial and boundary conditions may be expressed as follows:

$$T(x_i, t = 0) = T_p(x_i, 0) \quad (3)$$

$$c(x_i, t = 0) = c_p(x_i, 0) \quad (4)$$

$$\mathbf{n}^T (\alpha_{TT} \text{grad } T + \alpha_{TW} \text{grad } c) + \tilde{q} = 0 \quad (5)$$

$$\mathbf{n}^T (\alpha_{WW} \text{grad } c + \alpha_{WT} \text{grad } T) + \tilde{\eta} = 0 \quad (6)$$

where  $x_i \in (V \cup \partial V)$ ,  $i = x, y, z$ ,  $T_p$ ,  $c_p$  are the initial distribution of temperature and the initial concentration of moisture, respectively,  $\mathbf{n} = [n_x, n_y, n_z]^T$  is a vector normal to the boundary surface  $\partial V$ .

The heat flux  $\tilde{q}$  depends on the temperature of the boundary surface  $\hat{T}(x_i, t)$  and the outer temperature  $T_z(t)$ . Similarly, the moisture flux  $\tilde{\eta}$  depends on the moisture content at the boundary surface  $\hat{c}(x_i, t)$  and on the moisture content in the surrounding air. Hence, it can be written:

$$\tilde{q} = \frac{\alpha_p}{c_b \rho} [\hat{T}(x_i, t) - T_z(t)] \quad (7)$$

$$\tilde{\eta} = \beta_p [\hat{c}(x_i, t) - c_z(t)] \quad (8)$$

where  $\alpha_p$  denotes the thermal transfer coefficient, W/(m<sup>2</sup>K),  $\beta_p$  is the moisture transfer coefficient, m/s and  $c_z$  can be calculated from the formula:

$$c_z = \frac{W_z \rho_w}{\rho} \quad (9)$$

with  $W_z = 0.0005\varphi$ , m<sup>3</sup>/m<sup>3</sup>, and  $\rho_w = m_w / V_w$ , where:

$\varphi$  – relative humidity [%],

$m_w$  – mass of water in concrete [kg],

$V_w$  – volume of water in concrete [m<sup>3</sup>].

Taking into account the amount of cement  $c_c$  in 1 m<sup>3</sup> of concrete mix, the rate of heat generated per unit volume of concrete can be determined as:

$$q_v(T, t) = c_c q(T, t) \quad (10)$$

The rate of heat generated per unit volume of cement can be written as follows:

$$q(T, t) = \frac{\partial Q(T, t)}{\partial t} \quad (11)$$

In the presented model, heat of hydration was described by the equation:

$$Q(T, t) = Q_\infty e^{-at_e^{-0.5}} \quad (12)$$

where  $a$  is the coefficient connected with the type of cement given by the function  $a = a_1 t_e^{a_2}$  ( $a_1$  and  $a_2$  depend on the type of cement) and  $t_e$  is the equivalent age of concrete that is given by the equation:

$$t_e = \int_0^t e^{-\frac{E_K}{R} \left( \frac{1}{T} - \frac{1}{T_0} \right)} dt \quad (13)$$

### 3.2. Thermal–shrinkage strains

Imposed thermal–shrinkage strains  $\varepsilon^n$  are treated as volumetric strains:

$$d\boldsymbol{\varepsilon}^n = \begin{bmatrix} d\varepsilon_x^n & d\varepsilon_y^n & d\varepsilon_z^n & 0 & 0 & 0 \end{bmatrix} \quad (14)$$

and calculated based on predetermined temperature and humidity according to the equation:

$$d\varepsilon_x^n = d\varepsilon_y^n = d\varepsilon_z^n = \alpha_T dT + \alpha_W dW \quad (15)$$

where:

- $\alpha_T$  – the coefficient of thermal deformability,
- $\alpha_W$  – the coefficient of moisture deformability.

Equation 15 has a simplified character, because it assumes a linear relationship between temperature and moisture change in hardening concrete and strains. Although some authors suggest a non-linear relationship, especially in description of shrinkage strains based on moisture change, the relationship in Equation 15 is most frequently used in modelling of the phenomena being considered. The relation between mass concentration  $c$  (kg/kg) and volumetric moisture  $W$  (m<sup>3</sup>/m<sup>3</sup>) can be expressed analogically to equation (9).

### 3.3. Stress analysis

In the model, the viscoelastic and viscoelasto–viscoplastic areas were distinguished. These two areas are separated by the initial location of the yield surface, the formula of which is defined by the boundary surface multiplied by the coefficient less than one. The coefficient can be classified as the viscoelasticity limit. Its value depends on the concrete strength in uniaxial compression, as in the equation:

$$e_{\text{lim}} = 1 - e^{-0.02f_c(t_e)} \quad (17)$$

The following constitutive equation was assumed in the viscoelastic area:

$$\dot{\boldsymbol{\sigma}} = \mathbf{D}^{\text{ve}} (\dot{\boldsymbol{\varepsilon}} - \dot{\boldsymbol{\varepsilon}}^n - \dot{\boldsymbol{\varepsilon}}^c) \quad (18)$$

where:

$$\dot{\boldsymbol{\sigma}} = \frac{d\boldsymbol{\sigma}}{dt}, \quad \dot{\boldsymbol{\varepsilon}} = \frac{d\boldsymbol{\varepsilon}}{dt}, \quad \dot{\boldsymbol{\varepsilon}}^n = \frac{d\boldsymbol{\varepsilon}^n}{dt}, \quad \dot{\boldsymbol{\varepsilon}}^c = \frac{d\boldsymbol{\varepsilon}^c}{dt} \quad (19)$$

Viscoelasticity matrix  $\mathbf{D}^{\text{ve}}(t_{i+1})$  is given by the formula:

$$\mathbf{D}^{\text{ve}}(t_{i+1}) = \frac{\mathbf{D}^e(t_{i+1})}{1 + 0.5E(t_{i+1}) \left[ \frac{1}{E(t_i)} - \frac{1}{E(t_{i+1})} + H(t_{i+1}, t_i) \right]} \quad (20)$$

and additional denotations  $\Delta \boldsymbol{\varepsilon}^c(t_{i+1})$  and  $H(t_{i+1}, t_i)$  are given by the formulas:

$$\Delta \boldsymbol{\varepsilon}^c(t_{i+1}) = \mathbf{D}^{-1} \left[ \int_0^{t_i} -\frac{\partial C(t_{i+1}, \tau)}{\partial \tau} \boldsymbol{\sigma}(\tau) d\tau + \boldsymbol{\sigma}(t_i) \int_{t_i}^{t_{i+1}} -\frac{\partial C(t_{i+1}, \tau)}{\partial \tau} d\tau - \int_0^{t_i} -\frac{\partial C(t_i, \tau)}{\partial \tau} \boldsymbol{\sigma}(\tau) d\tau \right] \quad (21)$$

$$H(t_{i+1}, t_i) = \int_{t_i}^{t_{i+1}} -\frac{\partial C(t_{i+1}, \tau)}{\partial \tau} d\tau \quad (22)$$

A creep function  $C(t, \tau)$  and a function describing the modulus of elasticity variation during concrete curing  $E(t)$  were assumed according to functions suggested by CEB FIP MC90 [17].

In the viscoelasto–viscoplastic area, the constitutive equation has a form:

$$\dot{\boldsymbol{\sigma}} = \mathbf{D}^{ve} (\dot{\boldsymbol{\varepsilon}} - \dot{\boldsymbol{\varepsilon}}^n - \dot{\boldsymbol{\varepsilon}}^c - \dot{\boldsymbol{\varepsilon}}^{vp}) \quad (23)$$

where:

$$\dot{\boldsymbol{\varepsilon}}^{vp} = \dot{\lambda} \frac{\partial f}{\partial \boldsymbol{\sigma}} \quad (24)$$

In the consistent concept of the viscoplastic strains description, both the yield surface  $f$  and the failure surface  $F$  are rate-dependent surfaces:

$$f(\boldsymbol{\sigma}, \boldsymbol{\kappa}, \dot{\boldsymbol{\kappa}}) = 0 \quad (25)$$

$$F(\boldsymbol{\sigma}, \boldsymbol{\kappa}, \dot{\boldsymbol{\kappa}}) = 0 \quad (26)$$

The failure surface can be described as a modified 3-parameter Willam–Warnke failure criterion [15, 16, 18]. The failure criterion involves all stress invariants in the form of non-dimensional values of the octahedral stress  $s_m = \sigma_m / f_c(t_e)$ ,  $t_0 = \tau_{okl} / f_c(t_e)$  and the angle of similarity  $\theta$ . The failure surface for young concrete was assumed as a fixed surface in the proposed coordinate system. The meridians are straight lines and in the low-compression and tension regime, the caps described as the second-order parabolas were introduced. In the deviatoric plane, the failure surface in both models has a noncircular cross-section, described according to the Willam–Warnke conception as a part of an elliptic curve (Fig. 1).

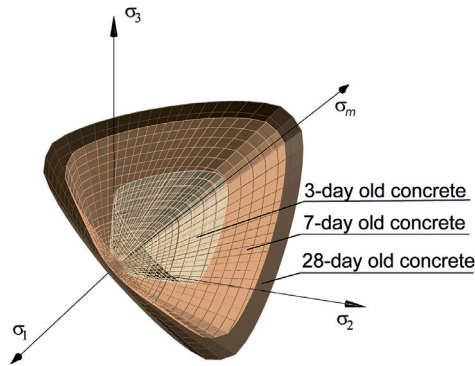


Fig. 1. Development of the failure surface of young concrete in the maturing process

A smeared crack image was assumed in the model. The possibility of crack occurrence is defined based on the location of the point representing a stress state with respect to the failure surface. This location can be described by the formula:

$$s_l = \frac{\tau_{okt}}{\tau_{okt}^f} \tag{27}$$

where:

$s_l$  – referred to as the damage intensity factor.

The damage intensity factor equal to 1 is equivalent to the stress reaching the failure surface and signifies failure of the element. Character of this failure depends on the location where the failure surface is reached [15–16]. In the further presented examples, reaching of the failure surface always occurred within the range of the hydrostatic tensile stresses which is equivalent to formation of the crack in the plane perpendicular to the direction of the maximum principal stress.

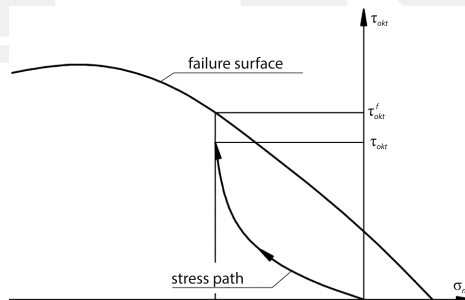


Fig. 2. Axiatoric section of failure surface

### 3.4. Reinforcement

Reinforcement is modelled as bar elements connected with concrete elements in the nodes. Bond forces between reinforcement and adjoining concrete are not considered, so the assumed model is simplified. Elastic–perfectly-plastic material model with Huber–von Mises–Hencky failure surface is assumed for reinforcement.

### 3.5. Validation of the model

Validation of the numerical results with experimentally-obtained data is necessary to confirm reliability of the theoretical model. Because the proposed model includes two issues connected with determination of thermal–moisture fields and stress and strain states, validation of the model should be two-phase. It should be noted that this is an untypical task in which firstly the loads to which the structure is subjected (thermal–moisture fields) are validated, and then the effects of these loads – stress state – is validated. This results from a specific nature of massive concrete structures where the material of the structure itself is the source of the load.

Validation of the model is presented in [15]. In the validation of thermal–moisture fields, the authors' own experimental results were used. In the case of stress state, because of the assumed complex material model, validation was initially performed with simple numerical tests, which allowed for qualitative confirmation of the proposed material model correctness. Firstly, creep test simulation in heavily stressed conditions was performed. Then, the results of numerical simulations of simple stress states in concrete samples were presented, i.e. uniaxially compressed and tensiled samples and cylindrical samples in split test. In the second phase, the thermal–shrinkage stresses were analysed. The results of the authors' own, as well as other experiments were used.

## 4. Analysis of RC wall

### 4.1. Input data

The analysed wall was assumed to have 20 m of length, 4 m of height and 80 cm of thickness, supported on a 4 m wide and 70 cm deep strip foundation of the same length. The wall and the foundation were assumed to be reinforced with a near-surface reinforcing net of  $\varnothing 16$  bars. The wall was reinforced at both surfaces with horizontal spacing of 20 cm and vertical spacing of 15 cm. The foundation was reinforced with a 20 cm  $\times$  20 cm mesh at the top and bottom surface.

Due to the fact that the wall has two axes of symmetry, the model for finite element analysis was created for  $\frac{1}{4}$  of the wall. A uniform mesh was prepared and densified at the free edges of the wall and within the contact surface between the wall and the foundation. The final geometry of the wall with a mesh of finite elements is presented in Fig. 3.

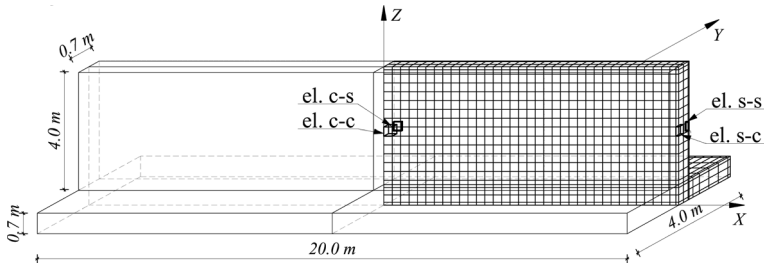


Fig. 3. Dimensions of the wall with finite element mesh

Mechanical properties of mature concrete were taken as follows: the compressive strength  $f_{cm} = 35$  MPa, the tensile strength  $f_{ctm} = 3$  MPa and the modulus of elasticity  $E_{cm} = 32$  GPa, and steel class RB400 were assumed for both the wall and the foundation. The foundation was erected earlier and had hardened, so the material properties were assumed as for 28-day concrete. For the wall, development of material properties was assumed according to CEB-FIP MC90. Detailed material properties, environmental and technological conditions were taken as:

- cement type CEM I 42.5R, 375 kg/m<sup>3</sup>,
- concreting proceeded in summer – ambient temperature  $T_z = 25^\circ\text{C}$ ,
- initial temperature of fresh concrete mixture  $T_p = T_z = 25^\circ\text{C}$ ,
- wooden formwork of 1.8cm plywood; no insulation,
- protection of top surface with foil,
- formwork removed in 3 days (72 h) after concrete casting.

The values of parameters taken in numerical analysis are presented in Table 1.

Table 1

## Parameters assumed for numerical analysis

Thermal fields		Moisture fields	
$\Lambda$ [W/(mK)]	2.56	$q_v$ [W/m <sup>3</sup> ]	acc. to eq. (10)*
$c_b$ [kJ/(kgK)]	0.82		
$\rho$ [kg/m <sup>3</sup> ]	2413	$K$ [m <sup>3</sup> /J]	$0.3 \cdot 10^{-9}$
$\alpha_p$ [m <sup>2</sup> /s]	$12.94 \cdot 10^{-7}$	$\alpha_{ww}$ [m <sup>2</sup> /s]	$0.6 \cdot 10^{-9}$
$\alpha_{TW}$ [m <sup>2</sup> K/s]	$9.375 \cdot 10^{-5}$	$\alpha_{wT}$ [m <sup>2</sup> /sK]	$2 \cdot 10^{-11}$
$\alpha_p$ [W/(m <sup>2</sup> K)]	15.00 no covering 13.78 foil 5.58 formwork	$\beta_p$ [m/s]	$2.78 \cdot 10^{-8}$ no covering $0.10 \cdot 10^{-8}$ foil $0.18 \cdot 10^{-8}$ formwork

\* data from tests for cement CEM I 42.5R:  $Q_\infty = 508$  kJ/kg,  $a_1 = 513.62$  and  $a_2 = -0.17$

The foundation was assumed to have cooled down by the moment of wall casting, thus the initial temperature of the foundation concrete was taken as equal to the ambient temperature  $T_z$ . The parameters connected with temperature and moisture migration in the wall after formwork removal were assumed as for a free, unprotected surface.

#### 4.2. Thermal and moisture analysis

The thermal–moisture effects were analyzed in time steps for the first 20 days (480 h) after casting of fresh concrete. Calculations were performed with TEMWIL program.

Fig. 4 shows the map of temperature distribution while Fig. 5 shows the map of moisture content distribution in the wall after 26 hours, when the maximum values of temperature were observed. It can be noticed that the concentration of high temperatures occurred in the central part of the wall while the edges were cooler because of the heat dissipation. Accompanying heating of the foundation was observed. It should be emphasised that there was little temperature difference at the thickness of the wall (not more than  $\sim 6^\circ\text{C}$ ). Water content in the whole body of the wall was on a similar level; some moisture concentrated near the surfaces where the wall was protected with the formwork/foil.

A change of temperature and moisture content in time was examined for four finite elements to represent the behaviour of the interior and the surface of the wall in the central part and at the edge of the structure (the elements are marked in Fig. 3). The results are collectively presented in Fig. 6–7 for temperature and moisture content, respectively.

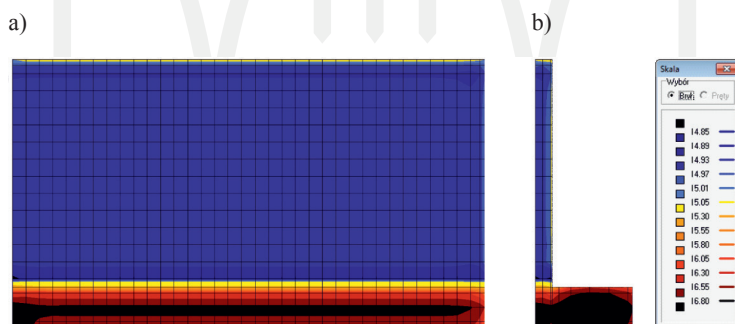


Fig. 4. Temperature distribution [ $^\circ\text{C}$ ] after 26 hours: a)  $XZ = 0$ , b)  $YZ = 0$

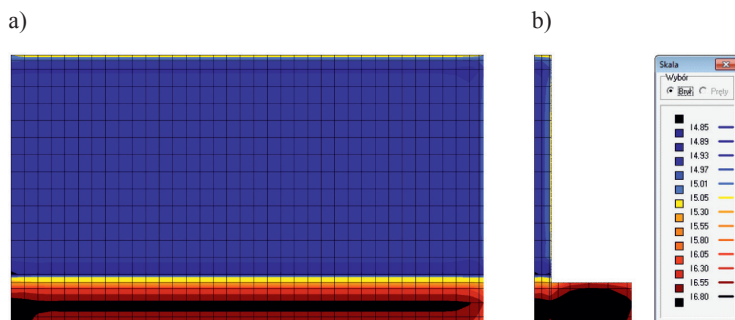


Fig. 5. Moisture content distribution [ $\times 100, \text{m}^3/\text{m}^3$ ] after 26 hours: a)  $XZ = 0$ , b)  $YZ = 0$

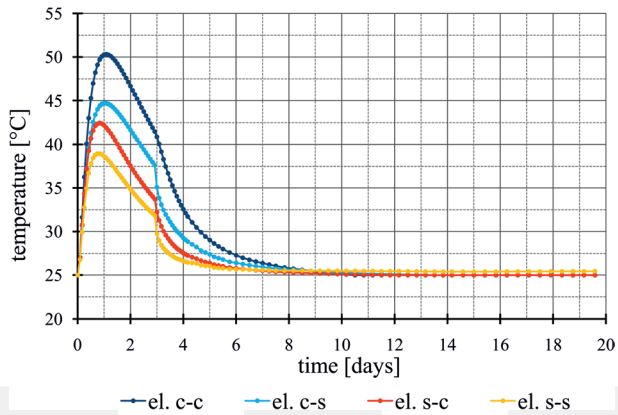


Fig. 6. Temperature evolution in time

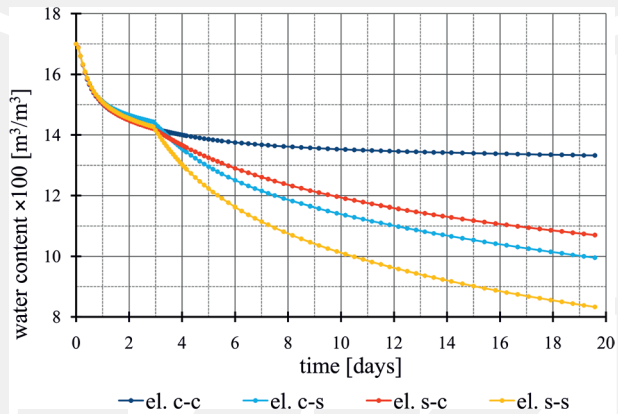


Fig. 7. Moisture loss in time

The greatest temperatures were reached in the central part of the wall, with maximum values obtained in the interior (el. c-c, 50.3°C) and bit smaller on the surface (el. c-s, 44.7°C). The lowest values were observed near the edge of the wall, with greater values inside the wall (el. s-c, 42.5°C) and smaller values near the surface (el. s-s, 38.9°C). The moment of formwork removal was visible, especially on the surface.

A similar pattern was also observed in the moisture migration diagram. The effect of the formwork removal was very visible: there was hardly any difference in the migration rate for different areas of the wall while the element was in the formwork, but the alteration was observed after the formwork was removed. As was expected, the rate of the drying process was decelerating as the accessibility to the surface decreased, being the fastest in the parts of the wall near two free surfaces (el. s-s), medium near one surface (el. s-c and c-s), and the slowest in the interior of the wall (el. c-c).

### 4.3. Stress analysis

Determination of the thermal–moisture fields allowed for the indication of the stress state and the level of damage intensity within the wall. Calculations were proceeded with MAFEM\_V EVP program. The results were analysed with use of MAFEM3D interface. Figure 8 shows the change of  $\sigma_x$  stress in time.

Two distinct phases in the behaviour of the wall during concrete curing can be distinguished. The first phase was caused by thermal expansion of the wall due to increase of temperature. Because of the bond between the (cool) foundation and the (hot) wall, compressive stresses were induced in almost the whole wall. A map of stresses at expansion after 16 hours is presented in Fig. 9a. Deformation of the structure is presented in 500:1 scale with respect to dimensions of the structure. The second phase was connected with cooling of the concrete accompanied with extensive drying shrinkage occurring after formwork removal. This led to contraction of the wall and tensile stresses appearing in the wall. Fig. 9b presents a map of stresses after 6 days. The concrete of the wall is vulnerable to cracking if tensile stresses reach the level exceeding the tensile strength of concrete. A sudden drop of stress in the surface element in the diagram in Fig. 8 signifies that tensile strength was reached and a crack occurred in the element.

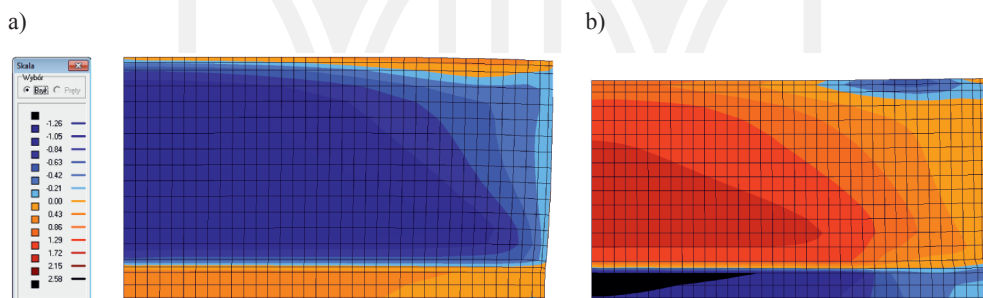


Fig. 9.  $\sigma_x$  stress distribution in  $XZ = 0$  cross-section: a) heating phase, b) cooling phase

### 4.4. Parametric study of thermal–shrinkage cracking

The presented numerical model allows for a multi-parameter investigation of thermal–moisture effects in the early-age concrete. The influence of the factors connected with the geometry of the wall, environmental conditions as well as conditions of concreting and curing of concrete on the resultant thermal–shrinkage cracking can be analysed.

This paper presents the results of the investigation into the influence of the conditions of concrete casting and curing on cracking. The implemented smeared model of cracks means that cracking is not represented as single cracks but by means of the damage intensity factor diagrams, so the comparison of the results of the numerical simulation is based on the damage intensity maps. It was stated that in all the analysed cases, the failure surface was reached within the range of hydrostatic tensile stresses, thus each time the ultimate damage intensity factor was equal to 1 in the finite element, it was equivalent to formation of the crack within this element. Hence, the black areas in the damage intensity factor diagram represent the possible location of the cracks. The scale for damage intensity applies to all the maps.

Fig. 10 shows the damage intensity maps for the basic case after 19 days. A typical cracking pattern can be observed: vertical cracks occur within the wall with the biggest cracks concentrating in the midspan and decreasing towards the free edge of the wall. It should be noticed that due to the early formwork removal, the surface of the wall is more prone to rapid cooling and drying, hence cracking would be observed at the surface first and would be of greater magnitude in the near-surface areas.

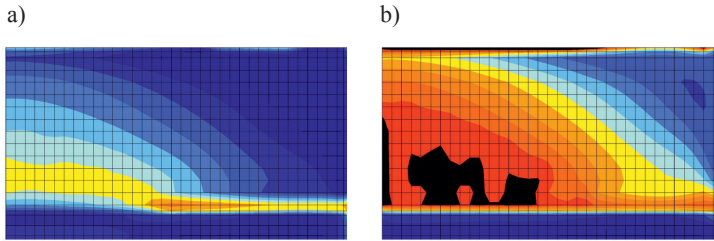


Fig. 10. Damage intensity of the wall in 19 days: a)  $XZ = 0$ , b)  $XZ = 0.4$  m

#### 4.4.1. Influence of ambient temperature and temperature difference

In the basic case, it was assumed that the concrete casting of the wall was proceeded during summer with no pre-cooling of the concrete mix. The second analysed example was a case of concreting in spring with the assumed ambient temperature of  $15^{\circ}\text{C}$ . The map of the damage intensity for that case after 19 days is presented in Fig. 11. It can be noticed that the character of damage intensity development is similar but the intensity is a bit lower.

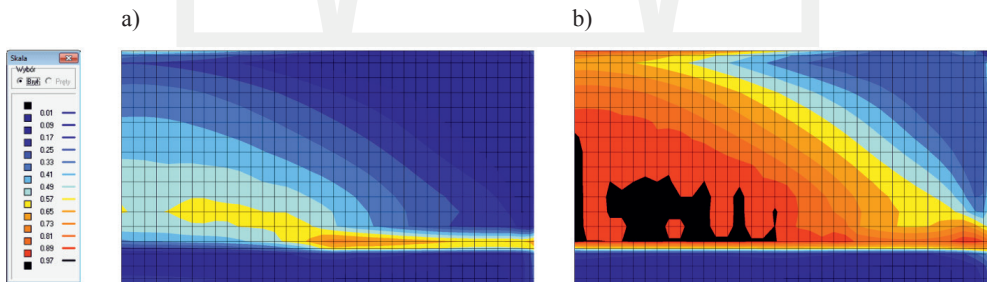


Fig. 11. Damage intensity of the wall in 19 days ( $T_p = T_z = 15^{\circ}\text{C}$ ): a)  $XZ = 0$ , b)  $XZ = 0.4$  m

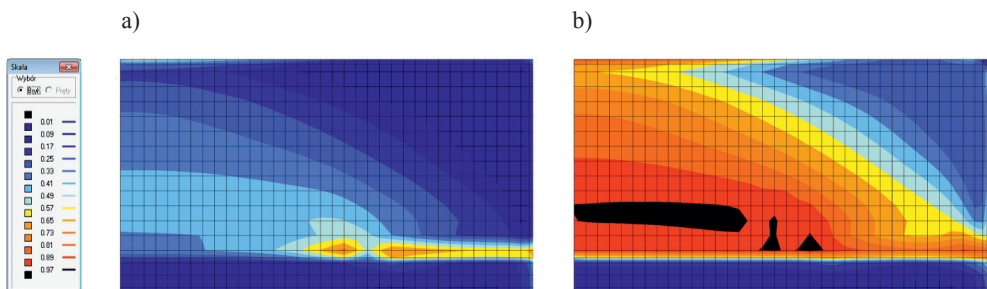


Fig. 12. Damage intensity of the wall in 19 days ( $T_z = 25^{\circ}\text{C}$ ,  $T_p = 20^{\circ}\text{C}$ ): a)  $XZ = 0$ , b)  $XZ = 0.4$  m

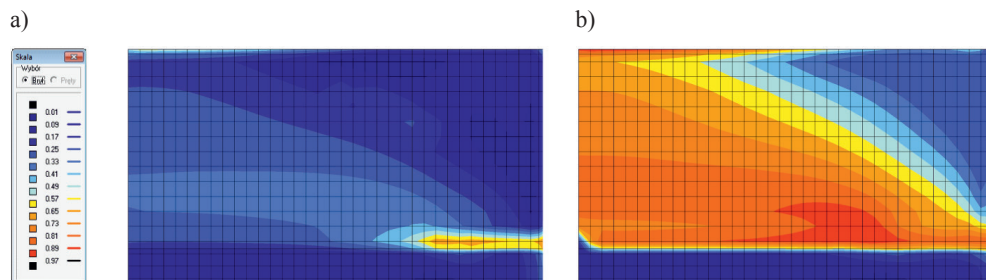


Fig. 13. Damage intensity of the wall in 19 days ( $T_z = 25^\circ\text{C}$ ,  $T_p = 15^\circ\text{C}$ ): a)  $XZ = 0$ , b)  $XZ = 0.4$  m

In two other cases, the concrete casting was assumed to be proceeded in summer ( $T_z = 25^\circ\text{C}$ ) but with the concrete mix cooled by 5 and  $10^\circ\text{C}$  ( $T_p = 20$  and  $15^\circ\text{C}$ ). The maximum observed temperature in the wall was reduced to  $45.9$  and  $41.8^\circ\text{C}$ , respectively. Fig. 12–13 present the maps of damage intensity after 20 days. A limitation of cracking was achieved – when initial cooling by  $10^\circ\text{C}$  was applied, cracking risk was completely eliminated.

The comparison was made between the basic case and the analysed cases for the temperature, moisture and stress changes over time. The two finite elements were analysed: one in the interior of the wall, and the second at the surface – both in the mid-span cross-section of the wall. The results are collectively presented in Fig. 14–16. The basic case is denoted as “basic” while the temperature cases  $T_z = T_p = 15^\circ\text{C}$  as “mod1”,  $T_z = 25^\circ\text{C}$  and  $T_p = 20^\circ\text{C}$  as “mod2” and  $T_z = 25^\circ\text{C}$  and  $T_p = 15^\circ\text{C}$  as “mod3”, respectively.

It was observed that the initial temperature of young concrete and ambient temperature had an influence upon the maximum temperature and heat migration rate during hardening process. The highest temperatures were reached when both the initial temperature of the concrete and the external temperature were high, lower when initial cooling of the concrete mix was applied and the lowest when the two were on the same, low level. In all cases, the maximum temperature was reached after almost the same time, but there was an impact on the cooling rate: cooling was finished at the same time, so it proceeded faster in the walls in which concrete was initially warmer. The process was more moderate in the near-surface parts than in the interior of the wall. There was a negligibly small influence of the temperature difference on the moisture dissipation process. Two general characteristics were observed: the first, smooth, characterising internal parts and the second, with a visible drop, in the surface parts.

In the stress–time relationship, the difference between the internal and surface areas was also noticed: compressive stresses were lower near the surface but the peak tensile stress was observed earlier. Lowering of the initial concrete temperature allowed more moderate stress change of the smaller magnitude in tension to be obtained, especially if achieved by initial cooling of concrete. Pre-cooling of concrete mix allowed for the elimination of cracking. Concreting at a lower temperature allowed for the lowering of the values of stresses, but at the same time a lower temperature resulted in a slower rate of strength development. This explains a similar level of damage intensity of the wall executed in  $T_z = T_p = 15^\circ\text{C}$  conditions.

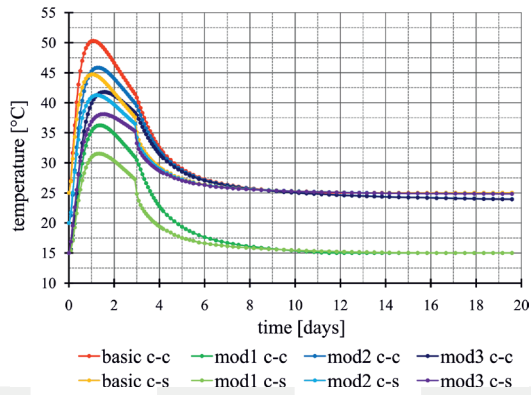


Fig. 14. Temperature development over time – influence of concreting conditions

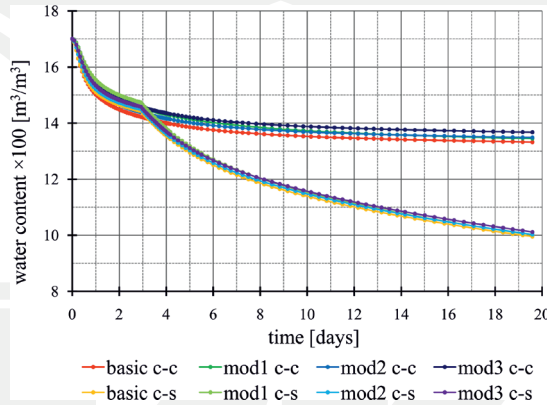


Fig. 15. Moisture loss over time – influence of concreting conditions

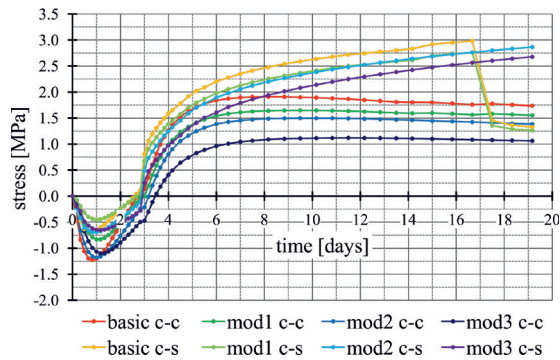


Fig. 16. Stress development over time – influence of concreting conditions

#### 4.4.2. Influence of time of formwork removal

Formwork removal after 3 days was assumed in the basic case. However, it was proved that at this moment, young concrete has still very high temperature and is subjected to high thermal strains. Therefore, it was investigated how the later formwork removal would influence the cracking of the wall.

The first scenario was analysed in which the formwork was removed after 10 days. The results presented in Fig. 17 show that this is not beneficial for the wall. The level of damage intensity was comparable to the basic case. Another scenario assumed that the wall was in the formwork during the whole process of curing. The removal was assumed after 28 days, so when the concrete had definitely cooled down. The maps in Fig. 18 show that significant limitation of cracking was obtained. What is important is that the application of the formwork during the whole curing process prevented the surface of the wall from rapidly drying and heat dissipation was limited. Hence, higher stresses occurred in the interior of the wall.

A collective comparison was made to assess the influence of different times of the formwork removal. The results are presented in Fig. 19 for temperatures, Fig. 20 for moisture and Fig. 21 for stresses. The case when formwork was removed after 10 days was denoted as “mod4” and when the wall was detained in formwork for 28 days as “mod5”.

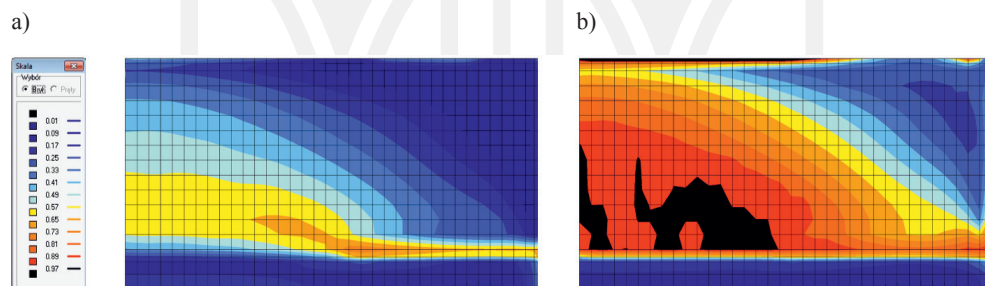


Fig. 17. Damage intensity of the wall in 19 days (formwork removed after 10 days): a)  $XZ = 0$ , b)  $XZ = 0.4$  m

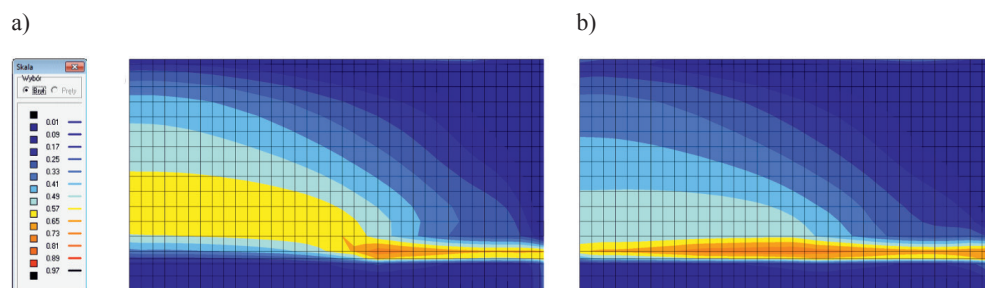


Fig. 18. Damage intensity of the wall in 19 days (the wall detained in formwork): a)  $XZ = 0$ , b)  $XZ = 0.4$  m

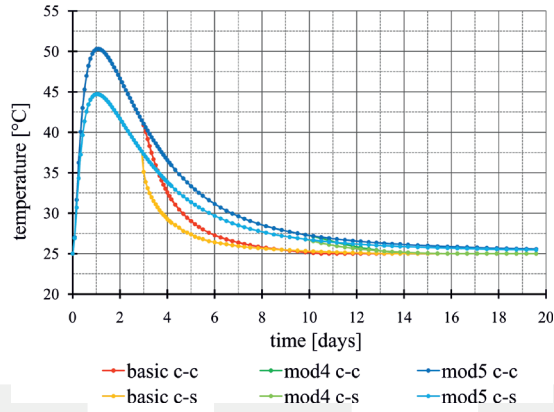


Fig. 19. Temperature development over time – influence of formwork removal time

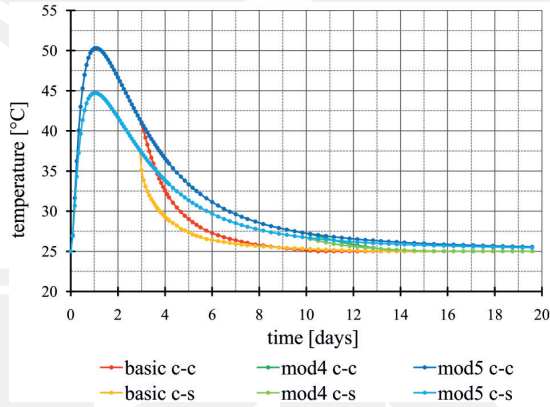


Fig. 20. Moisture loss over time – influence of formwork removal time

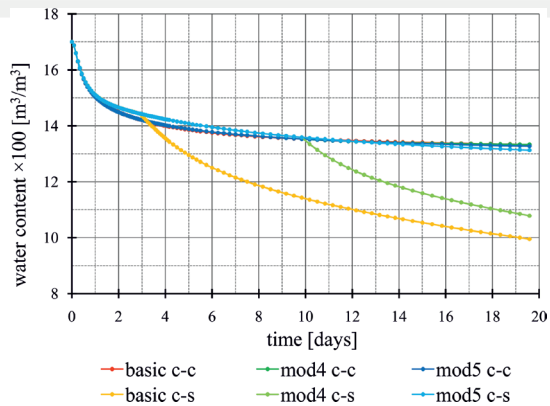


Fig. 21. Stress development over time – influence of formwork removal time

The time of the formwork removal had an influence on the rate of cooling and moisture migration after the removal. The most significant effects were observed when the formwork was removed early and the process attenuated when the formwork was detained for a longer time. A uniform temperature change was observed when the formwork was not removed until the concrete had cooled down.

The rate and magnitude of the water removal was almost the same both for the internal and surface parts unless the formwork was removed, this triggered extensive dehydration of the near-surface areas.

The stress development was identical when the wall was in the formwork. After the formwork removal, when the concrete of the wall started to shrink, the value of the peak tensile stress was greater and occurred earlier in the walls where the formwork was removed early; this led to surface cracking. What was very interesting, for the wall which was detained in the formwork for the whole curing process, was that the tensile stress curve was very smooth and the greatest stresses were observed in the interior of the wall. This had the result of no possibility of exchange of heat and moisture with the surrounding.

## 5. Conclusions

The presented paper deals with the numerical modelling of thermal–moisture effects in hardening concrete on the example of a reinforced concrete wall cast against an old set foundation. The results obtained in the numerical analyses conform to the present knowledge and practical experience. Because of a complex nature of a multi-phenomena process of concrete hardening numerical analyses are particularly difficult. The results can be regarded as qualitatively and quantitatively correct because the model was validated with experimental data. This confirms that the proposed numerical model of thermal–moisture effects in young concrete describes correctly the analysed case. In conclusion, the contribution of the presented work to this field of activity is the development and adaptation of a complex numerical model of thermal–moisture effects in hardening concrete and its implementation.

*This paper was done as part of a research project N N506 043440 funded by Polish National Science Centre.*

## References

- [1] Ayotte E., Massicotte B., Houde J., Gocovski V., *Modeling the thermal stresses at early ages in a concrete monolith*, ACI Materials Journal, vol. 94 issue 6, 1997.
- [2] Bažant Z. P., Carol I., *Viscoelasticity with aging caused by solidification of nonaging constituent*, Journal of Engineering Mechanics, no. 119, 1993.
- [3] Borucka-Lipska J., Kiernożycki W., Freidenberg P., *Indirect interactions in massive concrete elements with different concrete compositions*, Przegląd Budowlany, nr 3, 2006.
- [4] Di Luzio G., Cedolin L., *Numerical model for time-dependent fracturing of concrete structures and its application*, Proceedings of International Conference on Fracture Mechanics of Concrete and Concrete Structures, Catania, Italy 2007.

- [5] Santurjian O., Kolarow L., *A spatial FEM model of thermal stress state of concrete blocks with creep consideration*, Computers and Structures, vol. 58 issue 3, 1996.
- [6] Yuan Y., Wan Z.L., *Prediction of cracking within early-age concrete due to thermal, drying and creep behavior*, Cement and Concrete Research, no. 32, 2002.
- [7] Gawin D., Pesavento F., Schrefler B. A., *Hygro-thermo-chemo-mechanical modelling of concrete at early ages and beyond. Part I: Hydration and hygro-thermal phenomena*, International Journal for Numerical Methods in Engineering, no. 67, 2006.
- [8] Gawin D., Pesavento F., Schrefler B.A., *Hygro-thermo-chemo-mechanical modelling of concrete at early ages and beyond. Part II: Shrinkage and creep of concrete*, International Journal for Numerical Methods in Engineering, no. 67, 2006.
- [9] Wyrzykowski M., *Modeling coupled thermo-hygral process in maturing concrete exposed to internal and external curing*, PhD thesis, Technical University of Łódź, Łódź 2010.
- [10] Andreasik M., *Thermal-shrinkage stresses in massive concrete*, PhD thesis, Cracow Technical University, Kraków 1982.
- [11] Szarliński J., *Stress state and limit loads of massive concrete structures*, Monograph 88, Kraków 1989.
- [12] Klemczak B., *Viscoelastic-plastic material model for numerical simulation of phenomena occurring in early age concrete*, PhD thesis, Silesian University of Technology, Gliwice 1999.
- [13] Meschke G., *Consideration of aging of shotcrete in the context of 3-D viscoplastic material model*, International Journal for Numerical Methods in Engineering no. 39, 1996.
- [14] Tanabe T., Ishikawa Y., Ando N., *Visco-elastic and visco-plastic modeling of transient concrete*, Proceedings of EURO-C 1998 International Conference on Computational Modelling of Concrete Structures, Badgastein, Austria 1998.
- [15] Klemczak B., *Modeling thermal-moisture and mechanical effects in massive concrete structures*, Monograph 183, Silesian University of Technology, Gliwice 2008.
- [16] Klemczak B., *Prediction of Coupled Heat and Moisture Transfer in Early-Age Massive Concrete Structures*, Numerical Heat Transfer. Part A: Applications, vol. 60, no. 3, 2011.
- [17] *CEB-FIP Model Code 1990*, 1991.
- [18] Klemczak B. *Adapting of the Willam-Warnke failure criteria for young concrete*, Archives of Civil Engineering, vol. 53, no. 2, 2007.

ROBERT KOWALSKI, MAREK URBAŃSKI\*

## REDISTRIBUTION OF BENDING MOMENTS IN MULTI – SPAN R/C BEAMS AND SLABS SUBJECTED TO FIRE

### REDYSTRYBUCJA MOMENTÓW ZGINAJĄCYCH W WIELOPRZĘSŁOWYCH BELKACH I PŁYTACH ŻELBETOWYCH W WARUNKACH POŻAROWYCH

#### Abstract

This paper shows consideration of decrease in cross-section stiffness in commonly used in practice R/C beams and slabs in cases when only reinforcing bars or only concrete compressed zone is subjected to fire. Analyses were based on: a) standard fire curve, b) 500°C Isotherm Method assumptions, c) mechanical properties of reinforcing steel when heated to high temperatures. Afterwards, based on the estimated decrease of cross-sections stiffness, the redistribution of bending moments was calculated in some cases of two-span R/C beams and slabs subjected to fire from their bottom face. Due to the bending moment redistribution, one could expect a reduction of bending moments in span cross-sections and an increase of the support bending moment. As a result of this phenomenon, the ultimate limit state of the structural multi-span elements might occur after a shorter fire duration than could be expected when redistribution of bending moments is neglected.

*Keywords: concrete, cross-section, fire design, stiffness*

#### Streszczenie

W artykule rozważono zmniejszenie sztywności powszechnie stosowanych przekrojów belek i płyt żelbetowych w przypadkach, gdy tylko strefa prętów zbrojenia lub tylko strefa ściskana betonu wystawiona jest na działanie pożaru. Analizy oparto na: a) standardowej krzywej pożaru, b) założeniach metody izotermii 500°C [10], c) właściwościach mechanicznych stali zbrojeniowej w wysokiej temperaturze. Następnie, na podstawie oszacowania spadku sztywności przekrojów, obliczono redystrybucję momentów zginających w niektórych przypadkach dwuprzęsłowych belek i płyt żelbetowych, ogarniętych od spodu pożarem. Ze względu na redystrybucję momentów zginających można spodziewać się ich zmniejszenia w przekrojach przęsłowych oraz zwiększenia w przekrojach podporowych. W efekcie stan graniczny nośności wieloprzęsłowych elementów konstrukcyjnych może być osiągnięty po krótszym czasie trwania pożaru niż można byłoby się tego spodziewać w przypadku nieuwzględnienia redystrybucji momentów zginających.

*Słowa kluczowe: beton, przekrój, projektowanie z uwagi na warunki pożarowe, sztywność*

\* Prof. Robert Kowalski, Marek Urbański, The Faculty of Civil Engineering, Warsaw University of Technology.

## Symbols

$A_s$	– area of reinforcement [m]
$B_I$	– stiffness is determined on the assumption that the cross-section is not cracked [kNm <sup>2</sup> ]
$B_{II}$	– stiffness is determined on the assumption that the cross-section is fully cracked [kNm <sup>2</sup> ]
$B_{fi}$	– stiffness of a section in fire condition [kNm <sup>2</sup> ]
$E_{c,eff}$	– modulus of elasticity of concrete [GPa]
$E_s$	– modulus of elasticity of steel [GPa]
$E_{s,fi}$	– modulus of elasticity of steel in fire condition [GPa]
$a$	– axis distance of reinforcement [cm]
$b$	– breadth of beam [m]
$f_{yk}$	– characteristic value of tension yield stress of steel [MPa]
$f_{yk,0}$	– characteristic value of tension yield stress of steel in fire condition [MPa]
$g_k$	– characteristic permanent load [kN/m <sup>2</sup> ]
$h$	– total height of a section [m]
$l$	– span; length of an element [m]
$q_k$	– characteristic variable load [kN/m <sup>2</sup> ]
$t$	– time, duration [min]
$\alpha$	– angle [rad]
$\gamma_{G,sup}$	– partial safety factor for permanent [loads]
$\gamma_Q$	– partial coefficient for the variable effects
$\varepsilon_{s,tot}$	– total elongation of reinforcement [%]
$\zeta$	– factor related to the impact of tension stiffening
$\eta$	– ratio of bending moment in fire condition against the bending moment in non-fire condition
$\theta_s$	– temperature of reinforcement [°C]
$\xi$	– a reduction factor
$\rho$	– ratio of tension reinforcement ( $= A_s/bd$ ) [%]
$\sigma_s$	– steel stress [MPa]
$\varphi$	– concrete creep coefficient
$\Psi_0$	– the ratio of the value of combining the variable effects
$\Psi_2$	– the ratio of the quasi-permanent value of variable loads

## 1. Introduction

When reinforced concrete elements are exposed to fire, contraction of concrete and elongation of reinforcing bars can be much larger than found at room temperature [1–3]. This results in a significant reduction in cross-section stiffness, leading to high deformations (deflections) of the elements. Sometimes, the large deflection bending elements can be prevented by the formation of a static scheme of secondary structures (e.g. if the bending elements lean against partition walls) [4].

In predicting the fire resistance of roof elements, the worst fire scenario occurs when fire acts from the bottom of the elements. In this case, only reinforcement is heated in the span cross-sections, and in cross-sections of the support, only a compressed zone of concrete.

Relative changes in the stiffness of the support and span cross-sections may result in the redistribution of bending moments under fire conditions.

The study analyzed computationally changes in stiffness encountered in the practice of slabs and reinforced concrete beams cross-sections exposed to fire only on the tensile reinforcement, or only from the compression zone of concrete. Then, using the two span elements, what may be the impact of relative variation of stiffness of the sections to redistribution of bending moments and the projected capacity fire of elements was determined. The impact of fire was considered above the slab/beam, as less profitable situation.

It should also be noted that in case of fires in complex public or industrial buildings, in practice very rarely is the structure exposed to intense heat from all sides. Most parts (elements) are heated only from the zone of compression, or only from the expanded zone. Competent forecasting of changes in the stiffness of individual elements (cross-sections) and the prediction of the appropriate redistribution of internal forces may be crucial during a global analysis of complex reinforced concrete structures under fire conditions.

## 2. Stiffness of cross-section R/C slabs under fire conditions

### 2.1. Assumptions

Four cases of two-span slabs were examined with the span, thickness and reinforcement chosen so that the conditions of the limit state bearing capacity and usability were fulfilled [5–6]. Adopted variable load  $q_k = 5.00 \text{ kN/m}^2$ , which corresponds to the category of use such as C or D [7–8] and a permanent load ( $g_k$ ), which is the sum of the weight of its own slabs and the value of  $1.25 \text{ kN/m}^2$  were assumed. A more unfavorable combination of loads specified by the formulas [7] has been adopted for the calculation of the ultimate limit state (ULS):

$$p = \gamma_{G,sup} \cdot g_k + \gamma_Q \cdot \Psi_0 \cdot q_k \quad (1a)$$

$$p = \xi \cdot \gamma_{G,sup} \cdot g_k + \gamma_Q \cdot q_k \quad (1b)$$

For the calculation of serviceability limit state (deflection), a quasi-permanent combination of loads was assumed according to the formula:

$$P_{qp} = g_k + \Psi_2 \cdot q_k \quad (2)$$

In these formulas:

- $\gamma_{G,sup}$  – partial safety factor for permanent loads;  $\gamma_{G,sup} = 1.35$ ,
- $\gamma_Q$  – the partial coefficient for the effects variable;  $\gamma_Q = 1.50$ ,
- $\Psi_0$  – the ratio of the value of combining the variable effects;  $\Psi_0 = 0.7$ ,
- $\xi$  – a reduction factor;  $\xi = 0.85$ ,
- $\Psi_2$  – the ratio of the quasi-permanent value of variable loads;  $\Psi_2 = 0.6$ .

It is assumed that all slabs are made of C30/37 concrete and reinforced with steel of characteristic yield strength  $f_{yk} = 500$  MPa. The distance from the axis of cross-section bars is 30 mm. Table 1 shows the most important information about the slabs.

It should be noted that the combination of loads determined by the formula (2) is also suitable for the analysis of fire conditions [7, 9–10]. Given in Table 1, the coefficient  $\eta$  is the ratio of bending moment in fire condition against the bending moment adopted to check the ULS.

Stiffness of slab cross-sections in the fire conditions has been determined basing on assumptions of the 500°C-Isotherm Method, recommended in [10] to calculate the bearing capacity of reinforced concrete elements exposed to standard fire [9, 11]. This method assumes that the concrete in the outer part of cross-section, where the temperature exceeds 500°C, is completely destroyed. In the rest, the inside of the section it is assumed that the strength of concrete is the same as at room temperature. The mechanical properties of reinforcement have been accepted depending on its temperature, regardless of whether the bars are located inside or outside the area limited by the position of the 500°C isotherm.

Table 1

Key parameters of considered slabs

Length [m]	Height [cm]	Load [kN/m <sup>2</sup> ]		Span reinforcement			Support reinforcement		
		ULS	SLS	$H = p_{gp}/p$	$A_s$	$\rho$ [%]	$\eta$	$A_s$	$\rho$ [%]
7.20	25	16.13	10.50	0.61	ø10/100	0.36	0.65	ø12/140	0.54
6.00	20	14.69	9.25	0.59	ø10/120	0.38	0.63	ø16/210	0.56
4.80	16	13.54	8.25	0.57	ø10/150	0.40	0.61	ø12/140	0.58
3.60	12	12.39	7.25	0.55	ø8/130	0.42	0.59	ø8/90	0.62

In the case of heating the tension zone (span cross-section) a cross-section of unchanged dimensions was considered, taking into account only the increase in the elongation of the reinforcement. In the case of the compression zone heating, the cross-section of reduced dimensions and unchanged mechanical characteristics of reinforcement has been examined. The following presents the calculation procedure that was used:

## 2.2. The procedure for calculating cross-sectional span stiffness (heated reinforcement)

The first calculation was performed for the beginning of the fire  $t = 0$  min. The data used for the calculation are suitable for the calculated accidental situation of fire:

- bending moment calculated for the load combinations according to the formula (2); Table 1,
- mechanical characteristics of concrete and reinforcing steel,
- concrete creep coefficient of  $\varphi = 2.09 \div 2.30$ ;  $E_{c,eff} = 10.63 \div 9.94$  GPa (not including the impact of high temperatures).

Stiffness of the cross-section was calculated by the formula [5]:

$$B_{fi} = \frac{1}{\frac{1-\xi}{B_I} + \frac{\xi}{B_{II}}} \quad (3)$$

where:

- $B_I$  – stiffness is determined on the assumption that the cross-section is not cracked,
- $B_{II}$  – stiffness is determined on the assumption that the cross-section is fully cracked,
- $\xi$  – is a factor related to the impact of tension stiffening.

In the next step – the calculations for the duration of the fire,  $t = 30$  min.

Reinforcement temperature ( $\theta_s$ ) is estimated on the basis of Figure 1a [12]. They are the guidelines for a simplified prediction of reinforcement temperature and isotherms of 500°C position in cross-sections of R/C slabs. For the duration of the fire,  $t = 30$  min obtained  $\theta_s = 220^\circ\text{C}$ .

Then the total elongation of reinforcement ( $\varepsilon_{s,tot}$ ) has been estimated. In this regard, graphs given in Figure 2 [13] have been used. They represent the stress-strain relationship developed on the basis of [12] of the free thermal elongation of steel.

The vertical axis shows stress in the reinforcement calculated for the previously considered duration of the fire. The horizontal axis represents the full extension of the reinforcement, depending on the temperature. In the case of slabs with spans of 7.2 m, tension in the reinforcement at the beginning of the fire was  $\sigma_s = 280$  MPa, temperature of the reinforcement  $\theta_s = 220^\circ\text{C}$ , and elongation of reinforcement read  $\varepsilon_{s,tot} = 4.18\%$  (in fact, instead of charting, analytical files have been used for their preparation).

Position of 500°C-isotherm:

Duration of of standard fire:

$t = 30$  min. –  $a_{500} = 1.0$  cm

$t = 60$  min. –  $a_{500} = 2.0$  cm

$t = 90$  min. –  $a_{500} = 3.0$  cm

$t = 120$  min. –  $a_{500} = 3.5$  cm

$t = 180$  min. –  $a_{500} = 5.0$  cm

$t = 240$  min. –  $a_{500} = 6.0$  cm

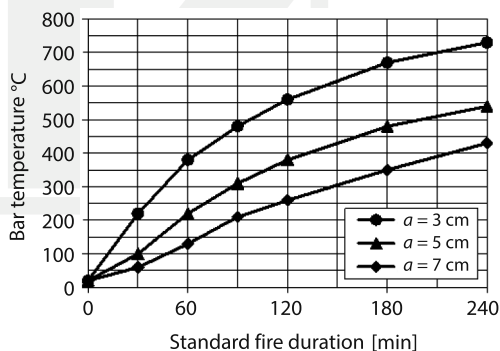


Fig. 1. Recommendation for a simplified evaluation of the temperature in the bars when using the “500°C – Isotherm Method”: a) position of the 500°C – isotherm and, b) the temperature of the reinforcing bars ( $a$  – the axis distance of reinforcement) [13]

Resultant modulus of elasticity of steel was calculated by the formula:

$$\tan \alpha = E_{s,fi} = \frac{\sigma_s(t=0)}{\varepsilon_{s,tot}} \quad (4)$$

Taking into account the impact of the elastic modulus defined by the formula (4), cross-sectional stiffness ( $B_{fi}$ ) has been calculated, according to formula (3), and the adjusted value of the stresses in the reinforcement ( $\sigma_s$ ) has been used. In the next steps calculation procedure described above was repeated for successive durations of fire. Computations have been done applying the calculated load bearing capacity. The cross-section load bearing capacity was calculated according to the 500°C-Isotherm Method, depending on the calculated tensile strength of steel ( $f_{sy,\theta} = k_{s,\theta} f_{yk}$ ) defined by Fig. 3. Tables 2a–d present the main results of the calculations.

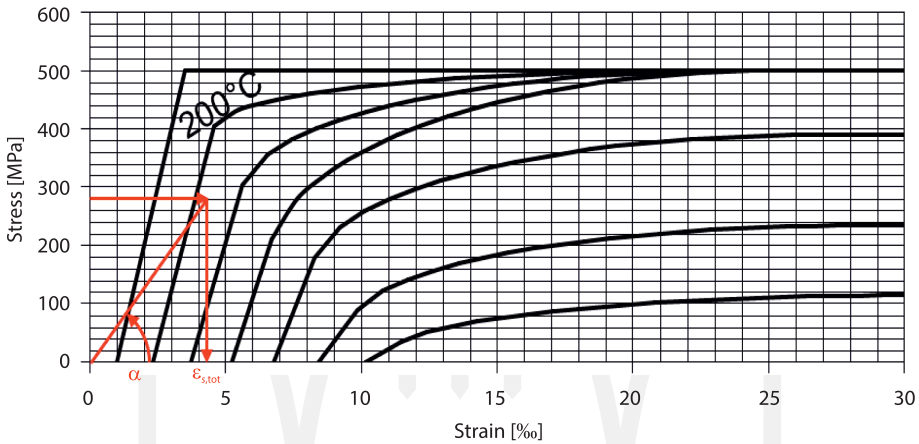


Fig. 2. The stress-strain relationship (included steel free thermal elongation) for hot-rolled reinforcing steel ( $f_{yk} = 500$  MPa) at high temperatures [13]. Looking from the left side of the figure, the successive lines refer to temperatures 100, 200, 300, 400, 500, 600, and 700°C respectively

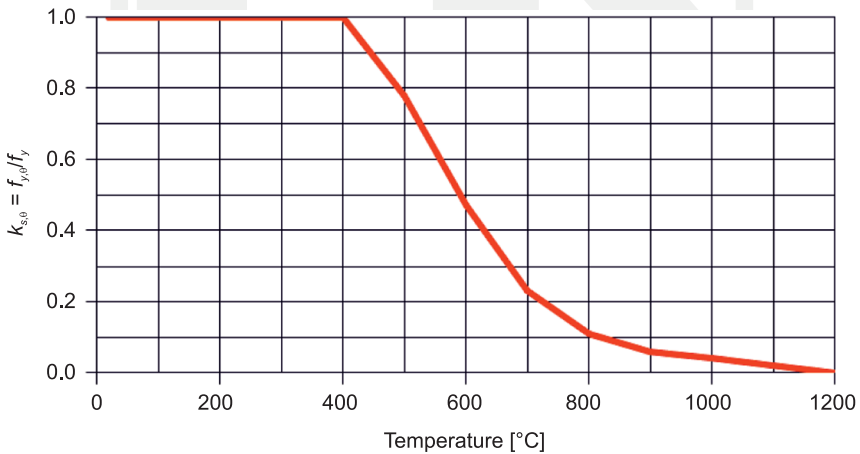


Fig. 3. The reducing factor of the yield strength of reinforcing steel [10]

Table 2a

**Key results of the calculations – a slab span of 7.2 m ( $h = 25$  cm)**

$t$ [min]	$\theta_s$ [°C]	$\sigma_s$ [MPa]	$f_{sy,\Theta}$ [MPa]	$\varepsilon_{s,tot}$ [‰]	$E_{s,fi}$ [GPa]	$B_I$ [kNm <sup>2</sup> ]	$B_{II}$ [kNm <sup>2</sup> ]	$B_{fi}$ [kNm <sup>2</sup> ]	$B_{fi}/B_{fi}(t=0)$
0	20	280	500	1.40	200.0	15 175	4 742	5 691	1.00
30	220	268	500	4.18	67.0	12 905	1 925	2 343	0.41
60	380	264	500	6.91	38.8	11 106	1 192	1 410	0.25
90	480	262	412	9.52	27.7	10 075	881	1 024	0.18
120	560	259	297	17.05	15.4	8 953	511	584	0.10
133	600	257	260	26.59	9,7	7 515	333	370	0.07

Table 2b

**Key results of the calculations – a slab span of 6.0 m ( $h = 20$  cm)**

$t$ [min]	$\theta_s$ [°C]	$\sigma_s$ [MPa]	$f_{sy,\Theta}$ [MPa]	$\varepsilon_{s,tot}$ [‰]	$E_{s,fi}$ [GPa]	$B_I$ [kNm <sup>2</sup> ]	$B_{II}$ [kNm <sup>2</sup> ]	$B_{fi}$ [kNm <sup>2</sup> ]	$B_{fi}/B_{fi}(t=0)$
0	20	270	500	1,35	200.0	7 689	2 319	2 829	1.00
30	220	258	500	4,13	65.0	6 403	931	1 140	0.40
60	380	255	500	6,78	38.1	5 322	580	683	0.24
90	480	253	412	9,22	27.6	4 710	434	499	0.18
120	560	250	297	15,91	15.9	4 057	261	294	0.10
136	590	248	250	28,18	8.9	3 811	151	169	0.06

Table 2c

**Key results of the calculations – a slab span of 4.8 m ( $h = 16$  cm)**

$t$ [min]	$\theta_s$ [°C]	$\sigma_s$ [MPa]	$f_{sy,\Theta}$ [MPa]	$\varepsilon_{s,tot}$ [‰]	$E_{s,fi}$ [GPa]	$B_I$ [kNm <sup>2</sup> ]	$B_{II}$ [kNm <sup>2</sup> ]	$B_{fi}$ [kNm <sup>2</sup> ]	$B_{fi}/B_{fi}(t=0)$
0	20	256	500	1.28	200.0	3 874	1 073	1 390	1.00
30	220	245	500	4.05	63.0	3 145	420	537	0.39

$t$	$\theta_s$	$\sigma_s$	$f_{sy,\Theta}$	$\varepsilon_{s,tot}$	$E_{s,fi}$	$B_I$	$B_{II}$	$B_{fi}$	$B_{fi}/B_{fi}(t=0)$
60	380	241	500	6.62	37.0	2 499	262	315	0.23
90	480	239	412	8.84	27.2	2 140	200	231	0.17
120	560	237	297	14.47	16.5	1 769	126	142	0.10
142	598	235	237	27.85	8.5	1 590	68	75	0.05

Table 2 d

**Key results of the calculations – a slab span of 3.6 m ( $h = 12$  cm)**

$t$	$\theta_s$	$\sigma_s$	$f_{sy,\Theta}$	$\varepsilon_{s,tot}$	$E_{s,fi}$	$B_I$	$B_{II}$	$B_{fi}$	$B_{fi}/B_{fi}(t=0)$
[min]	[°C]	[MPa]	[MPa]	[‰]	[GPa]	[kNm <sup>2</sup> ]	[kNm <sup>2</sup> ]	[kNm <sup>2</sup> ]	
0	20	257	500	1.29	200.0	1 493	364	518	1.00
30	220	245	500	4.05	63.4	1 159	145	193	0.37
60	380	241	500	6.63	37.0	849	90	109	0.21
90	480	240	412	8.85	27.3	684	69	79	0.15
120	560	237	297	14.49	16.5	522	44	48	0.09
140	596	235	240	24.86	9.5	332	26	28	0.04

**2.3. The procedure for calculating the stiffness of the support section  
(heated compressed zone of concrete)**

The first calculation was performed for the beginning of the fire ( $t = 0$  min.), assuming the data presented in Section 2.2. Then, based on formula (3) cross-sectional stiffness ( $B_{fi}$ ) was calculated for successive durations of fire. According to the assumptions of the 500°C – Isotherm Method [10, 11] it dealt with a reduced cross-sectional height (Fig. 4), and unchanged mechanical characteristics of reinforcement ( $E_s = 200$  GPa,  $f_{yk} = 500$  MPa) and concrete ( $E_{c,eff} = 10.63, 10.39, 10.21, 9.91$ , GPa for  $h = 25, 20, 16, 12$ , cm respectively). The location of the 500°C isotherms ( $a_{500}$ ) in cross-section was estimated on the basis of Figure 1a [12].

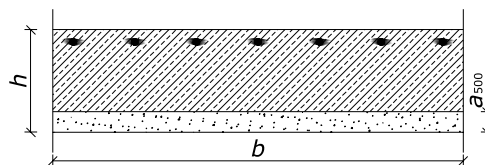


Fig. 4. Reduced cross-section of a slab considered in calculation

For the slabs with a thickness of 25 and 20 cm (range 7.2 and 6.0 m), it was calculated that load bearing capacity of cross-section is not exhausted even after 240 minutes of fire duration. The slabs of smaller thickness calculations were carried out until the calculated load bearing capacity. Tables 3a–d present the main results of the calculations.

Table 3 a

**Key results of the calculations – a slab span of 7.2 m ( $h = 25$  cm)**

$t$ [min]	$a_{500}$ [cm]	$M_{Rd}$ [kNm]	$M_{qp}$ [kNm]	$B_I$ [kNm <sup>2</sup> ]	$B_{II}$ [kNm <sup>2</sup> ]	$B_{f_i}$ [kNm <sup>2</sup> ]	$B_{f_i}/B_{f_i}(t=0)$
0	0.0	123.1	68.1	15 797	6 449	6 847	1.00
30	0.9	117.8	68.1	14 540	5 865	6 177	0.90
60	2.0	111.3	68.1	13 152	5 190	5 421	0.79
90	2.7	107.1	68.1	12 352	4 784	4 974	0.73
120	3.5	102.4	68.1	11 514	4 342	4 492	0.66
180	4.7	95.3	68.1	10 402	3 722	3 827	0.56
240	5.7	89.4	68.1	9 601	3 244	3 321	0.48

Table 3 b

**Key results of the calculations – a slab span of 6.0 m ( $h = 20$  cm)**

$t$ [min]	$a_{500}$ [cm]	$M_{Rd}$ [kNm]	$M_{qp}$ [kNm]	$B_I$ [kNm <sup>2</sup> ]	$B_{II}$ [kNm <sup>2</sup> ]	$B_{f_i}$ [kNm <sup>2</sup> ]	$B_{f_i}/B_{f_i}(t=0)$
0	0.0	76.8	41.6	7 945	3 078	3 295	1.00
30	0.9	72.5	41.6	7 142	2 718	2 878	0.87
60	2.0	67.2	41.6	6 279	2 312	2 420	0.73
90	2.7	63.9	41.6	5 794	2 071	2 155	0.65
120	3.5	60.0	41.6	5 300	1 814	1 876	0.57
180	4.7	54.3	41.6	4 669	1 463	1 501	0.46
240	5.7	49.5	41.6	4 240	1 201	1 225	0.37

**Key results of the calculations – a slab span of 4.8 m ( $h = 16$  cm)**

$t$ [min]	$a_{500}$ [cm]	$M_{Rd}$ [kNm]	$M_{qp}$ [kNm]	$B_1$ [kNm <sup>2</sup> ]	$B_{II}$ [kNm <sup>2</sup> ]	$B_{fi}$ [kNm <sup>2</sup> ]	$B_{fi}/B_{fi}(t=0)$
0	0.0	46.2	23.8	3 974	1 406	1 540	1.00
30	0.9	42.8	23.8	3 458	1 193	1 283	0.83
60	2.0	38.6	23.8	2 923	958	1 012	0.66
90	2.7	36.0	23.8	2 633	824	862	0.56
120	3.5	33.0	23.8	2 347	683	708	0.46
180	4.7	28.5	23.8	2 002	498	511	0.33
228	5.5	25.4	23.8	1 823	393	401	0.26

Table 3 d

**Key results of the calculations – a slab span of 3.6 m ( $h = 12$  cm)**

$t$ [min]	$a_{500}$ [cm]	$M_{Rd}$ [kNm]	$M_{qp}$ [kNm]	$B_1$ [kN/m <sup>2</sup> ]	$B_{II}$ [kN/m <sup>2</sup> ]	$B_{fi}$ [kN/m <sup>2</sup> ]	$B_{fi}/B_{fi}(t=0)$
0	0.0	23.6	11.8	1 623	490	558	1.00
30	0.9	21.1	11.8	1 333	384	423	0.76
60	2.0	18.0	11.8	1 047	274	292	0.52
90	2.7	16.0	11.8	902	214	225	0.40
120	3.5	13.8	11.8	768	156	162	0.29
156	4.0	12.4	11.8	700	124	128	0.23

### 2.3. Analysis of stiffness reduction in cross-section of slabs

Figure 5 shows the ratio of the stiffness of the cross section, calculated for successive durations of the fire against the initial stiffness ( $B_{fi}/B_{fi}(t=0)$ ), for span and support cross-sections (Table 2a–d, 3a–d). Figure 6 shows the ratio of stiffness of the cross-sectional span against support cross-section stiffness, depending on the duration of the fire.

A relative decrease in span cross-section stiffness (with heated reinforcement) occurs much faster than support cross-sections (with heated concrete compression zone). In all examined

span cross-sections, regardless of their height in the initial phase of the fire ( $t = 30$  min.) more than 60% reduction in stiffness has been reached. The support cross-sections of the stiffness was reduced, the faster, the lower section height. The ratio of stiffness of the span cross-section against support cross-section stiffness fell twice after thirty minutes of fire for all the thicknesses. A significant change in the proportion of the stiffness of the span and support cross-sections should lead to a substantial redistribution of bending moments, which is an increase support moments and reducing the span moments.

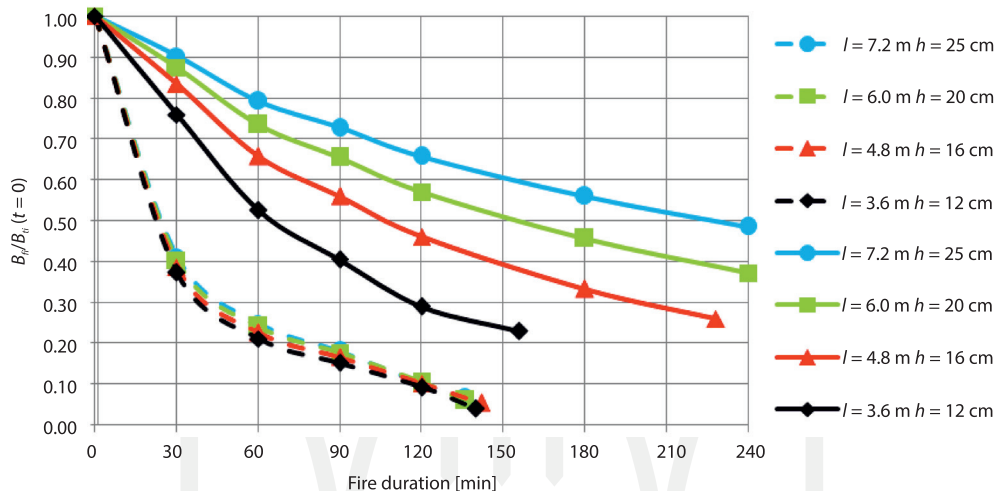


Fig. 5. Stiffness ratio of slabs cross-section, calculated for successive durations of fire, against the initial stiffness, continuous lines – support cross-sections, dashed lines – span cross-sections

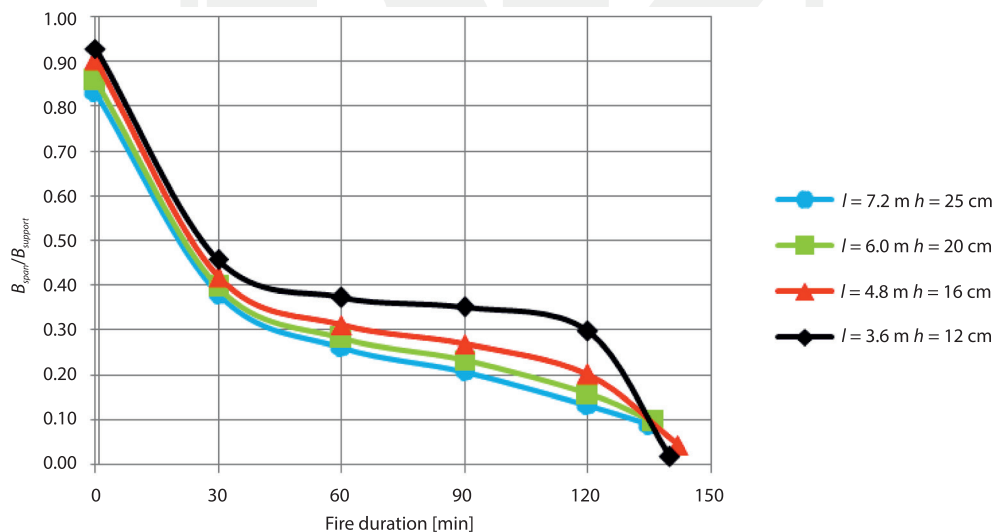


Fig. 6. The ratio of span cross-section stiffness against the support cross-section stiffness, depending on the duration of fire

### 3. Stiffness of cross-section R/C beams under fire conditions

#### 3.1. Assumptions

Two beams (two – span) were considered with a span 6.0 m and 7.5 m. It was assumed that the beam with a span  $l = 6.0$  m takes the load from the slab with a width of 4.20 m ( $h = 25$  cm), and the beam with a span  $l = 7.5$  m takes the load from the slabs width 7.5 m ( $h = 25$  cm). Slabs variable loads and combinations of load were assumed in the same way as described in Section 2.1. C 30/37 concrete and main reinforcement steel with characteristic yield strength  $f_{yk} = 500$  MPa were assumed, distance from the axis of the main bars from the edge of the cross-section was 50 mm. Cross-sections of beams and reinforcement bars were chosen such that they satisfy the terms of the boundary condition, load bearing capacity and serviceability for the degree of reinforcement span cross-section close to 1%. In Table 4 are the most important items of information about the beams.

Table 4

Key parameters considered beams

Lenght	Cross-section	Moment [kNm]		Span reinforcement			Support reinforcement		
		$l$ [m]	$b \times h$ [m]	span	support	$\eta$	$A_s$	$\rho$ [%]	$\eta$
6.00	$0.25 \times 0.50$	130.8	178.1	0.62	4 $\phi$ 20	1.10	0.66	6 $\phi$ 20	1.68
7.50	$0.35 \times 0.70$	369.5	583.4	0.62	7 $\phi$ 20	0.97	0.66	12 $\phi$ 20	1.66

Stiffness of the beam cross-sections were determined based on assumptions of the 500°C-Isotherm Method, as described in Chapter 2. The following section presents important information on procedures for the performed calculations.

#### 3.2. The procedure for calculating cross-sectional stiffness (heated reinforcement)

First, similar to Section 2.2, the calculations were performed for the outbreak of fire,  $t = 0$  min. For beams  $l = 6.0$  m and  $l = 7.5$  m there were adopted accordingly:  $\varphi = 2.37$ ,  $E_{c,eff} = 9.74$  GPa;  $\varphi = 2.26$ ,  $E_{c,eff} = 10.07$  GPa. In order to calculate the stiffness of the cross-section on fire conditions, it is necessary to estimate the temperature of reinforcement ( $\theta_s$ ) and the corresponding resultant modulus of steel ( $E_{s,ff}$ ). Resultant modulus of elasticity of steel is calculated analogously to the slab on the basis of Fig. 2 and formula (4).

Reinforcement temperature ( $\theta_s$ ) is estimated on the basis of Fig. 7 [12]. They are the guidelines for a simplified prediction of the temperature of the reinforcement in reinforced concrete beams cross-sections exposed to standard fire conditions.

In considering the beams, it should be taken into account that the temperature of the bars located in the corners of the cross-section is higher than that of bars located in the central part. This is reflected in the guidance given in Fig. 7. In the calculations, the corner and the middle bar temperatures has been set, then the resultant temperature was estimated as

a weighted average depending on the number of corner bars and middle bars. Table 5 shows the estimated bars temperature values.

On the basis of the average temperature value of resultant (secant) modulus elasticity of steel was specified, based on the graphs shown in Fig. 2.

Stiffness of the cross-section was calculated by the formula (3). Calculations have been done for the time at which ULS has occurred. Tables 6a and 6b present the main results of the calculations.

Table 5

### Estimated temperature of bars

Fire <i>t</i> min	Estimated temperature of bars [°C]					
	<i>L</i> = 6.0 m (2ø cor + 2ø midd)			<i>L</i> = 7.5 m (2ø cor + 5ø midd)		
	corner	middle	average	corner	middle	average
0	20	20	20	20	20	20
30	180	155	168	180	130	144
60	340	290	315	340	240	269
90	500	425	463	500	350	393
120	570	495	533	570	420	463
180	710	635	673	710	560	603
240	850	775	813	850	700	743

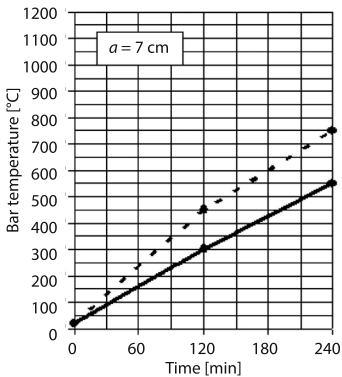
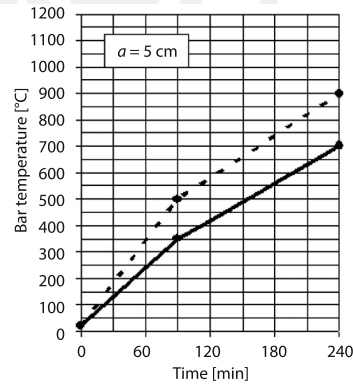
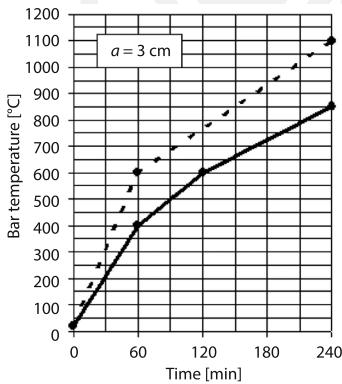
Table 6a

### Key results of the calculations – a beam span of 6.0 m (25 × 50 cm)

<i>t</i> [min]	$\theta_s$ [°C]	$\sigma_s$ [MPa]	$f_{sy,\theta}$ [MPa]	$\varepsilon_{s,tot}$ [‰]	$E_{s,fi}$ [GPa]	$B_I$ [kNm <sup>2</sup> ]	$B_{II}$ [kNm <sup>2</sup> ]	$B_{fi}$ [kNm <sup>2</sup> ]	$B_{fi}/B_{fi}(t=0)$
0	20	249	500	1.24	200.0	58 662	37 409	38 513	1.00
30	168	242	500	3.22	77.3	62 297	16 215	16 754	0.44
60	315	240	500	5.48	44.2	52 189	9 721	9 979	0.26
90	463	238	430	8.37	28.7	42 808	6 477	6 607	0.17
120	533	237	340	20.82	20.8	37 001	4 791	4 870	0.13
148	597	235	238	26.40	9.0	28 876	2 138	2 163	0.06

Key results of the calculations – a beam span of 7.5 m (35 × 70 cm)

$t$ [min]	$\theta_s$ [°C]	$\sigma_s$ [MPa]	$f_{sy,\theta}$ [MPa]	$\varepsilon_{s,tot}$ [‰]	$E_{s,fi}$ [GPa]	$B_I$ [kNm <sup>2</sup> ]	$B_{II}$ [kNm <sup>2</sup> ]	$B_{fi}$ [kNm <sup>2</sup> ]	$B_{fi}/B_{fi}(t=0)$
0	20	276	500	1.38	200.0	202 491	140 242	142 500	1.00
30	144	271	500	3.01	91.7	240 802	703 511	72 294	0.51
60	269	268	500	4.90	55.3	206 929	44 210	45 237	0.32
90	393	266	500	7.24	37.0	181 891	30 437	31 031	0.22
120	463	266	430	29.43	29.4	166 877	24 513	24 938	0.18
148	578	263	267	25.29	10.5	136 263	9 138	9 259	0.06



For  $b \geq 30$  cm;  
for corner bars – broken curve,  
for middle bars – solid curve;

For  $20 < b < 30$  cm;  
for corner bars – broken curve,  
for middle bars – interpolation;  
between solid and broken curve.

For  $15 \leq b < 20$  cm;  
for all bars – broken curve.

Fig. 7. Temperature of the reinforcing bars in R/C beams subjected to standard fire [12] ( $a$  – distance between the bar axis and the surface of the concrete;  $b$  – cross-section width)

### 3.3. The procedure for calculating the stiffness of the support cross-section (heated compressed zone of concrete)

First, calculations for the beginning of the fire were performed. Then, based on formula (3), calculated cross-sectional stiffness ( $B_{fi}$ ) for successive durations of fire was established. According to the assumptions of the 500°C-Isotherm Method [10, 11] it dealt with a reduced cross-sectional size (Fig. 8), and unchanged mechanical characteristics of reinforcement ( $E_s = 200$  GPa,  $f_{yk} = 500$  MPa) and concrete ( $E_{c,eff} = 10.63$  and 9.94 GPa for  $h = 25$  and 12 cm respectively).

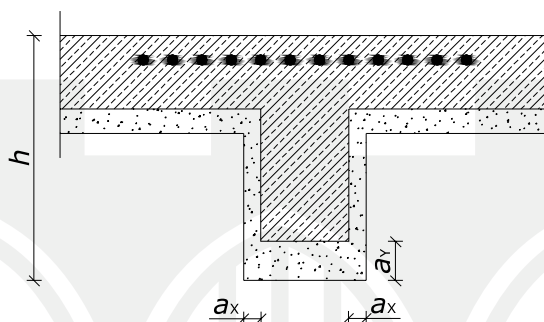


Fig. 8. Reduced cross-section of a beam considered in calculation

Location of 500°C isotherms in the cross-section was estimated on the basis of Fig. 9 [12]. They are the guidelines for a simplified forecasting 500°C isotherm distance from the side edge ( $a_x$ ) and lower edge ( $a_y$ ) of the cross-section reinforced concrete beams exposed to standard fire. Tables 7a and 7b show the main results of the calculations.

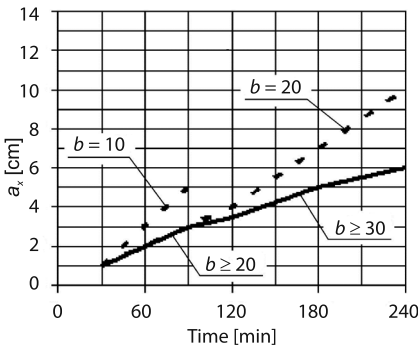
Table 7a

#### Key results of the calculations – a beam span of 6.0 m (25 × 50 cm)

$t$ [min]	$a_x$ [cm]	$a_y$ [cm]	$M_{Rd}$ [kNm]	$M_{qp}$ [kNm]	$B_I$ [kNm <sup>2</sup> ]	$B_{II}$ [kNm <sup>2</sup> ]	$B_{fi}$ [kNm <sup>2</sup> ]	$B_{fi}/B_{fi}(t=0)$
0	0.0	0.0	366.1	206.2	37 296	28 463	28 790	1.00
30	1.0	2.0	339.6	206.2	66 708	24 456	24 880	0.86
60	2.0	3.0	321.6	206.2	56 062	22 050	22 318	0.78
90	3.0	4.8	294.1	206.2	43 962	18 754	18 896	0.66
120	3.5	6.5	271.7	206.2	36 469	16 323	16 412	0.57
165	5.8	9.3	206.9	206.2	20 531	11 315	11 333	0.39

**Key results of the calculations – a beam span of 7.5 m (35 × 70 cm)**

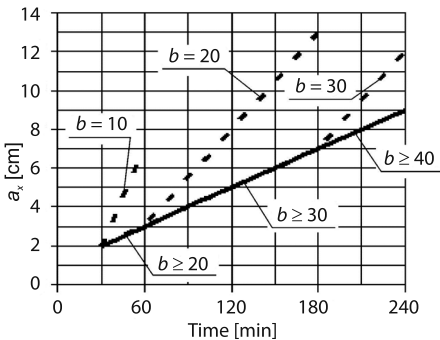
$t$ [min]	$a_x$ [cm]	$a_y$ [cm]	$M_{Rd}$ [kNm]	$M_{qp}$ [kNm]	$B_1$ [kNm <sup>2</sup> ]	$B_{II}$ [kNm <sup>2</sup> ]	$B_{fi}$ [kNm <sup>2</sup> ]	$B_{fi}/B_{fi}(t=0)$
0	0.0	0.0	1041.2	583.4	153 669	119 706	121 026	1.00
30	1.0	2.0	989.7	583.4	283 328	107 916	109 831	0.91
60	2.0	3.0	955.9	583.4	251 194	100 718	102 112	0.84
90	3.0	4.8	904.6	583.4	212 888	90 611	91 520	0.76
120	3.5	6.5	862.7	583.4	187 701	82 876	83 537	0.69
180	6.0	10.0	737.4	583.4	123 388	63 875	64 087	0.53
240	8.0	12.0	630.7	583.4	87 325	52 027	52 104	0.43



Time  $t < 90$  min:  
broken line for  $b = 10$  cm,  
solid line for  $b \geq 20$  cm.

Time  $t \leq 90$  min:  
broken line for  $b = 20$  cm,  
solid line for  $b \geq 30$  cm.

Interpolate in intermediate cases



Time  $t < 60$  min:  
broken line for  $b = 10$  cm,  
solid line for  $b \geq 20$  cm.

Time  $60 \leq t < 180$  min:  
broken line for  $b = 20$  cm,  
solid line for  $b \geq 30$  cm.

Time  $t \geq 180$  min:  
broken line for  $b = 30$  cm,  
solid line for  $b \geq 40$  cm.

Interpolate in intermediate cases

Fig. 9. Position of the 500°C – isotherm in R/C beams subjected to standard fire [12] ( $a_x$  – measured from the lateral side and  $a_y$  – measured from the bottom side)

### 3.4. Analysis of stiffness reduction in cross-section beams

Figure 10 shows the ratio of the stiffness of the cross-section, calculated for successive durations of the fire against the initial stiffness ( $B_{fi}/B_{fi}(t=0)$ ) for span and support cross-sections (Tables 6a–b and 7a–b). Figure 11 shows the ratio of span cross-section stiffness against the stiffness of the support cross-section depending on the duration of the fire.

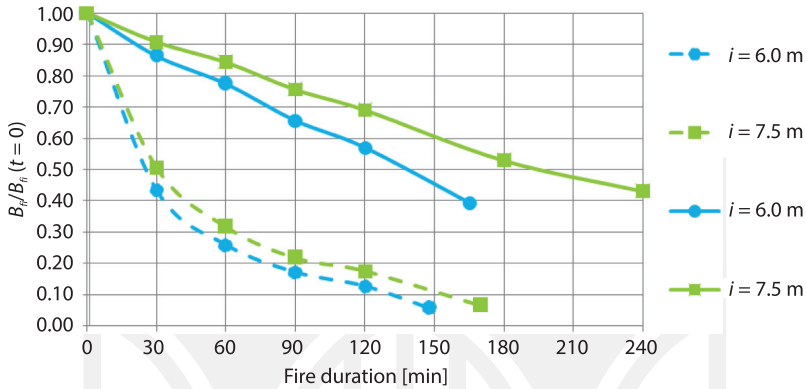


Fig. 10. Stiffness ratio of the beam cross-section calculated for successive durations of fire to the initial stiffness; solid lines – support cross-sections, broken lines – span cross-sections

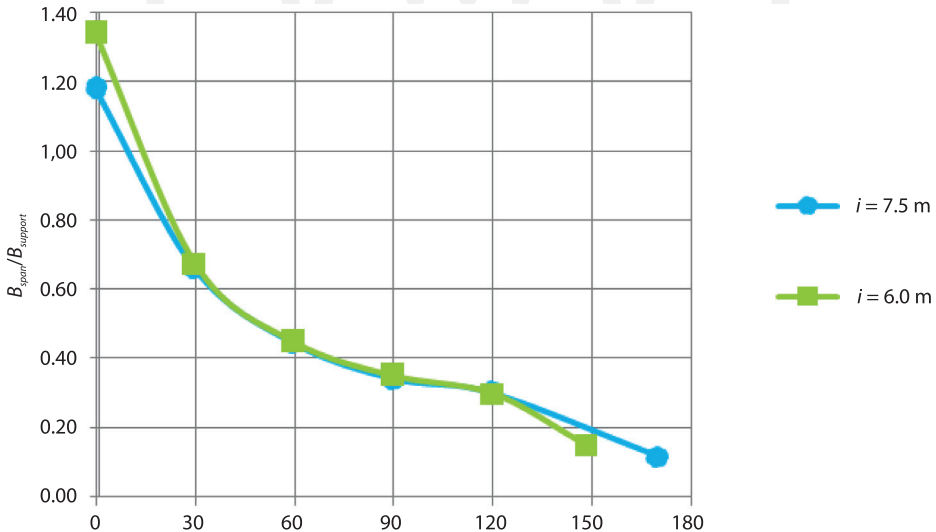


Fig. 11. The ratio of span cross-section stiffness beams against the stiffness of the support cross-section, depending on the duration of the fire

As in the case of the examined slabs, the relative reduction of span cross-sections stiffness (with heated reinforcement) occurs much faster than cross-sections stiffness of the support (within the heated concrete compression zone). In span cross-sections, already in the initial

phase of the fire ( $t = 30$  min.) more than 50% reduction in stiffness was reached. Stiffness in the cross-sections of the support is reduced more quickly the smaller the cross-sectional dimensions are. The ratio of span stiffness to the support stiffness decreased approximately twice after thirty minutes of fire duration. A significant change in the proportion of the stiffness of the span and support cross-sections should lead to a substantial redistribution of bending moments, i.e. increasing support moments and reducing the span moments.

#### 4. Redistribution of bending moments

##### 4.1. The assumptions and calculation procedure

Effect of changes in the stiffness of cross-sections in fire conditions on the redistribution of bending moments is defined in the examples: (1) two span beams with span length of 7.5 m, cross-section  $b \times h = 30 \times 70$  cm, (2) two span slabs with span length 7.2 m, cross-section height  $h = 25$  cm.

Using a computer program (Finite Element Method), calculations of bending moments in the designed permanent situation and accidental situation for the successive durations of fire in slabs and beams have been made. In the locations of the (positive) sagging bending moments for the calculation of the heated sections of the reinforcement (span), the stiffness defined in Section 2.2 or 3.2 has been taken. In the locations of the (negative) hogging bending moments assumed rigidity of the heated sections of concrete compression zone (the support), has been taken as defined in Section 2.3 or 3.3.

The paper presents the calculation results obtained in two the less favorable cases of the variable load location and operation of the fire (Fig. 12):

- variable load is located on one span only, which is subjected to the action of fire from the bottom (Fig. 12a),
- variable load is placed on both spans, which are subjected to the action of fire from the bottom (Fig. 12b).

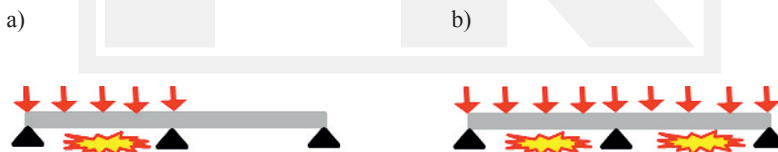


Fig. 12. Cases of variable loads and location of the impact of fire

##### 4.2. Beam with a 7.5 m span length, cross-section $b \times h = 30 \times 70$ cm

Figure 13 shows diagrams of bending moments in the beam exposed to variable load and fire in one span only (according to Fig. 12a) in a persistent design situation, and in subsequent fire durations. Red horizontal lines correspond to the values of calculated load bearing capacity.

Figure 14 shows the comparison between the calculated bending moment and calculated load bearing capacity, in span and support cross-sections of the beam shown in Fig. 13.

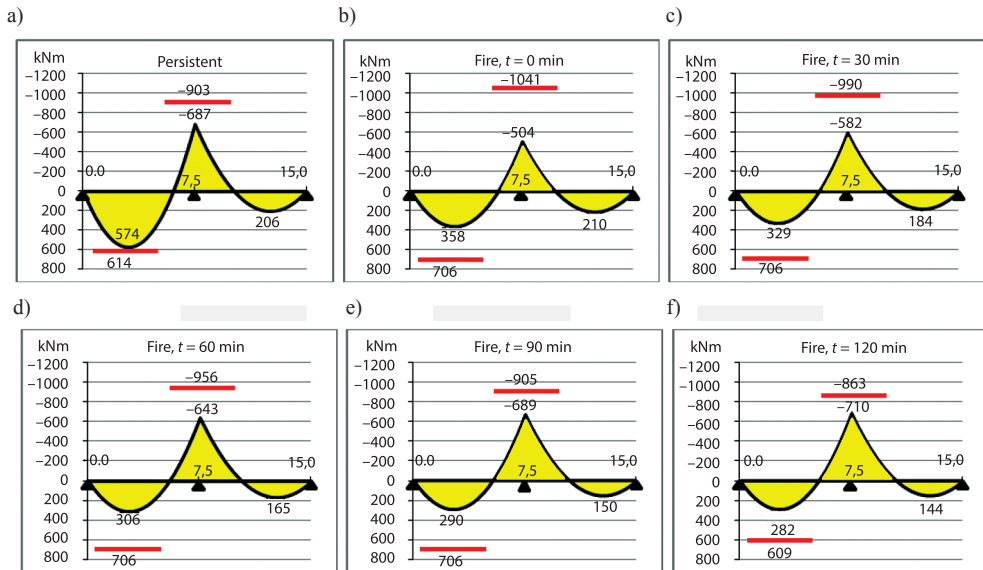


Fig. 13a–f. Bending moments for 7.5 m span length beam, 35 × 70 cm cross-section, variable load and fire in one span only

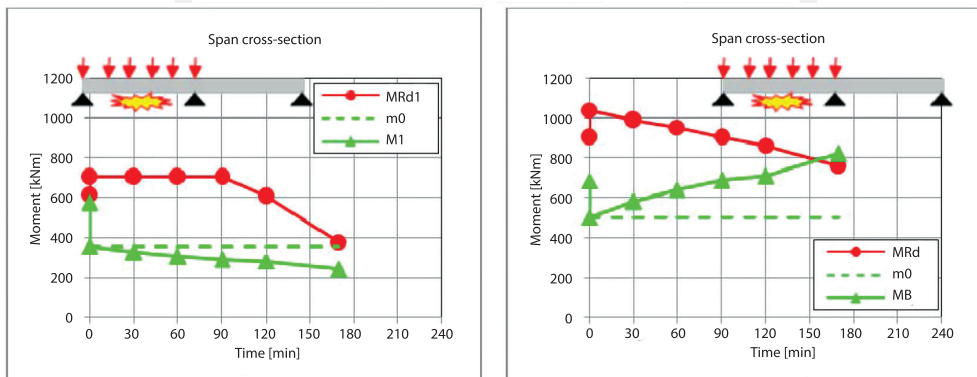


Fig. 14. Comparison of calculated bending moments and calculated load bearing capacity in span and support cross-sections: 7.5 m span length beam, 35 × 70 cm cross-section, variable load and fire in one span only. Red curve – calculated load bearing capacity, green solid line – calculated bending moment, redistribution considered; green broken line – calculated bending moment, redistribution neglected

Figures 15–16, in the same manner, present graphs of bending moments in the same beam, where a variable load and fire operate on both spans (according to Fig. 12b).

With the “transition” from a persistent design situation to accidental situation of fire (Fig. 13a, b, Fig. 15a, b) the calculated load bearing capacity greatly increases. Then, as the fire takes effect, span moments decrease and support moments increase.

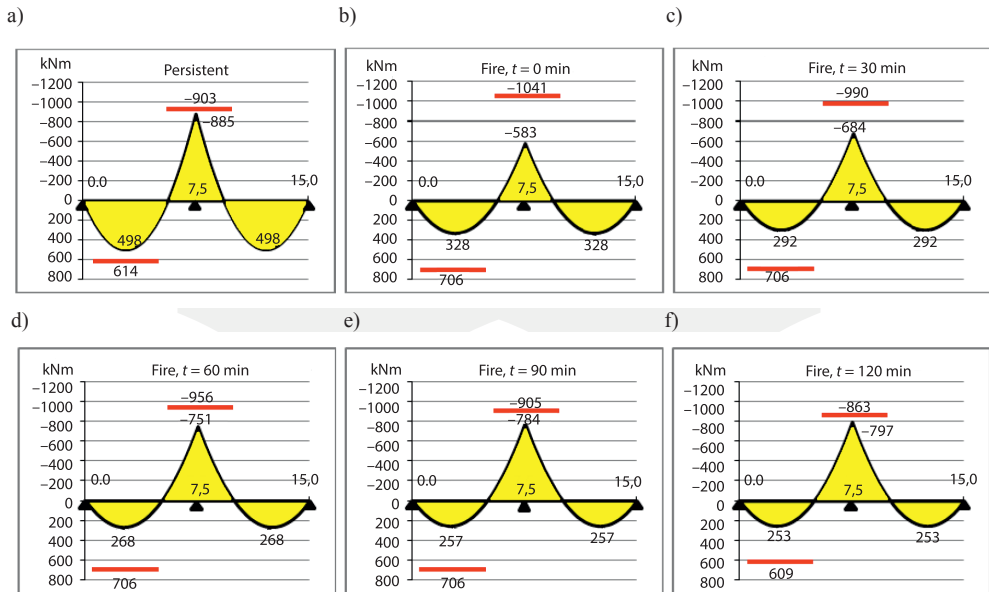


Fig. 15a+f. Bending moments for 7.5 m span length beam, 35 × 70 cm cross-section, variable load and fire in both spans

In span cross-sections (Fig. 14, 16), slightly decreasing the calculated moment “moves away” from the rapidly decreasing calculated load bearing capacity. This causes a slight delay of a computational load limit state in cross-sections of the span.

In the cross-sections of the support (Fig. 14, 16) rapidly growing calculated moment soon “approaches” the decreasing calculated load bearing capacity. This results in a significant acceleration of the ultimate limit state in cross-sections of the support.

Consequently, as a result of redistribution of bending moments, the calculated ultimate limit state occurs firstly in the support cross-section, and then in cross-section of the span. If omitted, the redistribution of bending moments would cause the reverse situation. ULS occurs first in the span cross-section, and then in the support cross-section.

Please note that the occurrence of ULS in a support cross-section will result in a “descending” graph of bending moments, which was not considered in this paper.

In conclusion, it can be estimated that in the case of load and fire on the two spans (Fig. 16), as a result of redistribution of bending moments, calculated destruction of the beam occurs about 40 minutes earlier than it would appear according to the calculations with neglected redistribution of bending moments. In the case of load and fire in one span only, inclusion or omission of redistribution of bending moments is not essential for a fixed computational time of the beam destruction.

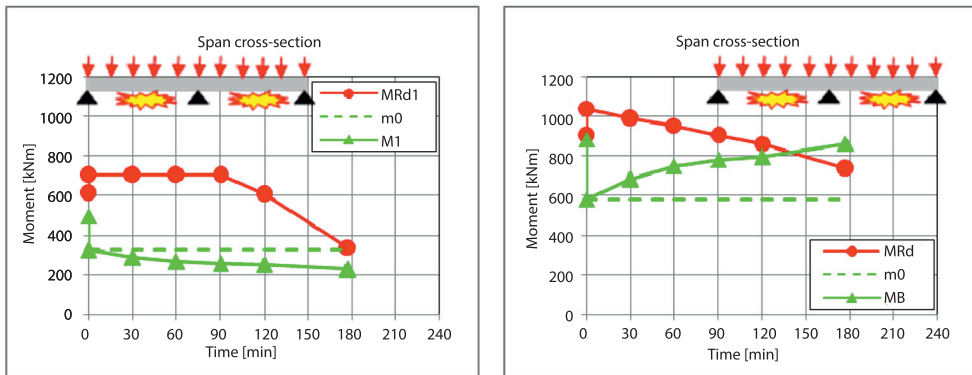


Fig. 16. Comparison of calculated bending moments and calculated load bearing capacity in span and support cross-sections: 7.5 m span length beam, 35 × 70 cm cross-section, variable load and fire in both spans. Red curve – calculated load bearing capacity, green solid line – calculated bending moment, redistribution considered; green broken line – calculated bending moment, redistribution neglected

4.3. Slab with a span of 7.2 m, height cross-section  $h = 25$  cm

Figures 17 to 20 present graphs of bending moments in two span slabs of 7.2 m span length, cross-section height  $h = 25$  cm, in the same manner as in the previous chapter.

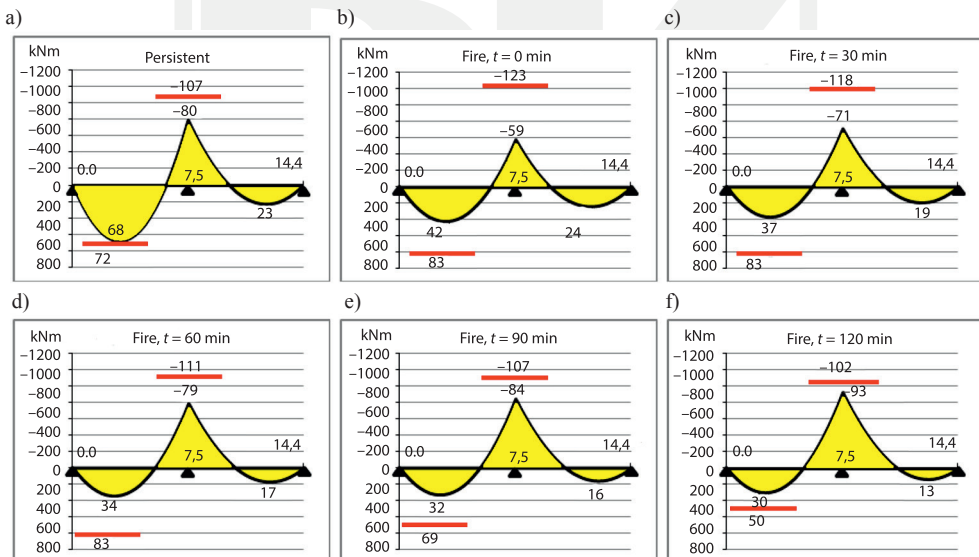


Fig. 17a-f. Bending moments for 7.2 m span length slab, depth 25 cm, variable load and fire in one span only

In the examined slab, a similar effect of redistribution of bending moments has been observed, as in the beam considered in the chapter 4.2. As a result of the redistribution of bending moments, the ultimate limit state occurs firstly in the cross-section of a support, and then in cross-section of span. In the case of the slab, redistribution of bending moments, however, does not cause acceleration of ULS.

The Fig. 18 and 20 shows the two aforementioned fire situations to cross-sections of the span and the support of the two span slabs of 7.2 m span. Red curve – calculated load bearing capacity, green solid line – calculated bending moment; redistribution considered, green broken line – calculated bending moment; redistribution neglected.

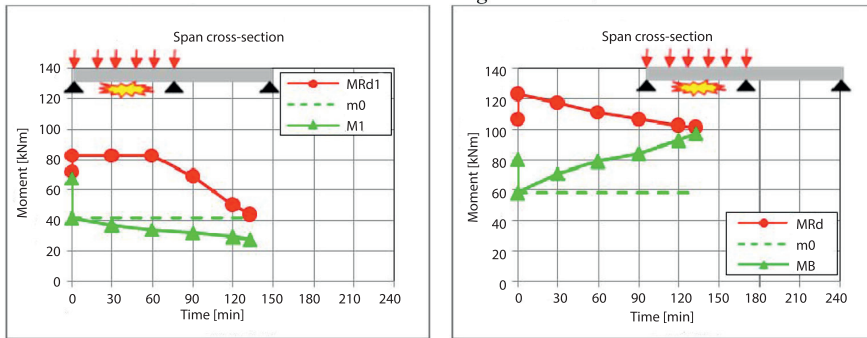


Fig. 18. Comparison of the calculated bending moments and the calculated load bearing capacity in span and support cross-sections: 7.2 m span length slab, 25 cm cross-section depth, variable load and fire in one span only. Red curve – calculated load bearing capacity, green solid line – calculated bending moment; redistribution considered, green broken line – calculated bending moment; redistribution neglected

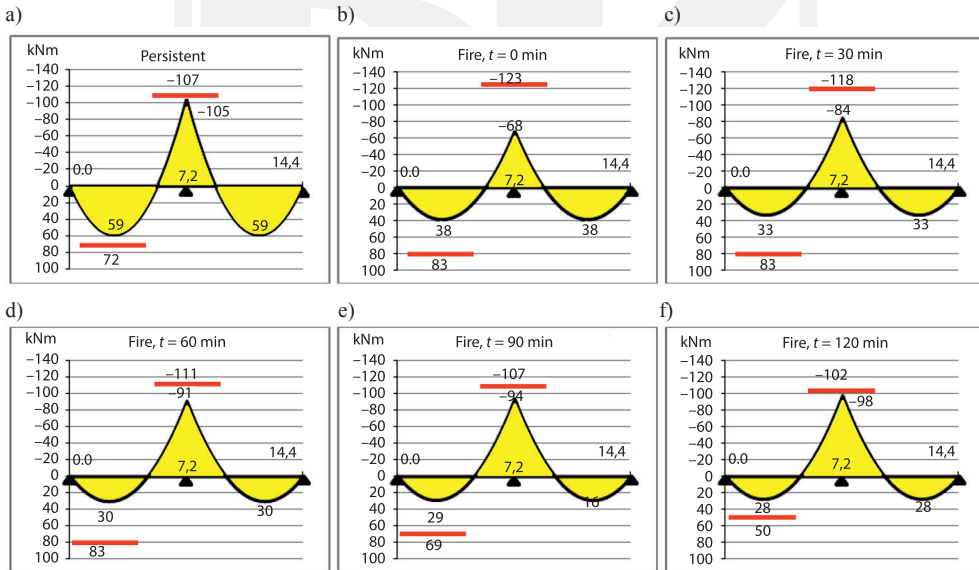


Fig. 19a-f. Bending moments for 7.2 m span length slab, cross-section depth 25 cm, variable load and fire in both spans

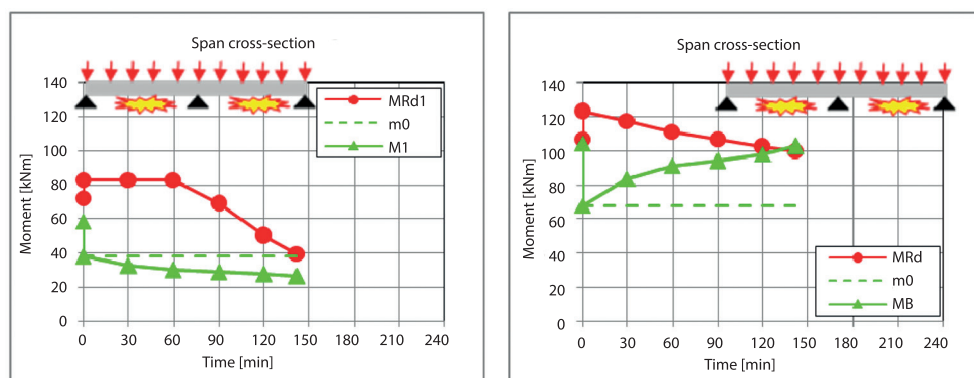


Fig. 20. Comparison of the calculated bending moments and the calculated load bearing capacity in span and support cross-sections: 7.2 m span length slab, 25 cm cross-section depth, variable load and fire in both spans. Red curve – calculated load bearing capacity, green solid line – calculated bending moment, redistribution considered; green broken line – calculated bending moment, redistribution neglected

## 5. Conclusions

In the first part of the paper, there has been analyzed computationally, how the stiffness of the encountered in practice cross-sections of slabs and cross-sections of reinforced concrete beams exposed to fire only on the tensile reinforcement, or only from the compression zone of concrete changes. The calculations were based on assumptions of the 500°C-Isotherms Method recommended in [10] to calculate the load bearing capacity of reinforced concrete elements exposed to standard fire.

Reduction of span cross-sections stiffness (with heated reinforcement) occurs much faster than the reduction of support cross-sections stiffness (with heated concrete compression zone). Already in the initial phase of the fire ( $t = 30$  min) a ratio of span cross-section stiffness to the stiffness of the support cross-section decreased approximately twice. This significant change in the proportion of the stiffness of the span and support cross-section can cause the redistribution of bending moments.

In the second part of the paper, for example of two span elements, it has been estimated the impact of changes in stiffness of the cross-sections on redistribution of bending moments.

As a result of the redistribution of bending moments, a slight decrease in the span moments and relatively significant increase in the support moments should be expected. Consequently, the calculated ultimate limit state occurs firstly in the cross-section of a support, and then in the span cross-section. If omitted, the redistribution of bending moments would cause the reverse situation. ULS would occur firstly in the span cross-section, and then in the support cross-section.

The ultimate limit state in elements with a relatively large cross section (as a result of redistribution of bending moments due to changes in stiffness of the cross-section) may occur slightly earlier than could be expected when the impact of redistribution is neglected. In elements with a relatively small cross-section, the redistribution of bending moments should not have a significant impact on the time in which the ultimate limit state occurs.

## References

- [1] Buchanan A.H., *Structural Design for Fire Safety*, John Wiley and Sons Ltd., 2002.
- [2] fib Bulletin 46/2008, *Fire design of concrete structures – structural behaviour and assessment, State-of-art report*, International Federation for Structural Concrete (fib), July 2008.
- [3] fib Bulletin 38/2007, *Fire design for concrete structures – materials, structures and modelling, State-of-art report*, International Federation for Structural Concrete (fib), April 2007.
- [4] Kowalski R., Król P., *Experimental Examination of Residual Load Bearing Capacity of RC Beams Heated up to High Temperature*, Sixth International Conference “Structures in Fire”, Michigan State University, East Lansing, Michigan, USA 2010. Proceedings edited by V.K.R. Kodur and J.M. Fransen, DEStech Publications Inc.
- [5] Eurocode 2, Fire Design of concrete structures – Part 1–1: General rules and rules for buildings, EN 1992-1-1: 2004.
- [6] Kordina K., Design of concrete buildings for fire resistance. Chapter 6 in: Structural concrete, Textbook on behaviour, design and performance. Second edition. Vol. 4, fib bulletin 54, 2010.
- [7] Eurocode 0, Basis of structural design, EN 1990: 2002.
- [8] Eurocode 1, Actions on structures – Part 1–1: General actions – Densities, self-weight, imposed loads for building, EN 1991-1-1: 2002.
- [9] Eurocode 1, Actions on structures – Part 1–2: General actions – Actions on structures exposed to fire, EN 1991-1-2: 2002.
- [10] Eurocode 2, Design of concrete structures – Part 1–2: General rules – Structural fire design, EN 1992-1-2: 2004.
- [11] Taerwe L.R., *Fire Design of Concrete Structures According to the Eurocodes: A Review*, SP-255-4, 75-96 in: Design of Concrete Structures for Fire Safety, ACISP-255, ACI, Detroit 2008.
- [12] Kowalski R., *On the Identification of the Reference Isotherm in the Simplified Analysis of R/C Members in Fire*, Studies and Researches, ed. by Politecnico di Milano and Italcementi, pub. by STARRYLINK (Brescia, Italy), 2010.
- [13] Abramowicz M., Kowalski R., *Stress-strain relationship of reinforcing steel subjected to tension and high temperature*, International Conference: Applications of Structural Fire Engineering, Prague 2009, Conf. proc.

## CONTENTS

Chudyba K., Matysek P.: Methods for determining masonry walls fire resistance.....	3
Chudyba K., Seręga S.: Structural fire design methods for reinforced concrete members.....	15
Derkowski W., Kwiecień A., Zając B.: CFRP strengthening of bent RC beams using stiff and flexible adhesives.....	37
Gromysz K.: Dissipative forces in joint surface of composite reinforced concrete floors .....	53
Habiera E., Czkwianianc A.: Redistribution of forces between reinforcement bars and profiles in the intermediate support zone in the double span, double combined beams.....	67
Kałuża M., Kubica J.: Behaviour of unreinforced and reinforced masonry wallettes made of ACC blocks subjected to diagonal compression.....	79
Klemczak B., Knoppik-Wróbel A.: Numerical model for analysis of early-age thermal-moisture effects in an RC wall .....	95
Kowalski R., Urbański M.: Redistribution of bending moments in multi – span R/C beams and slabs subjected to fire.....	115

## TREŚĆ

Chudyba K., Matysek P.: Metody określania odporności ogniowej ścian murowanych.....	3
Chudyba K., Seręga S.: Metody projektowania elementów żelbetowych z uwagi na warunki pożarowe.....	15
Derkowski W., Kwiecień A., Zając B.: Wzmocnienie zginanych elementów żelbetowych przy użyciu CFRP na sztywnych i podatnych klejach .....	37
Gromysz K.: Siły rozpraszające energię w zespoleniu żelbetowych stropów warstwowych.....	53
Habiera E., Czkwianianc A.: Redystrybucja sił pomiędzy zbrojeniem prętowym i kształtowym w strefie podpory środkowej w dwuprzęsłowych belkach podwójnie zespolonych .....	67
Kałuża M., Kubica J.: Zachowanie się niezbrojonych i zbrojonych murowanych elementów wykonanych z bloczków z autoklawizowanego betonu komórkowego poddanych ukośnemu ścisłaniu .....	79
Klemczak B., Knoppik-Wróbel A.: Model numeryczny do analizy wczesnych wpływów termiczno-wilgotnościowych w ścianie żelbetowej .....	95
Kowalski R., Urbański M.: Redystrybucja momentów zginających w wieloprzęsłowych belkach i płytach żelbetowych w warunkach pożarowych.....	115

